Fall 2021

Enhancing Charge Carrier Mobility in Colloidal Quantum Dots For Technological Applications

Fiaz Ahmed

ENHANCING CHARGE CARRIER MOBILITY IN COLLOIDAL QUANTUM DOTS FOR TECHNOLOGICAL APPLICATIONS

by

Fiaz Ahmed

Bachelor of Science
University of Education, 2012

Bachelor of Education
University of Education, 2012

Master of Science
Lahore University of Management Sciences, 2015

Submitted in Partial Fulfillment of the Requirements

For the Degree of Doctor of Philosophy in

Chemistry

College of Arts and Sciences

University of South Carolina

2021

Accepted by:

Andrew B. Greytak, Major Professor

Sophya Garashchuk, Committee Member

Morgan Stefik, Committee Member

Asif Khan, Committee Member

Tracey L. Weldon, Interim Vice Provost and Dean of the Graduate School

DEDICATION

To my beloved family. My father, the late Bashir Ahmed Choudhary and my mother Rasheedan BiBi, my sisters Nazia and Sadia, my brother Ijaz Ali and my wife Farah.

Thank you all for your endless love, sacrifices, prayers, support, and advice.

ACKNOWLEDGEMENTS

This work would not have been possible without the help of a great many people. I would like to gratefully thank Dr. Greytak for his endless guidance and encouragement throughout my PhD. His patience, dedication, and wisdom have shown me the best qualities a scientist can achieve. I would also like to thank Dr. Chandrashekhar for his unwavering guidance, insight, and patience along the way. It has been a true privilege to work with you. I am thankful to my committee members: Dr. Sophya Garashchuk, Dr. Morgan Stefik, Dr. Asif Khan for their support, commitment, and valuable insights. Thank you very much!

A special thank you to Dr. Perry Pellechia for his help with NMR spectroscopy and analysis, and to Dr. Stefik's lab for their contributions to this work.

Immense thanks to the entire Greytak lab past and present for their endless support and contributions. I am also very appreciative of the wonderful people that I had the opportunity to meet during my graduate career. Thank you Dr. Preecha Kittikhunnatham, Dr. John Dunlap, Sakiru Abiodun, and Nuwanthaka Millaniyage for their valuable insight and sense of humor, you all are truly amazing human beings.

I am also thankful to Dr. Khan's lab for their collaborative expertise and contributions in this work especially Shahab Mollah, Kamal Hussain and Samia Islam.

I must also thank my MS advisor Dr. Habib-ur-Rehman, Dr. Falak Sher, and Dr. Irshad Hussain with the rest of the faculty at Lahore University of Management and Science for their guidance in preparing me for graduate studies. Thank must also be paid to Mohammad Farooq Usman for his support during the last several years in every aspect of life.

ABSTRACT

Colloidal quantum dots (QD) are promising semiconducting materials to engineer photovoltaic and optoelectronic devices due to tunable size-dependent absorption and emission properties. These materials are important as they don't need complicated equipment and huge setup investment for industrial applications. If formulated into a kind of stable nano-ink, these QDs can be incorporated into devices using the most economical processing technologies, spray or roll to roll printing. More importantly, these are compatible with thin-film stacked devices and circuitry that can be formed on heat-sensitive and flexible substrates to make flexible wearable devices and sensors that are difficult to achieve with crystalline-based material in existence. QD processing technology consists of three main steps (I) Synthesis (II) Purification (III) and ligand exchange and device fabrication. With well-established synthetic procedures, great effort has been done on ligand exchange and device fabrication but there has been negligible attention given to purification strategies. Another major hurdle for their industrial applications is very short-lived post-ligand exchange QD solution stability that compromises the QD ink quality even before device fabrication.

This thesis is divided into six chapters. First, I will introduce QD chemistry, applications, and post-synthesis purification en route to device fabrication. Second, I'll introduce Gel Permeation Chromatography (GPC) as a purification technique in parallel to the established precipitation/re-dispersion (PR) method. This section will demonstrate the

effectiveness of GPC in removing byproducts and unbound ligands from PbS QDs, and the subsequent applicability of the GPC-purified QDs in optoelectronic devices. In the third and fourth chapters, I will present highly stable 3-mercaptopropionic acid (MPA) capped and halide capped PbS QDs, dispersed in a single non-coordinating organic solvent, to form printable p-type and n-type nano-inks. These inks are stable and suitable for making standalone, heterojunction, and p-n junction solar cell and photodetection devices. These inks should make QDs a viable option for industrial-scale manufacturing of QD devices through spray, or roll-to-roll printing processes. Chapter 5 will introduce $AgBiS_2$ based QDs ink as environment friendly alternative to eliminate toxicity concerns associated with the current state of the art PbS QD system. This ink has been utilized to fabricate flexible photodetectors to show its broad applicability in sensitive areas such as food processing and biomedical applications. Lastly, Chapter 6 of this thesis demonstrates scanning photocurrent microscopy (SPCM) as a diagnostic technique to characterize III-nitride (GaN/AlGaN) based high electron mobility transistor (HEMT) structures for growth defects and current conduction mechanisms via sub-bandgap excitation.

TABLE OF CONTENTS

LIST OF TABLES

LIST OF FIGURES

LIST OF ABBREVIATIONS

OA ..... Oleic acid

EDT 1,2-ethanedithiol

FTIR ..... Fourier transform infrared spectroscopy

GPC ..... Gel permeation chromatography

HTL ..... Hole blocking layer

ITO ..... Indium-doped tin oxide

LTF ..... Late Treatment Failure

MPA ..... 3-mercaptopropionic acid

PbS ..... Lead sulphide

PbO ..... Lead oxide

PbS ..... Lead sulphide

PV ..... Photovoltaic

QD ..... Quantum Dots

SEM ..... Scanning electron microscopy

SSLE ..... Solid state ligand exchange

SPLE ..... Solution phase ligand exchange

TEM ..... Transmission electron microscopy

TiO_2 ..... Titanium dioxide

ZnO ..... Zinc oxide

CHAPTER 1

INTRODUCTION TO QUANTUM DOT TECHNOLOGIES

1.1 A STATEMENT ON MOTIVATIONS

In the 21st century, climate change is the single largest threat to the global ecosystem, stemming from greenhouse gasses emission for energy production. Until we scale up the alternatives to fossil fuels, the world will continue to face two kinds of energy problems: access to energy that results in ~80% of global greenhouse gasses emission, and the lack of availability to hundreds of millions of people entirely, living remotely around the world[1]. It is predicted that the world's electric energy consumption will be doubled from today to ~30 TW (3×10^{13} W) by 2050[2]. Solar energy is a promising alternative to generate electricity at a large scale without impacting the environment. The current state-of-the-art available commercial technology is based on crystalline silicon, and widespread use of this photovoltaic (PV) technology at a global scale is limited due to its high per kilowatt-hour upfront cost. Another technical disadvantage of silicon-based PVs is, they can only harvest ~50% solar spectrum at best due to non-avoidable intrinsic losses, primarily related to the energy bandgap for photon absorption. Therefore, it is crucial to discover new materials with a smaller bandgap, either matching with the solar spectrum or employed in tandem, to achieve higher efficiencies to meet the modern-day demand for electricity at a lower cost.

The current electronics-driven era is founded on the semiconductor revolution based on high purity crystalline semiconductors. The desire to incorporate electronics everywhere and in every form has fueled the hunt for new materials enabling us for simple design and fabrication techniques for low-cost, flexible devices which are limited through current crystalline-based materials and fabrication tools[3].

Along these lines, inexpensive colloidally prepared quantum dots (QD), which are zero-dimensional nanocrystals of analogous bulk semiconductor crystals, exhibiting quantum confinement effects, offer a powerful platform for innovative device engineering[4–6]. QDs are promising light absorber material for PVs and optoelectronic applications, due to size-dependent, tunable bandgap, multi-exciton generation phenomena, and material processing that is compatible with a variety of flexible and heat-sensitive substrate and device fabrication techniques at a commercial scale[7]. Especially, for photovoltaic applications, the size-dependent tunable bandgap and diverse device configurations accessible with QDs can help in effectively harvesting the solar spectrum. For example, multijunction solar cells of compatible semiconducting materials with different bandgaps can act as tandem devices, breaking the Shockley-Queisser limit with theoretical efficiencies over 60%[8–10].

1.2 COLLOIDAL QUANTUM DOTS

A semiconducting material offers electronic and optical properties that can be modified through doping and chemical composition. A quantum dot is a nanocrystal of semiconducting material terminated by the surface ligand to preserve the particle size, that offers additional parameters of size and surface chemistry controlled optical and electronic properties[11,12]. These unique properties are stemming from large surface area and

quantization effect within nanocrystal enabling us to engineer nanomaterials with controlled absorption and emission spectrums, and electronic charge transport[13]. The absorbance of the above bandgap photon creates an electron-hole pair, that are free to move in the bulk of the semiconductor's conduction and valence band respectively. In materials with high dielectric constants, electron-hole pairs can get bound by weak coulombic force to form an exciton that is analogous to electron and proton in the hydrogen atom. This distance between charge carriers is known as Bohr's exciton radius (***R_B***):

$$R_B = \frac{\hbar^2 \mathcal{E}}{q^2 m^*_{e,h}} \qquad \text{Eq.1.1}$$

Here, ***ε***, ***ħ***, ***m*$_{e,h}$***, and ***q*** are dielectric constant, reduced Planck constant, reduced mass of holes and electrons, and elementary charge constant, respectively[14,15]. As we reduce the size of semiconducting nanocrystal below the Bohr radius, the motion of charge carriers becomes confined and the energy level become discrete, which results in increased and size-dependent bandgap. The ***R_B*** for several commonly explored QD materials is: 5 nm for CdSe, 5nm for $AgBiS_2$, 15nm for InP, 15nm for PbS, and 34nm for InAs. That means particles of these materials smaller than their ***R_B*** will exhibit strong quantum confinement.

1.3 PbS-QUANTUM DOTS

Due to technological relevance, low cost and large Bohr exciton radius, which offer strong quantum confinement effect and tunable bandgap across the shortwave to near-infrared range (0.4eV-2eV), PbS QDs have been intensely studied as a model platform for colloidal QD optoelectronics[9]. More importantly, many published examples are available for straightforward and well-established synthetic methods and material properties comparison that govern device performance[16]. We will use PbS-QD system to investigate

effect of purification on charge transport in Chapter-2 and explore new strategies to formulate QDs based solution processable inks for broad technological and industrial applications in Chapter-3 & 4.

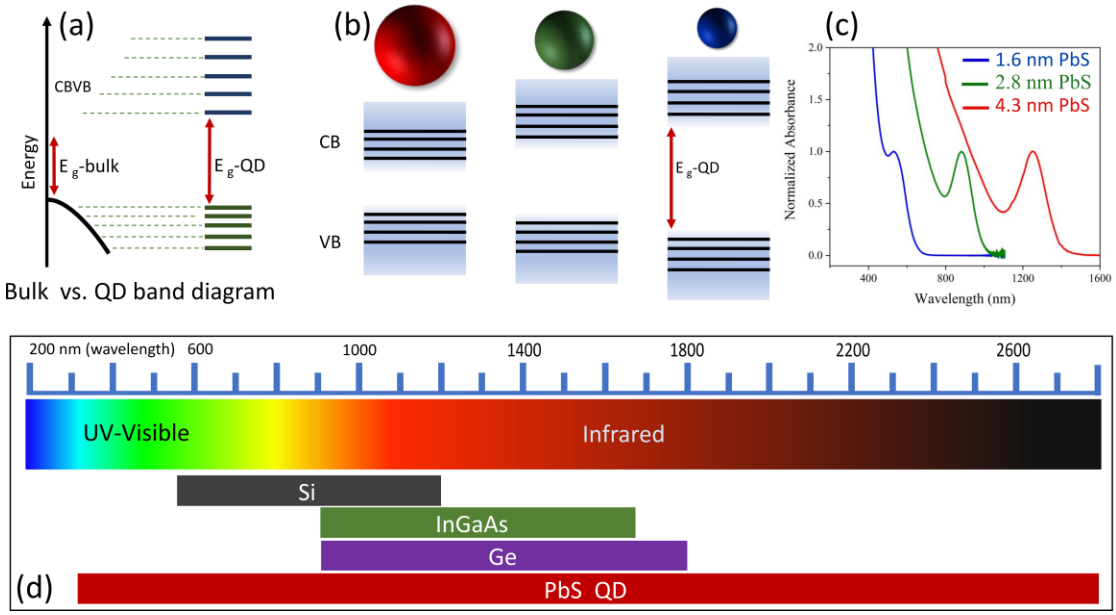

Figure 1.1: *Concept graphics for (a) energy band diagram of bulk semiconductor and quantum dot (b) size dependent bandgap diagram for quantum dots (c) size dependent absorption profile of PbS QDs in solution (d) bandgap comparison of crystalline based materials and PbS QDs*

1.4 GREEN QUANTUM DOTS ($AgBiS_2$)

In many parts of the world there is now, or soon to be, legislation to restrict, and in some cases ban certain toxic heavy metals in consumer and household appliances such as lighting equipment, consumer electronics, leisure & sports equipment. Therefore, for colloidal quantum dots to be commercially viable in many applications, they must not contain any controlled heavy elements like mercury (Hg), Cadmium (Cd) and lead (Pb). Therefore, there is a need to explore less toxic and environment friendly QD systems[17].

In last years, $AgBiS_2$ nanocrystals with a narrow bulk bandgap of ~0.8 eV, and a large absorption coefficient ~10^5 cm^{-1} have emerged as an appealing eco-friendly candidate for

NIR-Photodetectors and solar cell applications. In Chapter 5 of this thesis, we have extended the research concepts learned from PbS QDs to $AgBiS_2$ demonstrating its general applicability for any such colloidal nanocrystal system[18].

1.5 COLLOIDAL QUANTUM DOT APPLICATIONS

Solution processable colloidal quantum dots can be incorporated in solid state devices to convert photon flux into electric power and to modulate and transmit charges under bias in photodetectors, field-effect transistors (FET), and in novel hybrid devices **Figure 1.2** [3,4,19,20]. In principle, a solar cell (PV) is a device that converts light energy into electrical energy in a single-step fashion. Above bandgap absorbed light creates photoexcited electron and hole that are then separated and transported through the QDs matrix for collection at opposite electrodes.

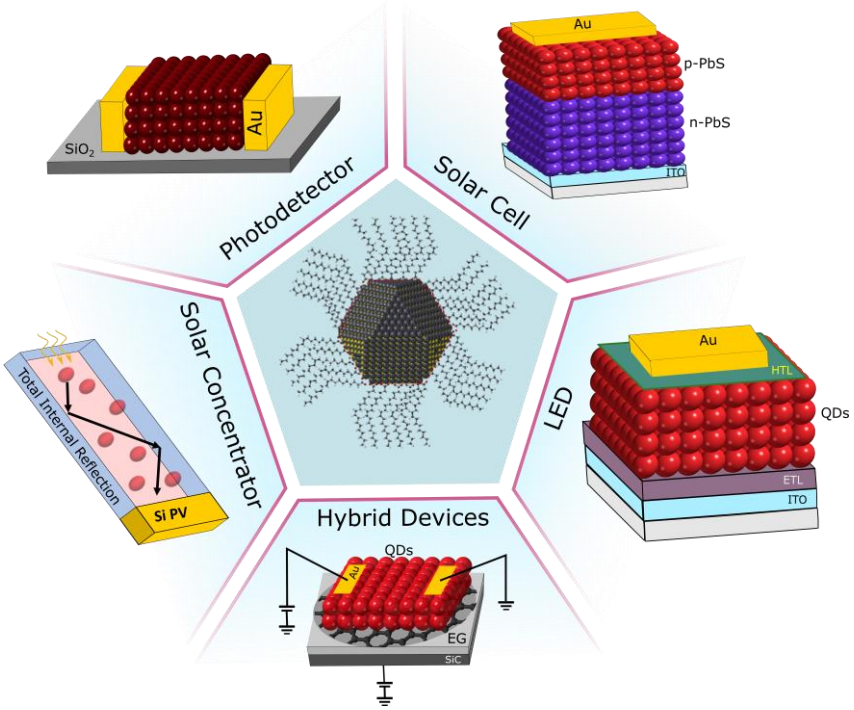

Figure 1.2: *Potential applications of colloidal quantum dots in energy harvesting and photodetection devices*

In photovoltaic applications, there are several possible device architectures to employ QDs as absorber materials but the most common architectures are metal-semiconductor (Schottky junction), heterojunction, and p-n junction solar cells. **Figure 1.3** depicts the architectural view and band diagram for few of these devices.

QD with strong optical absorption and tunable bandgap (e.g. ~0.4eV-2eV for PbS) are ideal light absorbing material for Near-infrared light detection. Multispectral detectors operating in near-infrared, visible, and ultraviolet regimes can easily be engineered in a single non-cooling device on flexible and heat-sensitive substrates[21]. Photoconductor and photodiode are the two most common device architectures for QD photodetectors, later being preferred due to low dark current and higher detectivities.

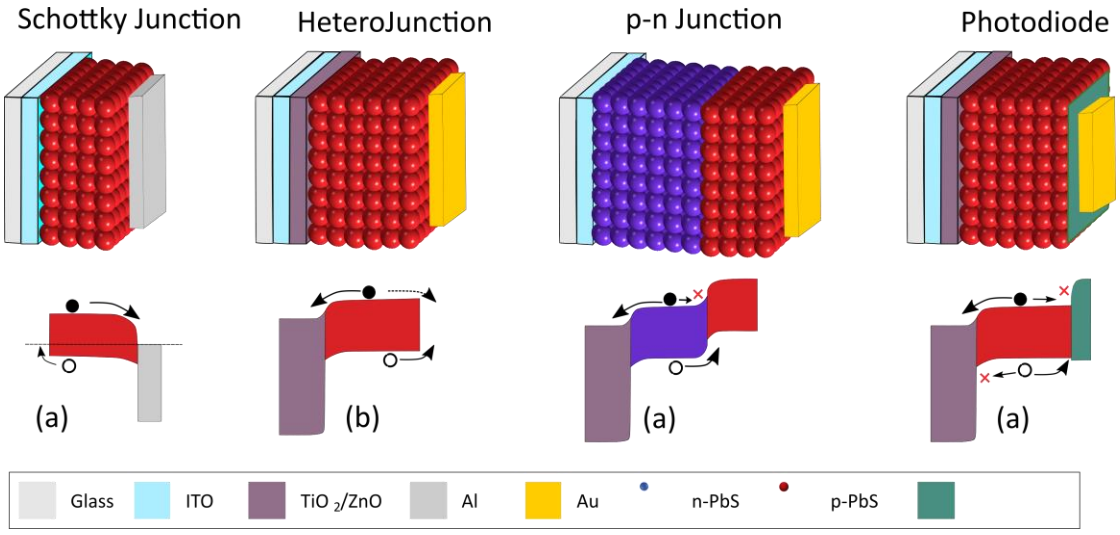

Figure 1.3: *Concept graphics for various QD photovoltaic device configurations with respective band diagram indicating working mechanism and flow of charges*

1.6 COLLOIDAL QUANTUM DOT SYNTHESIS

Monodispersed organically passivated QDs are synthesized through a bottom-up (assembling atoms to form the desired nanostructures) approach to obtain large quantities of QDs, inexpensively. In this process, precursors are rapidly mixed in a non-coordinating

solvent, at elevated temperatures (~80- 200°C), in the presence of surface capping ligand molecules (e.g. oleate) **Figure 1.4**[22,23]. The process involves a short nucleation phase during the supersaturation condition when precursors are mixed. This nucleation relieves the supersaturation and prevents further nucleation, followed by a slower, controlled growth phase on top of those initial nuclei[24]. The use of mixed precursors results in alloy type NCs[18], though the final composition is rarely a direct function of initial precursor stoichiometry: an example is $AgBiS_2$ NCs, for which a detailed synthesis process is given in Chapter-4.

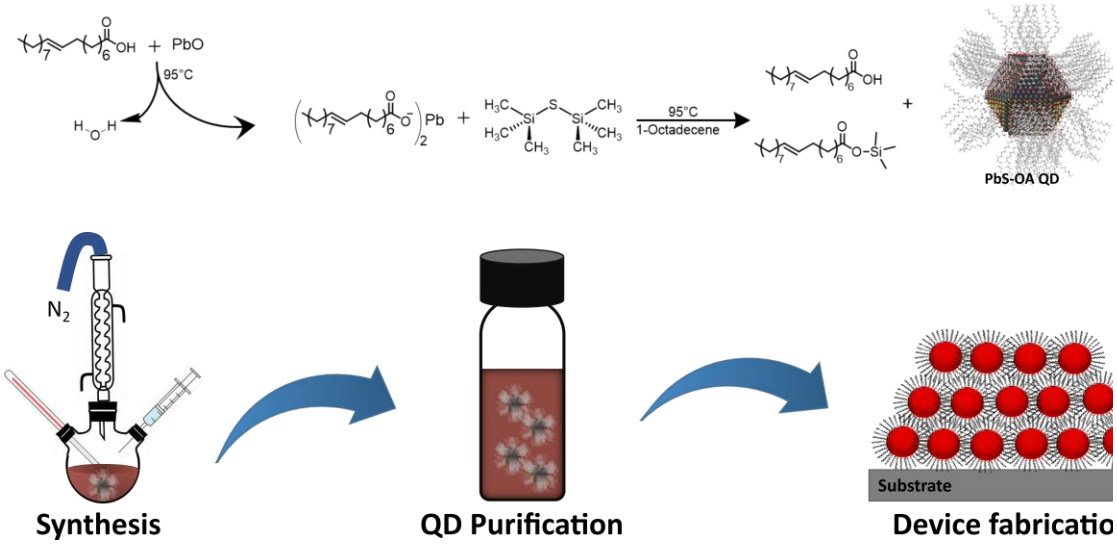

Figure 1.4: *A reaction scheme for PbS QD synthesis and assembly of these QDs into thin film devices*

1.7 COLLOIDAL QUANTUM DOT PURIFICATION

QDs are synthesized in high boiling point non-coordinating solvents in the presence of access of capping ligands. In order to assemble QDs into functional devices, post-synthesis purification is required to get rid of growth solvent, reaction byproducts and residual precursors. There are several purification methods available but precipitation-redispersion (PR) is the foremost used technique in QD research.

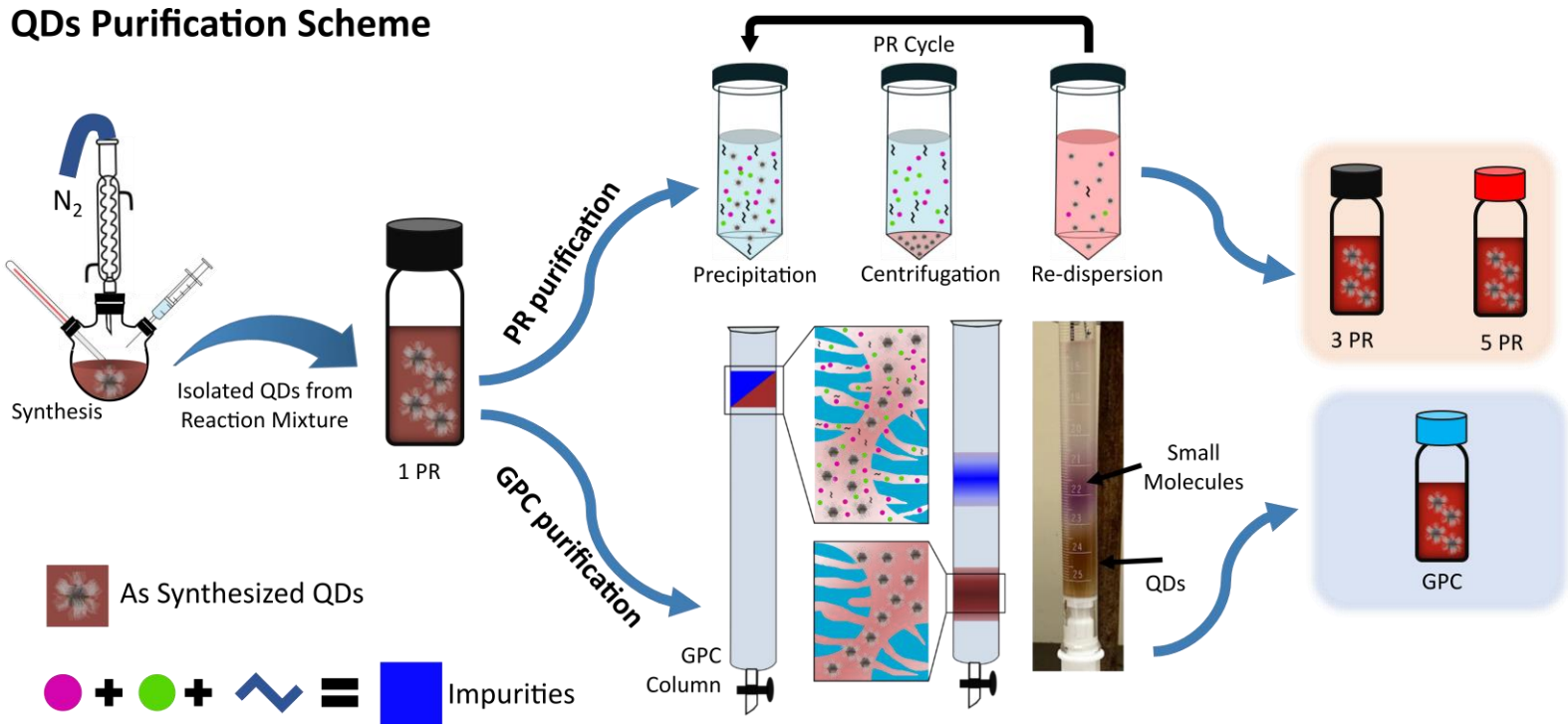

Figure 1.5: *QD purification process comparing precipitation and redispersion (PR) (on top) and Gel Permeation Chromatography (GPC) on bottom. (a) the loading of crude QD sample into the column, inset depicting microscopic view of porous stationary phase (b) separation of QD and impurities on the basis of their rate of elution, QD being larger in size eluate faster (c) visualization of purification process, blue dye was added to mimic and provide visuals for small molecules.*

PR process involves the addition of anti-solvent for QD agglomeration, separation through centrifugation, and redispersed of QDs in neat solvent again23. Such a single PR cycle is insufficient to get a clean product and must be repeated several times that leads to inconsistent ligand quantification and may result in loss of native ligands bound to the surface. The exposure to harsh polar solvent and forced aggregation during a PR cycle, can induce irreversible damage to QDs surface, causing poor size distribution, and particle coalescence to form trap states for charge carriers. This presents a tradeoff between QD's surface degradation and removal of reaction by-products[25]. The Greytak group has established gel permeation chromatography (GPC) as an effective way to purify colloidal quantum dots that can break this tradeoff. GPC is a size exclusion chromatography that separates analytes on the basis of size through which larger particle elutes faster than smaller. It effectively separates QDs from byproducts and unreacted precursors with a very consistent ligand population and surface chemistry. Thus, following purification, the population of native ligands can be quantified[26–30]. As, the surface chemistry of CQDs dictates the electronic parameters of material, establishing a well-defined initial state of purified CQDs is a valuable starting point to study the effect of surface modification and different device fabrication methods on charge transport in QDs based devices. A comparison between PR and GPC purification strategies is depicted in **Figure 1.5**. Chapter-2 of this thesis describes the effect of these purification routes on optoelectronic properties of PbS QD solids

1.8 LIGAND EXCHANGE PROCESS

Nanocrystalline cores are passivated by long-chain ligands [typically, oleic acid OA] to control the growth process, passivate the surface, and maintain their colloidal

stability. However, the presence of these capping ligands directly influences the conductivity in assembled QD solids, that greatly depends on the separation between neighboring NCs. Long-chain ligands (~2nm OA) form an insulating layer and act as tunneling barriers for charge carriers resulting in a weak coupling between the individual QD, as the wave function of the charge carriers in each QD is still effectively confined within the nanocrystal. To achieve better device performance, the basic requirement is to reduce interparticle distance and fabricate densely packed, compact, and crack-free films[11]. This is a primary requirement to promote not only band-like transport but it also favors the hopping of charges from on crystal to another within film matrix[3,31,32]. It was realized that post-synthetic treatments are inevitable to increase the optoelectronic performance of the CQDs-based device that can be achieved by replacing the bulky ligands with shorter and more conducting smaller molecules through a ligand exchange step. There are a variety of smaller thiols, amines and carboxylate type molecular ligand examples available in literature along with inorganics anionic ligands e.g., (Cl^{-1}, Br^{-1}, I^{-1}), SnS_4^{4-}, $SnTe_4^{4-}$ and MoS_4^{2-} are the most notable examples[6,9]. These new ligands can be installed on QD by: (i) solid-state ligand exchange (SSLE) or (ii) Solution phase ligand exchange (SPLE). These ligand exchange processes are compared in **Figure1.6**. The solid-state ligand exchange process consists of, assembling QD film onto the substrate with native ligands, introducing secondary ligand by dropping or amercing in secondary ligand solution, and rinsing off exchanged and free ligands. This process is convenient when the incoming ligand has very high reactivity. But a complete ligand exchange is implausible as QDs have limited degree of freedom and are tightly held onto the substrate.

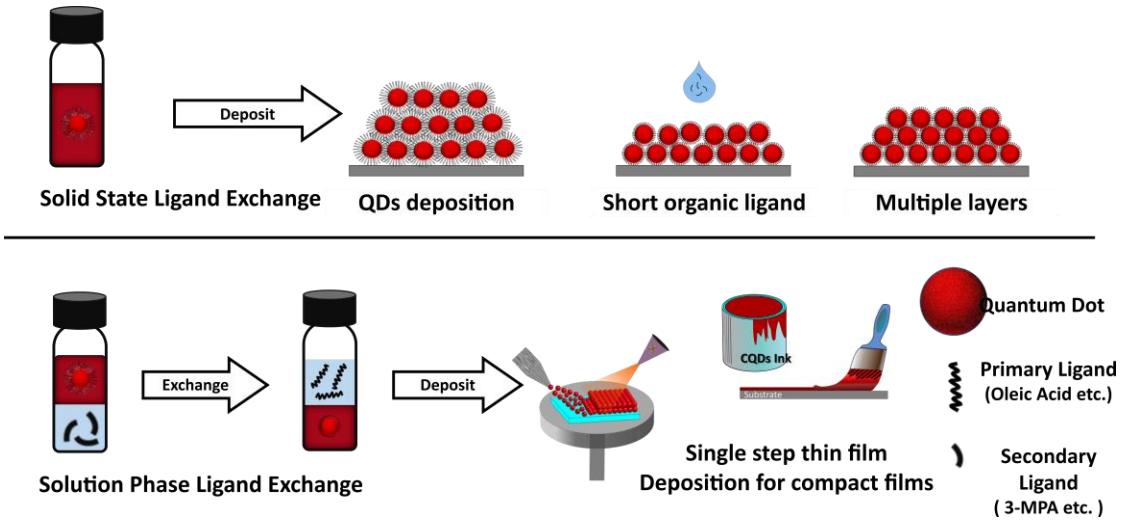

Figure 1.6: *Ligand exchange processes (top) solid state exchange process flow chart (bottom) solution-phase exchange process and film fabrication process*

This process also results in uneven morphology, voids, and cracks that are inevitably formed due to mass lose by replacing long-chain ligands with shorter molecules. In order to overcome these problems, SSLE process is repeated several times, successively filling the gaps from previous layers to make a compact and uniform film. Along these lines, SSLE process is not compatible with large-scale industrial applications as only about 1% of synthesized QDs end up being incorporated into devices and repetitive nature of ligand exchange step[33]. To overcome these issues, solution-phase ligand exchange is an inexpensive approach that is compatible with high output and large-scale industrial applications. In SPLE, ligand exchange is done in the solution phase to formulate quantum dot inks that can be directly incorporated into devices through more conservative spray or roll-to-roll printing techniques for large area deposition for mass scale photovoltaic applications[34].

1.9 CHARGE TRANSPORT IN QD SOLIDS

A single Quantum dot can be modeled as a site-localized wave function and with long chain bulky ligands, charge transport can only occur through hopping from one dot to another. As the inter particle separation decreases by replacing long chain ligand with smaller molecules, it improves the packing of the films and the neighboring wave functions start to overlap generating some extended states which improves "through the band" transport, while close packing of QD also enhances the tunneling transport between localized QD states. Just like in atomic solids, in QDs, interactions between the electronic wave functions of nearby CQDs decrease exponentially with inter-dot spacing[32,35]. On nanometer scale, QDs can be locally ordered, long-range-ordered or super crystals that also increase the charge mobility from locally ordered to long rang ordered crystals[36]. Another major factor in charge mobility is surface defects, which can arise from lattice defects or grain boundaries. Carrier trapping at surface defects can also cause increased non-radiative recombination. Reversible carrier trapping in shallow trap states is one of the main origins of hysteresis and deteriorates the carrier lifetime which is a key parameter in determining the charge transport in QDs[37,38].

Bulk conductivity **"σ"** (1/resistivity "**ρ**") is a simplest parameter to assess the ease of charge transport in assembled solids.

$$\sigma = nq\mu_e + nq\mu_h \qquad \text{Eq.1.2}$$

Here $\boldsymbol{n}$ is the intrinsic carrier density, $\boldsymbol{q}$ is elementary charge, and "$\boldsymbol{\mu_{e,h}}$" is the charge mobility for electron and hole respectively. The transmission line model (TLM) measurement technique, is a direct approach to measure film resistance separately from

contact resistance. In this technique, resistance is measured between pairs of neighboring, parallel contacts with increasing spacing.

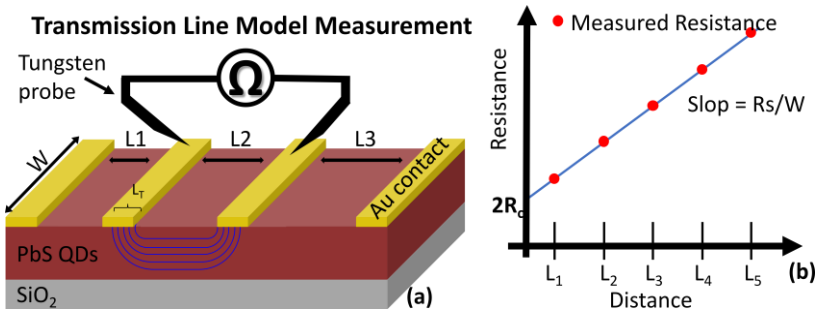

Figure 1.7: *A sketch of TLM device and measurement setup*

The slope of resistance versus device length is nominally the resistance per unit length, equal to ***Rs/W***. Here, ***Rs*** is sheet resistance and ***W*** is width of the contacts. As the film thickness is known, the bulk resistivity for the film can be obtained as:

$$1/\sigma = \rho = R_S . d_{QD} \qquad \text{Eq.1.3}$$

Here $\boldsymbol{d_{QD}}$ is the film thickness[39].

For a photoconductive device, with ohmic contacts, the linear increase in photoresponse is an indicator of photoconductive gain ($\boldsymbol{g}$), that can be obtained from directly measured responsivity ($\boldsymbol{R}$). Responsivity is the performance of a photodetector in term of photocurrent generated per unit incident optical power at given wavelength. The gain ($\boldsymbol{g}$) a photodetector is in direct relation to the responsivity and external quantum efficiency (EQE) of the device under monochromatic illumination as:

$$g = \frac{R . E_{ph}}{1 - 10^{-A}} = \frac{EQE}{1 - 10^{-A}} \qquad \text{Eq.1.4}$$

Here E_{ph} is the photon energy in eV and A is the absorbance of the film at the excitation wavelength, neglecting scattering and reflection. In general, the photoconductive gain can contain contributions from both electrons and holes:

$$g = \frac{V}{L^2}(\mu_e + \mu_h)\tau_{rec} \qquad \text{Eq.1.5}$$

Here μ_e and μ_h are the electron and hole mobilities, respectively, V is the applied voltage, and L is the length of the device in the direction of transport[40]. Charge transport in QD is often time reported in terms of charge carrier mobility $\mu_{e,h}$. Mobility is defined as the movement of charges under applied potential or in simple words, it is the ease with which charge carrier can travel through a material. Generally, the photoconductive gain can contain contributions from both electrons and holes and so the resulting mobility.

$$\mu = \mu_n + \mu_p \qquad \text{Eq.1.6}$$

In practice, one carrier may become rapidly localized in low-mobility traps, in which case, $\mu\tau_{rec}$ is determined by the more mobile carrier, which continues to cycle additional charges through the device until the ground state is recovered through recombination. This more mobile charge carrier is referred as majority carrier and the associated mobility can be estimated by:

$$\mu = \frac{L^2}{V\tau_{rec}}.g \qquad \text{Eq.1.7}$$

Along with several other techniques available in literature, researcher have measured the mobility of charges using back-gated I-V measurements of field-effect transistor (FET) structure fabricated on SiO_2 dielectrics with conductive Si substrates assuming FET is biased in triode region of output characteristics. However, the field-effect

mobility may not accurately describe the behavior of charge-collecting devices due to limitations associated with carrier density, estimation of gate capacitance particularly in films that may experience compensation due to mobile ions or high trap density, and dependence of contact resistance on gate voltage near pinch-off[41]. In contrast, we have used directly measured, photoconductive gain and recombination lifetime to estimate carrier mobility for majority carriers in ohmic devices using ***Eq. 1.7***.

In order to extract the mobility of minority carriers, the diffusion length ($\boldsymbol{L_D}$) paired with lifetime in rectifying devices was used to estimate minority carrier mobilities. The details of these techniques are given in Chapter-2. The minority carrier diffusion lengths in lateral rectifying devices can be measured using scanning photocurrent microscopy.

1.10 SCANNING PHOTOCURRENT MICROSCOPY

In semiconductors, the mobility of charges depends is intrinsically related to two properties, the diffusion length and carrier life time:

$$\boldsymbol{\mu = \frac{qL_D^2}{\tau_n k_B T}} \qquad \text{E}q.1.8$$

In this study we have focused on the charge carrier mobility and effecting factors specially, diffusion length and carrier life time. Diffusion length ($\boldsymbol{L_D}$) is a lateral distance that a charge carrier is able to move in its lifetime before recombination or absorbed by a trap state. In case for QDs, it is characteristics for each material, depending on synthesis, packing and inter-particle distances. Scanning photocurrent microscopy (SPCM) is a versatile experimental technique that offers a wealth of information about optoelectronic properties of these semiconducting materials, including charge transport dynamics[42–44]. Analogous to other scanning probe microscopy techniques, SPCM uses above bandgap focused light beam instead of a probe tip to excite the material locally to generate electron-

hole pairs. The excitons are then (electrons and holes) free to relax, recombine, drift, and diffuse. If these carriers reach the electrodes before recombination, a photocurrent signal is observed. The resultant photocurrent is plotted as a function of position on the device to from a two-dimensional image. The collected photocurrent can be modeled by simple 1D exponential curve as a function of distance x_o[45].

$$I_{ph} = \frac{eG}{2} \exp\left(\frac{-x_o}{L_D}\right) \qquad \text{Eq.1.9}$$

Here, G is the charge carrier rate of generation, e is the electron charge, and L_D is diffusion length, which can easily be extracted by fitting the photo current without the need of any other charge transport parameter.

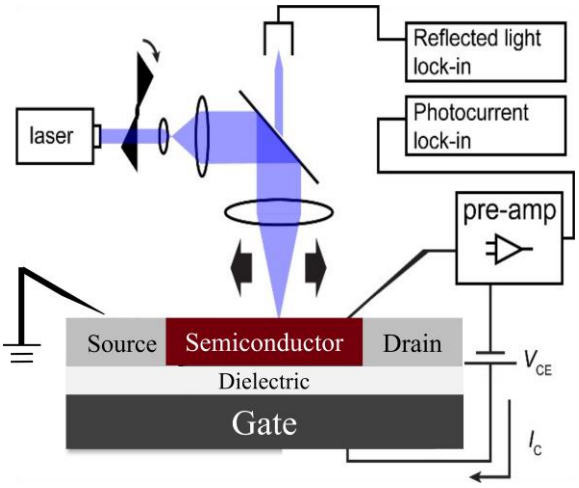

Figure 1.8: *Scanning photocurrent microscopy experimental setup*

1.11 THESIS OVERVIEW

Colloidal quantum dots (CQDs) are promising semiconducting materials to engineer photovoltaic and optoelectronic devices due to tunable size-dependent absorption and emission properties. There has been negligible attention given to purification strategies and systematic efforts to find the ideal ligand populations to optimize device performance.

In first chapter of this thesis, gel permeation chromatography (GPC) will be introduced as as a purification technique and its effectiveness in removing byproducts and unbound ligands from PbS QDs and subsequent applicability in optoelectronic devices. It was shown that post synthetic purification and optimum ligand population can significantly impact physical characteristics device performance.

In second and third chapter, this thesis presents highly stable 3-MPA capped and halide capped PbS QDs dispersed in a single non-coordinating organic solvent. These p-type and n-type inks are stable and suitable for making standalone, heterojunction and p-n junction solar cell and photodetection devices using drop casting, spray, or roll-to-roll printing processes.

Over the last decade, inorganic QDs, for example PbS and CdSe QD systems have been explored but environmental regulatory concerns have been raised due to toxic heavy metals in such materials, opening an opportunity for exploration of environment friendly alternatives such as $AgBiS_2$. Chapter-4 will describe electrostatically stabilized 3-mercaptopropionic acid (MPA) capped $AgBiS_2$ QDs dispersed in organic solvent that are stable over a period of weeks or longer. These inks should be suitable for making NIR-photodetectors on flexible and heat sensitive substrates using spray or roll to roll printing techniques for food processing and biomedical applications.

Last Chapter of this thesis discuss the scanning photocurrent microscopy (SPCM) as a diagnostic technique to characterize III-nitride (GaN) based High Electron Mobility Transistor (HEMT) structures for growth defects and current conduction mechanism.

CHAPTER 2

IMPROVED CHARGE TRANSPORT IN PbS QUANTUM DOT THIN FILMS FOLLOWING GEL PERMEATION CHROMATOGRAPHY PURIFICATION*

1.1 INTRODUCTION

The desire to incorporate improved and broadly deployable photodetectors and photovoltaics in daily life has fueled the hunt for new materials which enable simple design and fabrication techniques for low-cost, flexible, and large area semiconductor devices[46–48]. Semiconducting colloidal quantum dots (QDs), which are zero-dimensional, nanoscale crystals of analogous bulk semiconductors, offer a versatile platform for engineering photovoltaic devices, displays and flexible electronics[3,49,50]. QDs are promising semiconducting materials for electronic and optoelectronic devices due to tunable size-dependent band gap, multi-exciton generation, and high achievable quantum efficiencies[51,52].

In traditional solution-based synthesis of QDs, long chain organic ligands (e.g. oleate) are used as surface capping agents to preserve size and prevent aggregation[51,53]. Great efforts have been made to find suitable short-chain surface ligands to reduce spacing between adjacent QD's and improve charge transport in optoelectronic devices [54–57]. To

*Reprinted with permission from Ahmed, F.; Kelley, M. L.; Chandrashekhar, M.; Greytak, A. B. Improved Charge Transport in PbS Quantum Dot Thin Films Following Gel Permeation Chromatography Purification. The Journal of Physical Chemistry C 2021 125 (32), 17796-17805 DOI: 10.1021/acs.jpcc.1c04218

build devices out of QDs, post synthesis reaction byproducts and residual precursors are removed by multiple precipitation and redissolution (PR) cycles. The PR technique uses polar anti-solvents that can promote QD aggregation.[58] Multiple PR cycles result in loss of native ligands bound to the surface, which can induce surface traps that degrade the optoelectronic performance of the dots.[59–63] Ligands also inhibit coalescence, which has been shown to lead to electronic traps in QD films.[64] This presents a tradeoff between QD agglomeration and removal of reaction byproducts and residual precursors through multiple PR cycles. Greytak group has shown that post-synthesis purification of QD's by gel permeation chromatography (GPC) can break this tradeoff.[26,65–67] GPC is an effective way to separate analytes on the basis of size, through which larger particles elute faster than smaller ones. It effectively separates QDs from byproducts and unreacted precursors, while reproducibly preserving ligand surface termination. GPC also prevents agglomeration by keeping QDs dispersed in a homogenous solvent environment during purification. Post synthesis purification steps are particularly crucial in solid state ligand exchange and film fabrication(SSLE) where diffusion of ligands, impurities, and QDs is limited within the deposited film.[68] While GPC purified QDs have been employed in electronic devices, film's electronic properties including conductivity, photoconductivity, and photocurrent lifetimes have not been directly examined in SSLE films prepared following GPC or compared to similar films prepared following PR. Such comparisons are necessary as effective purification strategies could help eliminate factors such as cracks, surface traps, and coalescence of QDs can that degrade QD film performance.

Because PbS QDs offer effective bandgaps tunable across the shortwave to near-infrared range, and synthetic methods with good control of size distributions have been

developed, PbS QDs have been intensely studied as a model platform for colloidal QD optoelectronics.[13,49,69] For example, spin-casting of oleate-coated PbS QDs followed by ligand exchange with ethanedithiol (EDT) can be used to build films with *p*-type character that can be employed in representative Schottky-barrier and oxide heterojunction photovoltaic devices.[70] A variety of techniques have been applied to learn material properties (such as carrier type, density, mobility, and lifetime) and interfacial properties (such as contact resistance and contact potentials) that govern device performance, and how these properties can be influenced and improved by attention to preparative techniques. Many of these studies focus on vertical device architectures common to thin-film photovoltaics.[71–74] While clearly advantageous for many applications, vertical architectures present some limitations for isolating the behavior of individual junctions. Lateral transport devices, in which current moves in the plane of the thin film, have been investigated primarily in field-effect transistor studies[70,75] that permit measurement of majority-carrier mobility at high carrier densities that may not be representative of excited-state carrier dynamics in optoelectronic devices. But, lateral transport devices also provide the opportunity to separate junction behavior from bulk properties through varying contact separation in transmission line model (TLM) studies[76] and through localized photocurrent and photovoltage measurements at metal-semiconductor interfaces.[44,75,77] For example, scanning photocurrent microscopy (SPCM) has been used by Law[77] to characterize the effect of gating on minority carrier diffusion length in PbSe QD FETs, and by Strasfeld[44] to resolve ohmic and Schottky contacts to PbS QD films. The former examples use films deposited over pre-patterned bottom contacts, but this can lead to uneven film thickness

and one study found that top-contacts exhibited significantly lower contact resistance in TLM measurement of CdSe QD films.[76]

Here, we employ laterally patterned top contacts to directly compare the performance of PbS-EDT films prepared following GPC purification and conventional PR cycles in photoconductive and rectifying optoelectronic devices, and to permit comparison to state of the art literature results. The overall experimental approach for QD film formation using layer-by-layer spin coating and ligand exchange of GPC-purified PbS QDs is outlined in **Figure 2.1**.

2.2 COLLOIDAL QUANTUM DOT PURIFICATION

Oleate-capped PbS QDs with a lowest energy electronic transition λ_{1s} ~1250 nm corresponding to a diameter ~4.4 nm, were synthesized through a previously described, air free synthetic route in 1-octadecene solvent,[78] and subsequent purification, film deposition, and ligand exchange steps were conducted in an inert atmosphere. Following synthesis and an initial precipitation under nitrogen atmosphere using anhydrous methyl acetate (MeOAc, dried over activated 4A molecular seives), the QDs were redissolved in toluene to form a stock solution designated as 1PR. A portion of QDs from the 1PR stock solution were brought through two further PR cycles, filtered through a 0.1µm PTFE syringe filter, and brought to a final concentration of 25mg/mL in anhydrous toluene (3PR). Similarly, a portion of the 3PR sample was brought through two further PR cycles (5PR). Separately, from the 1PR stock solution, 250 nmol of PbS QDs were purified using gel permeation chromatography (GPC).[66,79]

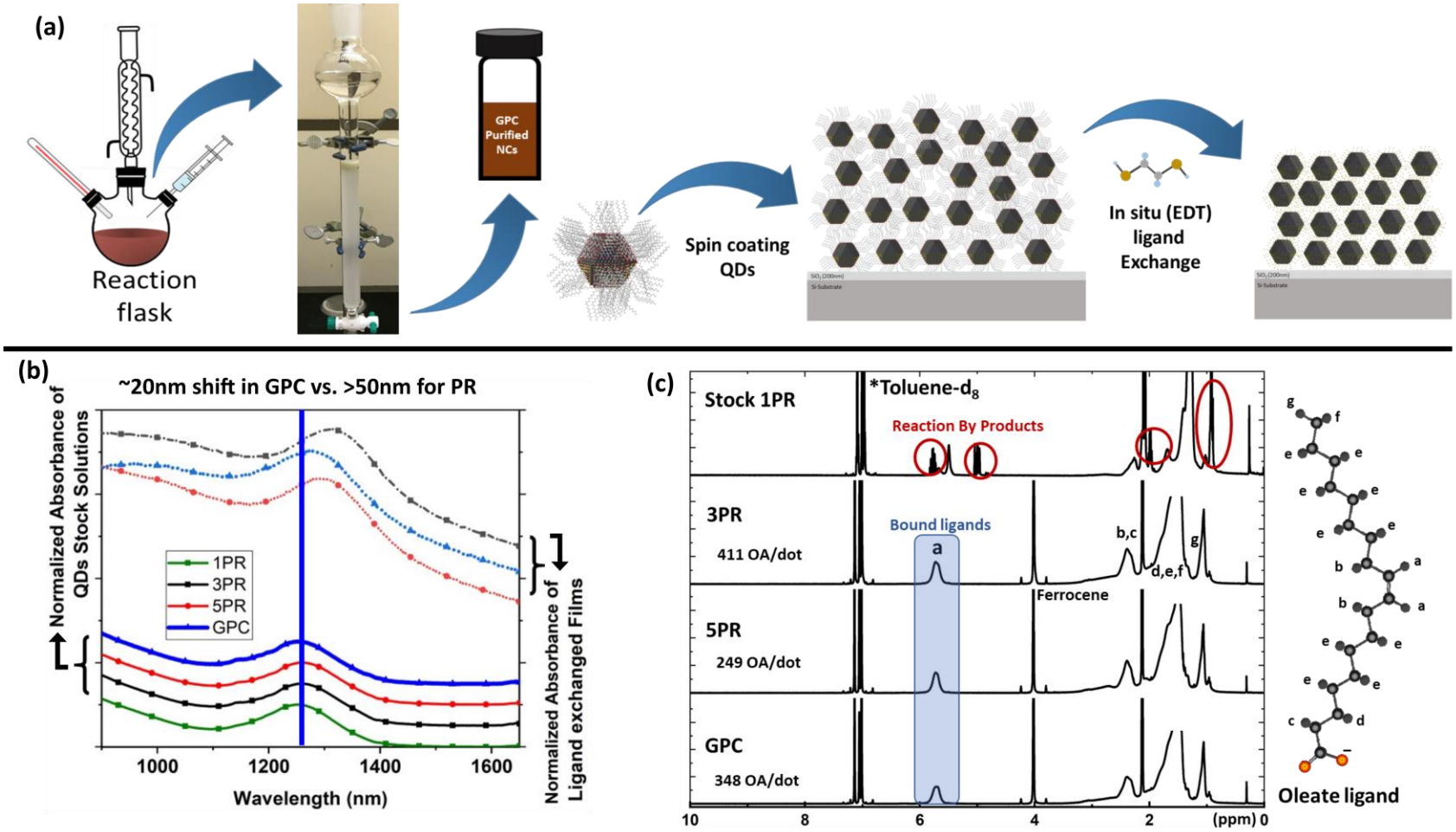

Figure 2.1: *(a) Synthesis and purification route to make spin coating layer by layer film fabrication and ligand exchange process to make compact QD film. (b) Absorbance of QDs after synthesis, purified solutions and ligand exchanged films. (c)* ^{1}H *NMR spectrum of Stock (1PR) and purified (3PR, 5PR & GPC) QDs solutions*

The eluted fractions containing QDs were combined and concentrated by removing excess solvent under partial vacuum to achieve a final concentration of 25mg/mL, and then passed through a 0.1 μm filter, to obtain the GPC sample used in subsequent work. For GPC, the polystyrene gel (Bio-Beads S-X1, Bio-Rad), were prepared following Shen et al[79]. In particular, beads were washed three times with an excess of toluene and swollen under ambient conditions in toluene for 24 hours. These swollen beads were washed again with fresh toluene and then evacuated to dryness under Schlenk line vacuum before transferring into the glovebox. The beads were swollen a second time with anhydrous toluene inside the glovebox for another 24 hours before loading onto the column as described previously. In a typical run, the 1PR aliquot was concentrated to a 200 μL volume under partial vacuum prior to injecting onto the column.

2.3 FILM FABRICATION

Conductive PbS QD films were formed on Si/SiO_2 substrates (wet oxidized, 200 nm thickness). Chips of ~1 cm^2 were cleaned by sequential sonication in acetone, isopropanol, ethanol, and DI water, and finally dried under N_2 flow. Substrates were heated at 120°C for 10 min to remove adsorbed water before transferring into the glovebox. QD films were deposited using a layer-by-layer deposition and ligand exchange process. Each coating cycle consisted of dropping 20 μl PbS solution onto the substrate while spinning at 3000 rpm followed by treatment with 3 drops of 1.0% (v/v) 1,2-ethanedithiol in acetonitrile and rinsing with 3 drops of fresh acetonitrile and 3 drops of anhydrous toluene. Each deposition, ligand exchange and cleaning step is 30 sec apart and done in nitrogen filled glovebox, using compact spin coater constructed from a hard drive motor and operated by an Arduino microcontroller. This coating cycle was repeated four times to get

a ~100 nm thick PbS QD film. Metal top contacts were evaporated through a shadow mask using an e-beam evaporator. The completed devices were then immediately tested for optoelectronic properties under normal atmosphere conditions, using tungsten wire probe arms mounted on a scanning stage.

2.4 RESULTS & DISCUSSION

Initial analysis of samples by ultraviolet-visible-near infrared (UV-vis-NIR) absorption spectroscopy was used to monitor lowest-energy electronic transition peak wavelengths, effective diameter according to a published calibration curve, and relative concentration. For these measurements samples are diluted in *n*-octane under N_2. As shown in **Figure 2.1(b)**. Full spectrum of these solution and fabricated films are given in **Figure 2.2.** The different purification methods led to minimal change in the absorption spectrum, indicating no great change in effective diameter or size distribution. However, UV-vis-NIR does not probe ligand populations associated with the QDs.

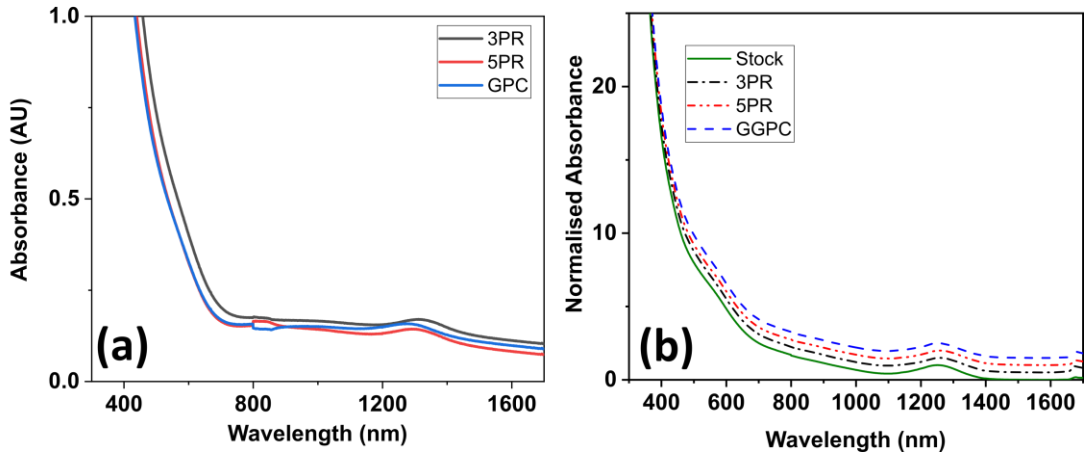

Figure 2.2: *(a) Thin film UV-vis-NIR absorbance spectrum of PbS-EDT deposited on glass substrates (b) Solution phase UV-vis-NIR absorbance spectrum normalized and offset at λ_{1S} peak by 0.5*

NMR is a standard and essential technique for the analysis of organic ligands on QD surfaces and presence of unwanted impurities. Ligands attached to the surface of QDs characteristically exhibit broadened NMR spectral lines that can be distinguished on the basis of width and chemical shift from sharp peaks associated with freely diffusing small molecules.[80] The olefin resonance of oleate ligand species is well resolved from crowded aliphatic and aromatic protons associated with solvent, and can be used to quantify total oleate concentration when ferrocene is used as an internal standard. We have shown previously that GPC purification leads to highly repeatable ligand populations, characterized by a single resolvable olefin peak in purified oleate-capped PbS QD samples below a critical size of ~5 nm, which includes those examined here.[66] Conversely, studies of PbS QDs purified with PR have indicated a diminishing ligand population with repeated PR cycles, attributed to dissociation of physisorbed material and/or dissociation of lead oleate equivalents from weakly bound coordination sites: these changes can occur with minimal effect on the electronic absorption spectrum.[56,81–83] NMR spectra for 3PR, 5PR, and GPC samples **Figure. 2.1(c)** all show complete removal of residual octadecene growth solvent, unreacted precursors, and reaction byproducts and of narrow peaks associated with free or weakly associated oleate species. Yet, the bound surface ligand population per QD, as determined by integrating peaks for bound oleate in spectra of to establish total ligand concentration and dividing by the QD concentration from a UV-vis-NIR absorbance measurement, shows differences among the three samples. GPC QDs showed 348 OA/dot ligand population. The 3PR sample shows a slightly higher number, while 5PR cycles led to additional ligand loss down to ~249 OA/dot. The lower number for 5PR could indicate bare sites, which could promote agglomeration. We note that close inspection of the UV-

vis-NIR absorption spectra of solution-phase samples in **Figure. 2.1(b)** shows a small redshift in λ_{1s} peak after successive PR cycles. The ligand population determined for the GPC sample is in line with our previously determined ligand density versus size measurements for PbS QDs.[66] We also analyzed purified QDs sample using thermogravimetric analysis (TGA) and found that was no significance difference in mass loss associated with decomposition of organic matter between the 3PR and GPC samples, consistent with comparable ligand populations among these two samples **Figure 2.3(a).**

PbS QD films were formed through an air-free, layer-by-layer process. Spin coating of oleate-capped QDs was followed by ligand exchange with an EDT solution **Figure 2.1(a)**. In particular, ~100 nm thick films were formed on Si/SiO_2 substrates. The efficacy of the ligand exchange process was confirmed using Fourier transform infrared (FTIR). The absence of C-H peaks around 3000cm^{-1} indicates that oleate ligand has been replaced by EDT **Figure 2.3(b)**.[84,85]

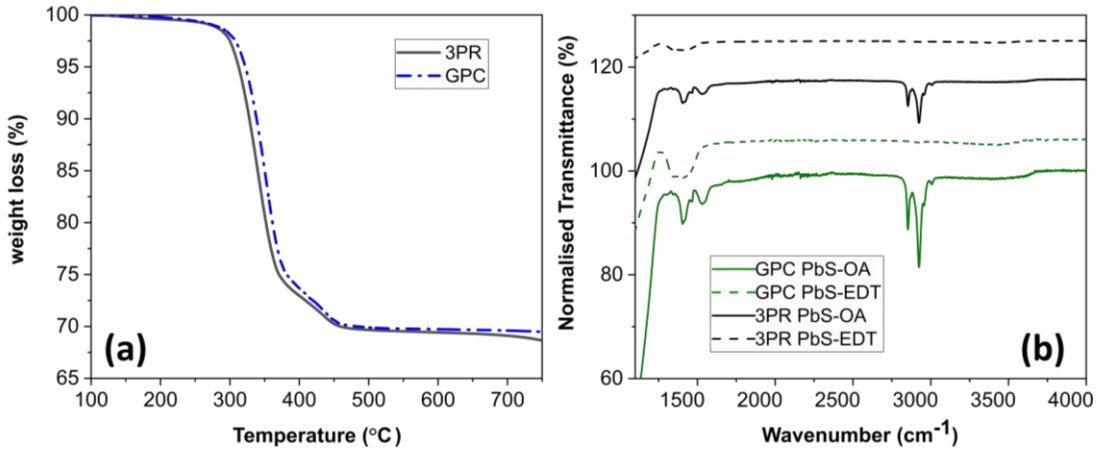

Figure 2.3: *(a) Thermo gravimetric analysis (TGA) graph of dried samples of PbS QDs after 3PR and GPC purifications. (b) FTIR spectra of spin-casted films on SiO_2 before and after EDT ligand exchange*

The film thickness and roughness **Figure 2.4,** were measured by scanning electron microscopy (SEM) and atomic force microscopy (AFM). The overall morphology, as qualitatively seen under SEM imaging **Figure 2.4**, is more uniform for GPC purified QDs, with diminished incidence of micron-scale texture that was most evident in the 3PR sample. Localized surface roughness, measured by AFM, was comparable between 3PR and GPC, but elevated in the 5PR sample, a possible consequence of partial agglomeration. After the layer-by-layer coating and exchange process, the films were dried by annealing in a glove box overnight prior to contact formation. UV-vis-NIR spectra of similar films deposited on glass substrates **Figure 2.3(b),** revealed an additional red shift of the lowest-energy exciton peak in all three films, but with a greater shift for the PR films, as well as a sloping background characteristic of Rayleigh scattering.

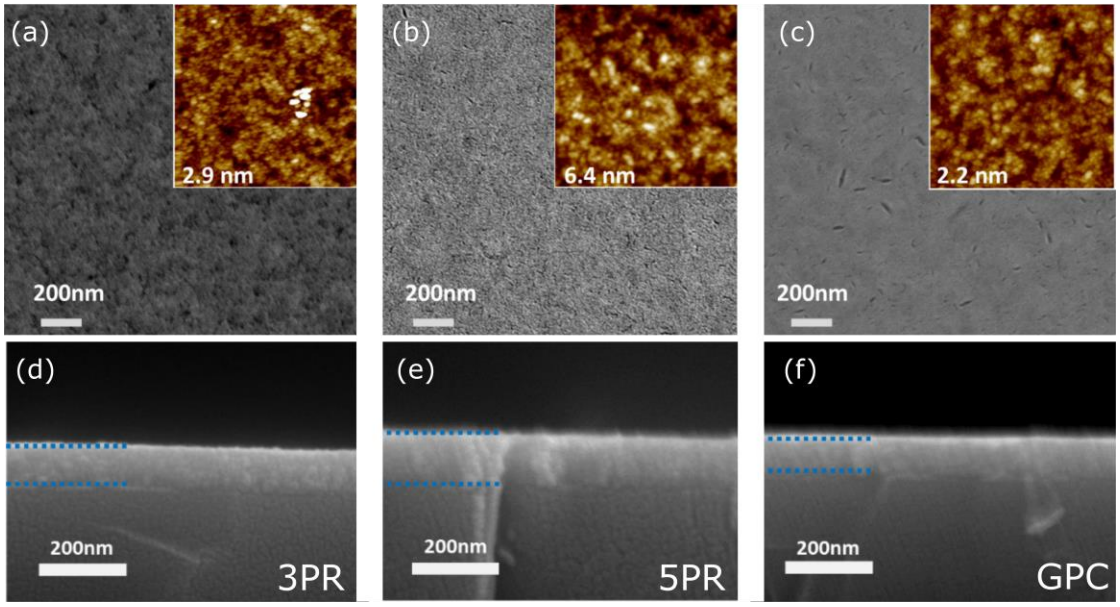

Figure 2.4: *(a,b,c) SEM surface morphology of films made using QDs purified by precipitation/redispersion (3PR, 5PR cycles) and GPC technique insets are AFM images of 2μm×2μm area shows surface profiles indicating the surface roughness (d,e,f) Cross-sectional SEM images of same films made on Si/SiO2-substrates.*

A red shift associated with increased delocalization and dielectric solvation in the presence of neighboring QDs can be anticipated on formation of close packed QD films, but the greater red shift in the PR purified vs. GPC purified films could possibly be associated with ripening or aggregation.[86]

In order to directly characterize and compare the electronic properties of the PbS QD films, metal top contacts (pure Au for ohmic contacts, and pure Al for Schottky contacts as discussed below) of 100 nm thickness were deposited through a shadow mask by electron beam evaporation. This process forms an intimate contact between the QD film and metals with reduced potential for influence of surface relief, oxides, or organic residues that bottom contacts are susceptible to, and similar concerns or mechanical damage that could result from traditional 4-point probe measurements. The evaporated metal films were contacted by fine W wires in a home-built probe station. All measurements were conducted under ambient conditions. As-fabricated devices were tested by current-voltage (*I-V*) measurement in the dark to obtain the resistivity, and under monochromatic illumination to obtain the photocurrent action spectra. The responsivity was calibrated with an InGaAs commercial photodiode with known responsivity.

In first set of measurements, we used a transmission line model (TLM) measurement approach, in which resistance is measured between pairs of neighboring, parallel contact stripes with increasing spacing, to measure separately the bulk film resistivity and the contact resistance[87]. **Figure 2.5(c)**, shows the results for TLM patterns with width *W*=4mm, which is chosen to be at least 10x the maximum contact separation to minimize the influence of spreading resistance.

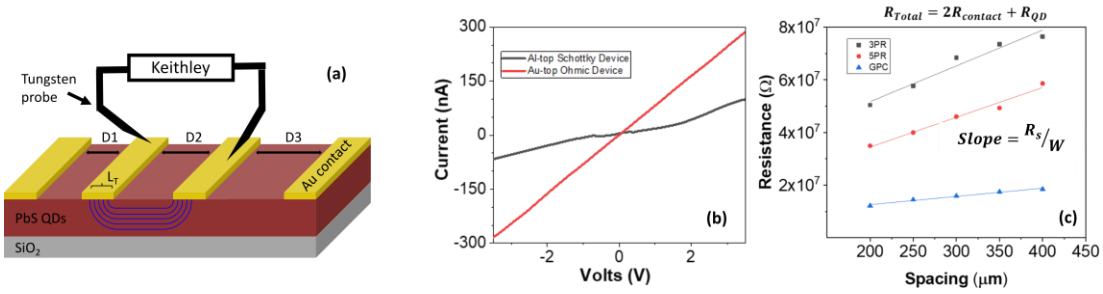

Figure 2.5: *(a) Sketch of TLM devices indicating L_T (b) IVs for ohmic and schottky devices under dark (c) TLM experiment data for sheet resistance and contact resistivity of EDT exchanged films on isolated Si/SiO_2 substrate.*

The slope in these plots is nominally the resistance per unit length, equal to $\boldsymbol{R_s/W}$ where R_s is the sheet resistance of the film, and the *y*-intercept is twice the contact resistance $\boldsymbol{R_C}$. It is easily seen that the GPC film has the lowest sheet resistance, while all samples exhibited low contact resistance consistent with the ohmic ***I-V*** curves seen for Au contacts, as shown for a representative case in **Figure 2.5(b)**. As the film thickness is known, the bulk resistivity for the film can be obtained as:

$$\rho = R_s d_{QD} \quad (1)$$

Here $\boldsymbol{d_{QD}}$ is the film thickness. The product $R_C W$ gives a contact resistivity normalized by the width of the contact. Within the TLM formalism, for a film of uniform thickness, this contact resistivity can be interpreted arising from a specific contact resistance $\boldsymbol{R_{C,sp}}$ for the metal/semiconductor interface. The specific contact resistance and film resistivity determine a characteristic distance over which current is transferred from the film to the top contact. This transfer length $\boldsymbol{L_T}$ can be read from (half) the *x*-intercept of the TLM plot, and from it, the specific contact resistance is obtained as:

$$R_{C,sp} = R_C L_T W \quad (2)$$

The values of $\boldsymbol{\rho}$ for the QD films and $\boldsymbol{R_{C,sp}}$ for the film/Au interface for 3PR, 5PR and GPC samples, as established from measurements in triplicate on similarly prepared films, are listed in **Table 2.1**. We find that the GPC-purified film, despite a larger initial ligand/QD ratio than the 5PR sample, had the lowest resistivity (1.5±0.4 kΩ-cm) and lowest contact resistance. The resistivity is comparable to the lowest values reported for PbS-EDT films prepared at room temperature **Table 2.4**. The contact resistance, while small compared to the total resistance of the film, scales roughly with the resistivity, which has been observed previously in Au-contacted PbS QDs.[75]

In previous reports, EDT has been associated with a tendency to form QD films that have low binding energies for the valence band (band edges shifted to higher energy) and/or exhibit *p*-type conductivity, and Au has been routinely used to form ohmic contacts to EDT-capped PbS QD layers in solar cells[88,44,89]. The large workfunction of Au (ϕ=5.1 eV) can be expected to lead to ohmic contacts to p-type semiconductors, but this is the first direct measurement of specific contact resistance for PbS QD films. We have previously noted ohmic contacts between EDT-capped PbS QD films and epitaxial graphene electrodes with workfunction ~4.5 eV.[67] In contrast, we found that evaporated top contacts composed of Al, a low workfunction metal (ϕ=4.3 eV), gave non-linear *I-V* curves **Figure 2.5(b),** indicative of contact barriers. In the case of the lateral metal-semiconductor-metal TLM structure, the two contacts are biased in opposite directions. However, rectifying behavior characteristic of a single *p*-type Schottky junction is seen when similarly prepared films are contacted with Al in a vertical transport geometry **Figure 2.6c**. We investigated photoconductivity in the PbS QD films to evaluate the effective bandgap, photoconductive gain (*g)*, and in order to evaluate whether the comparatively lower resistivity of the GPC-

purified film arises from increased carrier concentration and/or increased carrier mobility. Figure 4b shows representative photocurrent (I_{ph} vs. V) characteristic for the three films with Au-top contacts under wide-area illumination at 444 nm. Under 2.79 µW total power, the conductivity increases in all 3 films and the photocurrent is approximately linear with power in this regime **Figure 2.6**. The increase in conductivity is largest for the GPC-purified film.

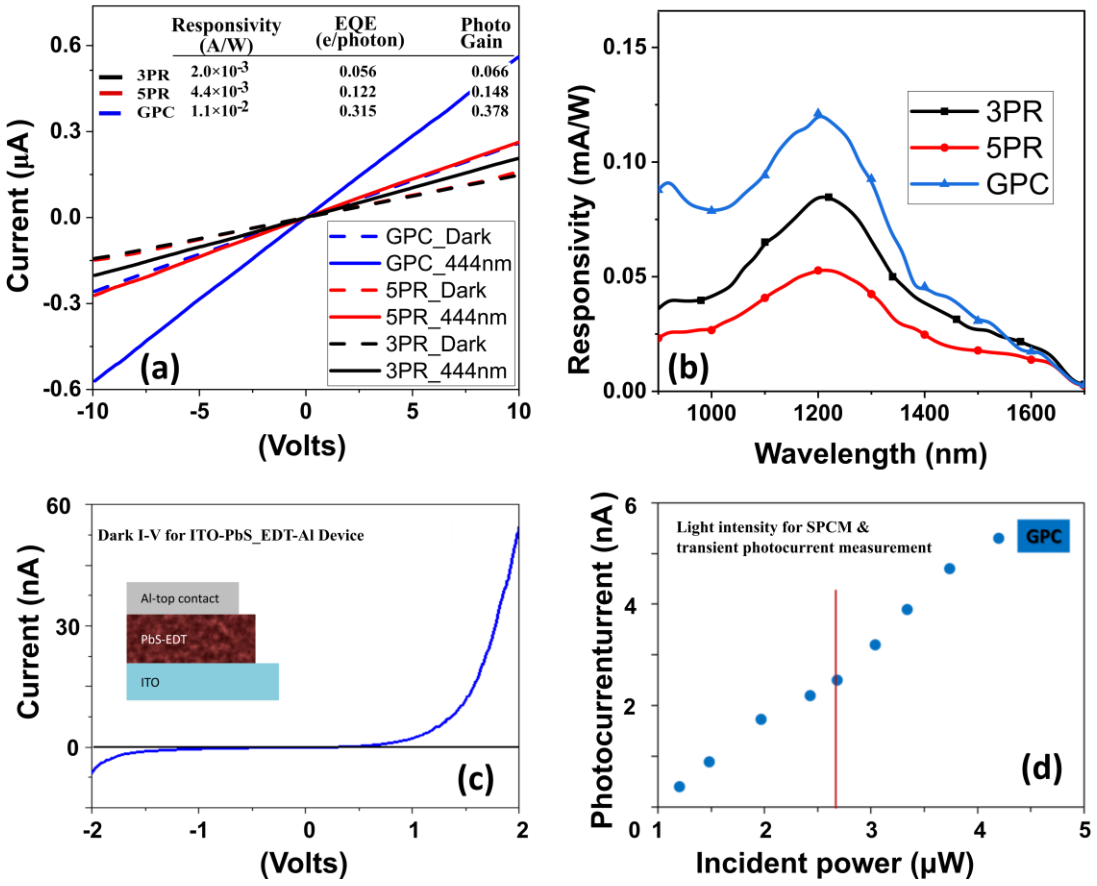

Figure 2.6: *(a) Photocurrent action spectrum of films with ohmic contacts (b) Dark and illuminated current of 75µm×200µm Au-top ohmic photoresistor devices at 2.79 µW 444nm laser illumination (c) Representative I–V curve of a single Schottky junction device prepared by evaporating Al on a GPC-purified PbS-EDT film, formed on a tin-doped indium oxide (ITO)-coated glass substrate serving as an ohmic contact (inset) (d) Intensity dependent photocurrent response of Al-top contacted devices*

The linear increase of photocurrent with applied voltage in each case is a strong indicator of photoconductive gain. In a photoconductive sensor, the gain g (internal quantum efficiency) is determined by how many additional carriers can transit the device within the recombination lifetime.

From the directly-measured responsivity R of such a device under monochromatic illumination, the external quantum efficiency (EQE) and photoconductive gain g can be obtained as

$$\mathrm{EQE} = \frac{R}{q}\frac{hc}{\lambda} = R\,E_{\mathrm{ph}} \quad (4)$$

$$g = \frac{\mathrm{EQE}}{1 - 10^{-A}} \quad (5)$$

where E_{ph} is the photon energy in eV and A is the absorbance of the film at the excitation wavelength, neglecting scattering and reflection. For this purpose, the film absorbance at 444 nm was directly measured using a confocal microscope and a calibrated photodiode detector in order to minimize any losses of transmitted light to small-angle scattering. The responsivity, EQE, and gain at a bias of 1 V for each of the devices studied in Figure 4 are shown in the inset table.

In general, the photoconductive gain can contain contributions from both electrons and holes[40]:

$$g = \frac{V}{L^2}\left(\mu_n + \mu_p\right)\tau_{\mathrm{rec}} = \frac{V}{L^2}\mu\tau_{\mathrm{rec}} \quad (3)$$

where $\boldsymbol{\mu_n}$ and $\boldsymbol{\mu_p}$ are the electron and hole mobility respectively, $\boldsymbol{V}$ is the applied voltage, and $\boldsymbol{L}$ is the length of the device in the direction of transport. On its own, the gain $\boldsymbol{g}$ of a device with known geometry provides an effective mobility-lifetime product $\mu\tau_{\mathrm{rec}}$ for the semiconductor material, where $\boldsymbol{\mu}$ is the effective mobility (representing a sum of electron

and hole mobilities). In practice, one carrier may become rapidly localized in low-mobility traps, in which case $\mu\tau_{rec}$ is determined by the more mobile carrier, which continuing to cycle additional charge through the device until the ground state is recovered through recombination.

We found $\mu\tau_{rec}$ as high as 2.1×10^{-5} cm^2/V for the GPC purified film. We note that this value exceeds mobility-lifetime products reported for holes[71,72,90] and electrons[91] in previous studies of PbS-EDT films , an indication of good quality, but additional information from time-resolved measurements below is needed to determine which carrier dominates the photoconductivity and principally determines the observed $\mu\tau_{rec}$.

The photoresponse action spectrum (responsivity versus wavelength) of the GPC purified films is shown in **Figure 2.4b**. The general shape is identical to the absorbance spectrum in **Figure 2.2**, with the GPC responsivity comparable to the PR films near the band edge. The primary peak is slightly blue shifted for all the films with respect to the absorbance peak, a possible indication of enhanced exciton dissociation when smaller QDs are initially excited. Nonetheless, the action spectrum confirms the photoconductivity is associated with the quantum confined effective bandgap, and illustrates those differences in responsivity for visible (444 nm) light are associated with a diminished response in the PR films at high photon energy, which could be associated with different rates for trapping and recombination upon thermalization of high-energy excited states.

Previously, researchers have measured μ using back-gated *I-V* measurements on field effect transistor (FET) structures fabricated from QD films on SiO_2 dielectrics with conductive Si substrate serving as back gates, from which a field effect mobility is extracted by assuming the FET is biased in the triode region of the FET output

characteristics, with reported μ ~10^{-3} cm^2/Vs for holes in PbS-EDT films. [41,74] However, the field-effect mobility may not accurately describe the behavior of charge-collecting devices due to limitations associated with carrier density, estimation of gate capacitance particularly in films that may experience compensation due to mobile ions or high trap density, and dependence of contact resistance on gate voltage near pinch-off.

To further analyze the optoelectronic properties of the PbS QD films and evaluate the barriers formed at low-workfunction metal contacts, we used scanning photocurrent microscopy (SPCM) to directly image charge collection and identify characteristic lengths.[44,67,75,92] This technique uses a focused, diffraction limited light beam to locally create electron-hole pairs. The excitation spot is rastered over an electronic device to build a map of the resulting photocurrent as a function of illumination position. SPCM was performed using 444 nm laser in a homebuilt setup described previously;[67,93] the laser modulation frequency was 71 Hz and the photocurrent amplitude, along with the reflected light amplitude for spatial registry, were measured with lock-in detection. SPCM measurements were performed on devices formed between top contacts of smaller width than the TLM structures in order to increase the photocurrent relative to dark current under localized excitation.

The **Figure 2.7** illustrates representative SPCM results for Au-contacted and Al-contacted devices, with otherwise identical design characteristics, prepared using the GPC purified QDs. The bias *V* is held close to zero (short circuit) in each case. With Au contacts, the photocurrent signal has constant sign and reaches a maximum value between the contacts. This is consistent with photoconductive behavior in the presence of a small residual bias, in which diffusion of the lower-mobility carrier into the contacts diminishes

the excitation lifetime compared to excitation at the center. Conversely, with Al contacts, the photocurrent displays an opposite sign (equivalently, a 180-degree phase shift) at the opposing contacts. The sign of the photocurrent near each contact indicates that localized excitation causes current flow from the Al contact into the PbS film, consistent with the photocurrent expected for a *p*-type Schottky barrier, reinforcing assignment of the *p*-type character for the PbS-EDT films studied here, consistent with previous reports. The magnitude of the photocurrent decreases slowly with distance away from each contact, falling to near zero in the center.

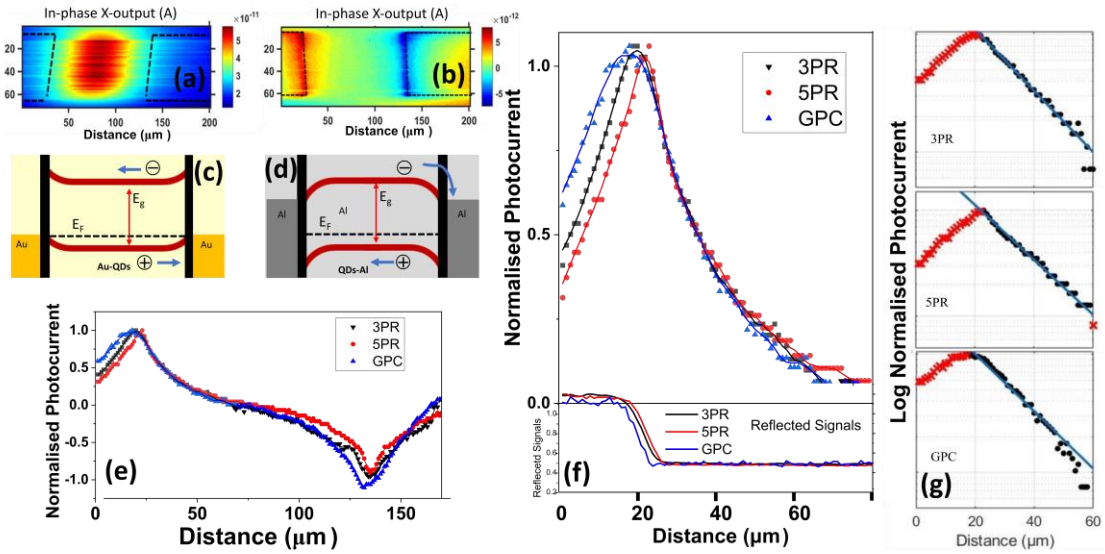

Figure 2.7: *(a,b) SPCM of an ohmic (Au-electrodes) device and Schottky (Al-electrodes) devices (c,d) energy band diagram for ohmic and schottky contacts respective (e) Line scan photocurrent profile for 3PR, 5PR and GPC Schottky devices (f) Line scan photocurrent profile for 3PR, 5PR and GPC Schottky devices to extract diffusion length with reflected signals from same scans (g) Single exponential decay fitting of SPCM photocurrent profiles (logarithmic scale).*

The decay of photocurrent with distance is clearly much broader than the decay of the reflected signal: the reflected signal **Figure 2.7** indicates the point spread function of the excitation laser beam that is convolved with the intrinsic response of the device.

For a *p*-type Schottky contact, the distance over which charge can be collected is the depletion width plus the minority carrier diffusion length L_D. If L_D is long enough, electrons reach the metal electrode, and a photocurrent signal is observed. The photocurrent profiles shown in **Figure 2.7e** can thus be used to obtain L_D in the GPC, 3PR, and 5PR PbS-EDT films. The profiles in each case were well described by an exponential decay, indicating an electron diffusion length $L_D \approx 15$ μm **Figure 2.7f**. Previous SPCM investigations noted L_D larger than the film thickness, for example up to ~1.7 μm for a film of 50 nm thickness. The thicker film and top contact geometry employed here may influence the considerably larger L_D observed here. We performed transient photocurrent measurements in order to characterize the speed of the photoconductive and Schottky devices as sensors, and also to enable estimation of the variation in carrier mobilities. The DC photoconductivity (with ohmic contacts) and SPCM results (with Schottky contacts) offer characteristic lengths for motion of the dominant carrier under drift (as $\mu\tau_{rec} \times V/L$), and for motion of minority carriers under diffusion (L_D) respectively. By combining these with lifetimes, mobility values can be obtained. For the Schottky case:

$$L_D = \sqrt{D\tau_n} = \sqrt{\frac{k_B T}{q}\mu_n \tau_n} \quad (6)$$

$$\mu_n = \frac{q}{k_B T}\frac{L_D^2}{\tau_n} \quad (7)$$

with τ_n the electron lifetime in the conduction band. Figure 6 shows the transient decays for ohmic-contacted (a) and Schottky contacted (b) films. All decays were collected by using a digital oscilloscope to monitor the falling edge of the current signal when the device is excited with a 5 Hz square-wave modulated, wide area laser beam. The data were collected at a constant bias of 3V to ensure a high-enough signal to noise ratio.

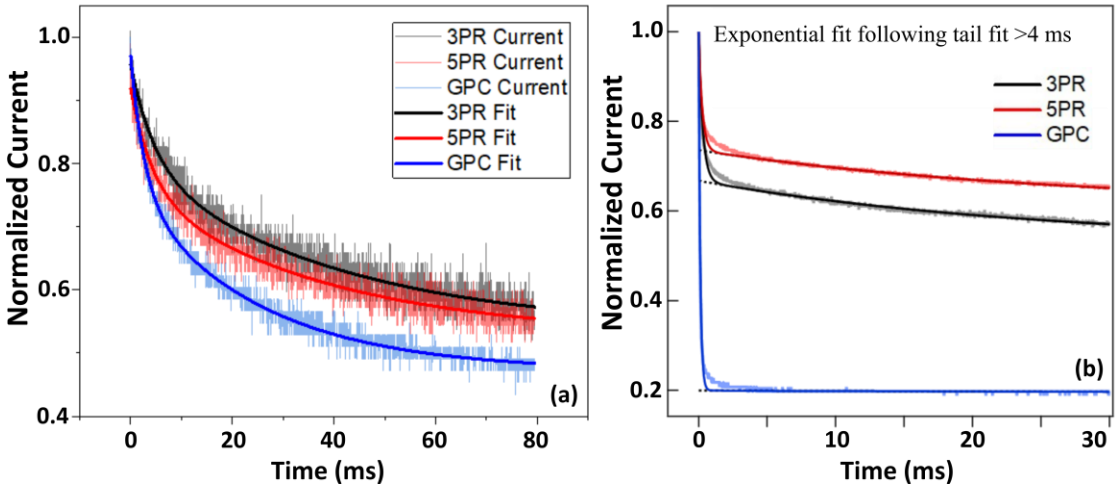

***Figure* 2.8:** *Transient photocurrent decays for (a) Au-contacted (ohmic) and (b) Al-contacted (Schottky) PbS QD films.*

The ohmic-contacted films all showed photocurrent decays over tens of milliseconds with multiexponential line shapes. As shown in **Table 2.1**, the average lifetime for the GPC-purified films (16 ms) was shorter than for 3PR or 5PR, (multiexponential analysis is detailed in Table S1).

For the Schottky contacted devices, the transient photocurrent decay represents the characteristic time required for photoexcited minority carriers (electrons) to recombine or be swept out of the device. As such, the measured lifetime is a lower limit on τ_n and the recombination time τ_{rec}. All devices showed a fast, sub-millisecond decay that was accompanied, in the PR cases, by a longer decay component with a lifetime >20 ms. By separately fitting the slow (>4 ms) and fast (<4 ms) components of the response, it is clear that the slow component is absent in the GPC films. We used tail fitting for transient photocurrent decays to separate out fast and slow components, and used a single-parameter fit of the fast component lifetime to evaluate differences in minority carrier mobility based on Equation 7, since the slow component is effectively filtered out in SPCM. The fast component, which dominates the response at the 71 Hz frequency used for SPCM imaging,

was significantly faster in the GPC film compared to the PR examples as indicated in Table 1. The shorter lifetime in the GPC purified films, together with a comparable diffusion length, is consistent with an electron mobility μ_n that is also higher in the GPC purified films than for PR.

Returning to the behavior of the ohmically-contacted devices, we note that the photocurrent decay in these devices is much slower than the decay time for electrons in the Schottky-contacted devices, suggesting that electrons are significantly trapped on a sub-millisecond timescale, and the photoconductive gain seen with Au contacts is dominated by holes. For a *p*-type film, the low Fermi level position will tend to expose electron traps. If holes dominate the photoconductivity, the observed $\mu\tau_{rec}$ can be used to assign the hole mobility μ_p, which when combined with the observed dark conductivity, provides an estimate of the hole concentration as $p = (q\mu_p\rho)^{-1}$, giving $p \sim 10^{18}$ cm^{-3} for the three films examined here. The 5PR and GPC films had comparable hole concentrations, with the improved performance of the GPC film arising from significantly greater mobility. The 3PR film showed the lowest mobility; its conductivity, being comparable to the 5PR case, is driven by an elevated hole concentration that could possibly arise from greater surface area exposed to air via micron-scale texture seen in SEM. Overall, the hole densities are comparable to 1-2×10^{18} cm^{-3} reported from field-effect measurements on larger (8.8nm) PbS QD films[88] prepared by layer-by-layer ligand exchange with short-chain carboxylates **Table 2.5**.

The mobility values obtained in the ohmic and Schottky contacted cases are not directly comparable head-to-head, as they are obtained under different measurement conditions, but they can be used to compare samples prepared and measured similarly, as

in the case here among 3PR, 5PR and GPC purified films. The photoconductive gain is measured under wide area illumination in ohmic devices, while the diffusion length L_D is measured under focused illumination in rectifying devices, with locally higher power density. Nonetheless, the higher electron mobilities calculated from the Schottky device results may indicate a significant contribution of electrons to the effective mobility observed in ohmically contacted devices.

2.5 CONCLUSIONS

In this study we have utilized variable contact spacing, time-resolved photocurrent, and SPCM to analyze charge transport in films of uniform thickness prepared from purified PbS QDs with known ligand populations. GPC purification let to lower resistivity, lower contact resistance, higher photoconductive gain, and shorter lifetimes than PR purification. An effective mobility-lifetime product an order of magnitude greater than previously studied PbS QD films is obtained using the GPC-purified QD sample.[90] Meanwhile, an electron diffusion length >10 μm was observed via the SPCM profile near a rectifying *p*-type Schottky barrier. Transient photocurrent measurements on the Schottky contacted devices revealed a much shorter lifetime in the GPC-purified case, indicating a higher electron mobility. These results emphasizing a role for detailed control of QD surfaces in improving the response time of QD-based IR photodetectors. While the emphasis of the present study has been on comparing film's electronic properties, identifying the chemical and physical origins of the differences observed will help to improve the performance and durability of SSLE QD solids. Microscale roughness and spectroscopic redshift point to aggregation as a limitation when PR is carried to excess, while larger-scale cracks may introduce additional scattering and elevated carrier densities on air exposure. Among the

purified QD samples, in no case were significant impurity concentrations detected by NMR to impact film properties. The ligand density of the GPC sample fell between those of the PR films examined here, but the presence of long-lived photocurrent decay in Schottky contacts to both PR films, absent in the GPC case, suggests that performance is not simply a matter of optimizing residual ligand density, and that differences in solvent exposure or interparticle contact during purification are possible drivers of variation in electronic properties following SSLE in PbS QD films.

2.6 MATERIALS AND METHODS

The following reagents for synthesis and subsequent purification were used as received. Lead (II) oxide (PbO, 99.9%), anhydrous acetonitrile (ACN, 99.8%), anhydrous toluene (99.8%), and 1,2-ethanedithiol (EDT, 98%) were purchased from Alfa Aesar. Bis(trimethylsilyl) sulfide ($(TMS)_2S$, 95%) and 1-octadecene (ODE, 90%) were purchased from Acros Organics. For purification, methyl acetate (MeOAc, 99 %) purchased from Millipore Sigma was purged with nitrogen for 60 min, and then dried over activated molecular sieves in a nitrogen glovebox. Molecular sieves (4A) were purchased from Mallinckrodt and activated by heating at 200°C under Schlenk line vacuum prior to transfer into the glovebox. Polystyrene Bio-Beads (S-X1, 200-400 mesh), purchased from Bio-Rad, were prepared following Shen et al. (ref. 38 of main text). In particular, beads were washed three times with an excess of toluene and swollen under ambient conditions in toluene for 24 hours. These swollen beads were washed again with fresh toluene and then evacuated to dryness under Schlenk line vacuum before transferring into the glovebox. The beads were swollen a second time with anhydrous toluene inside the glovebox for another 24

hours before loading onto the column (1 cm inner diameter) as described previously, to form a 20cm long stationary phase.

PbS colloidal quantum dots were synthesized following Zhang et al. (ref. 37, main text). The as-synthesized oleate capped PbS QDs have λ_{1s} peak centered at 1250nm, indicating 4.4 nm diameter. After synthesis, the quantum dots were then precipitated and redispersed (PR) under nitrogen atmosphere using anhydrous methyl acetate and toluene, respectively, to form a stock solution designated as 1PR. A portion of QDs from the 1PR stock solution were brought through two further PR cycles, filtered through a 0.1μm PTFE syringe filter, and brought to a final concentration of 25mg/mL in anhydrous toluene (3PR). Similarly, a portion of the 3PR sample was brought through two further PR cycles (5PR). Separately, from the 25mg/mL 1PR stock solution, 250 nmol of PbS QDs were purified using gel permeation chromatography (GPC). The eluted fractions containing QDs were combined and concentrated by removing excess solvent under partial vacuum to achieve a final concentration of 25mg/mL, and then passed through a 0.1 μm filter, to obtain the GPC sample used in subsequent work.

Conductive PbS QD films were formed on Si/SiO_2 substrates (wet oxidized, 200 nm thickness). Chips of ~1 cm^2 were cleaned by sequential sonication in acetone, isopropanol, ethanol, and DI water, and finally dried under N_2 flow. Substrates were heated at 120°C for 10 min to remove adsorbed water before transferring into the glovebox. QD films were deposited using a layer-by-layer deposition and ligand exchange process. Each coating cycle consisted of dropping 20μl PbS solution onto the substrate while spinning at 3000 rpm followed by treatment with 3 drops of 1.0% (v/v) 1,2-ethanedithiol in acetonitrile and rinsing with 3 drops of fresh acetonitrile and 3 drops of anhydrous toluene. Each

deposition, ligand exchange and cleaning step is 30 sec apart and done in nitrogen filled glovebox, using compact spin coater constructed from a hard drive motor and operated by an Arduino microcontroller. This coating cycle was repeated four times to get a ~100 nm thick PbS QD film. Metal top contacts were evaporated through a shadow mask using an e-beam evaporator. The completed devices were then immediately tested for optoelectronic properties under normal atmosphere conditions, using tungsten wire probe arms mounted on a scanning stage.

Table 2.1: *Obtained electronic values for film properties*

Film	Ligand/QD	Resistivity (kΩ-cm)	$R_{C,sp}$ (kΩ-cm²)	Photocurrent lifetime, ohmic (ms)	μ ohmic ($cm^2V^{-1}s^{-1}$)	L_D (μm)	Photocurrent lifetime, rectifying (ms)	μ_n, rectifying[a] ($cm^2V^{-1}s^{-1}$)
3PR	411	3.4 ±0.4	18.0 ±1.6	27	1.4×10^{-4}	15.1	0.296	2.9×10^{-1}
5PR	249	4.8 ±0.0	16.8 ±1.7	24	3.5×10^{-4}	15.3	0.252	3.6×10^{-1}
GPC	348	1.5 ±0.4	5.9 ±4.6	16	1.3×10^{-3}	15.8	0.119	8.1×10^{-1}

Table 2.2. *Photocurrent decay fit parameters (Au contacts).*[a]

Contact Type	Film	τ_{avg}[b] ms	τ_1 ms	A_1[c]	τ_2 ms	A_2[c]	Mobility $cm^2\ V^{-1}\ s^{-1}$
Ohmic	**3PR**	27	4.68 (±0.40)	0.37	40.7 (±3.2)	0.63	1.4×10^{-4}
	5PR	24	4.20 (±0.33)	0.40	37.2 ± (2.3)	0.60	3.5×10^{-4}
	GPC	16	2.27 (±0.11)	0.43	25.2 ± (0.6)	0.57	1.3×10^{-3}

[a]Biexponential least-squares fit: $I(t)=A_1\exp(-t/\tau_1)+A_2\exp(-t/\tau_2)+\text{const}$. [b]Amplitude average lifetime: $\tau_{avg}=(A_1\tau_1+A_2\tau_2)/(A_1+A_2)$. [c]Amplitudes shown are normalized to sum to 1.

Table 2.3. *Photocurrent decay fit parameters (Al contacts).*[a]

Contact Type	Film	τ_{fast}[b] ms	A_{fast}[c,d]	τ_{tail}[c] ms	A_{tail}[c,d]	Mobility $cm^2\ V^{-1}\ s^{-1}$
Schottky	**3PR**	0.296 ± (0.052)	0.71	24.8 (±0.7)	0.29	2.9×10^{-1}
	5PR	0.252 ± (0.029)	0.67	26.8 (±0.7)	0.32	3.6×10^{-1}
	GPC	0.119 ± (0.001)	0.98	118 (±294)	0.02	8.1×10^{-1}

[a]Biexponential tail fit: $I(t)=A_{fast}\exp(-t/\tau_{fast})+A_{tail}\exp(-t/\tau_{tail})+\text{const}$. [b]Least-squares solution of τ_{fast} with other parameters fixed based on behavior at long times (>4 ms). [c]Values determined by monoexponential fit of normalized photocurrent at times > 4 ms. [d]Amplitudes shown are normalized to sum to 1.

Table 2.4. *Representative reported PbS QD film properties*

Material	Resistivity kΩ-cm	$R_{c,sp}$ kΩcm^2	Hole conc. cm^{-3}	L_D (electron) µm	μ (cm^{2}V^{-1}s^{-1})		Group	Ref.
					Hole	Electron		
4.4nm PbS-EDT GPC	1.5	5.9	3.2×10^{18}	15.8 SPCM	1.3×10^{-3}	8.1×10^{-1}	This Work	
4.4nm PbS-EDT 5PR	4.8	16.8	3.3×10^{18}	15.2 SPCM	3.5×10^{-4}	3.6×10^{-1}		
4.4nm PbS-EDT 3PR	3.4	18.0	1.3×10^{19}	15.1 SPCM	1.4×10^{-4}	2.9×10^{-1}		
5nm PbS-EDT	1700		2.0×10^{16}		1.0×10^{-4} FET		Klem *Appl. Phys. Lett.* 2008 (Sargent)	28
6nm PbS-butylamine			3.0×10^{16}		2×10^{-4} CELIV	2×10^{-4} drift	Johnston *Appl. Phys. Lett.* 2008 (Sargent)	29
8.8nm PbS-formic acid	1.3		2.0×10^{18}		2.4×10^{-3} FET		Zarghami *ACS Nano* 2010 (Law)	47
4.4nm PbS-butylamine				1.8 SPCM			Strasfeld *Nano Lett.* 2012 (Bawendi)	36
6.3nm PbSe-Na_2S				1.7 SPCM			Otto *Nano Lett.* 2013 (Dong)	35
3.6nm PbS-EDT			3.6×10^{15}		3.1×10^{-5} SCLC		Kwan Kim *J. Appl. Phys.* 2014 (Jeong)	31
5nm PbS-EDT					3.1×10^{-4} FET		Kim, *Chem. Mat.* 2014 (Park)	33
3nm PbS-EDT					1.0×10^{-4} FET		Cao *Nat. Energy* 2016 (Konstantatos)	32
3nm PbS-EDT, annealed					1.0×10^{-2} FET			
4.5nm PbS-EDT	18.0						Kelley *ACS Appl. Elec. Mat.* 2020 (Greytak)	24

CHAPTER 3

A p-TYPE PbS QUANTUM DOT INK WITH IMPROVED STABILITY FOR SOLUTION PROCESSABLE OPTOELECTRONICS*

3.1 INTRODUCTION

Colloidal quantum dots are promising absorber materials for applications in optoelectronics and photovoltaic devices due to their tunable absorbance stemming from a size-dependent optical band gap that can be fine-tuned for solar energy capture. More importantly, these materials are compatible with low-temperature thin film solar concentrators, flexible and printable solar cells, and photodetectors manufacturable at industrial scales and at a low cost as compared to their crystalline-based counter parts[50,94,95]. To get the most power out of a solar cell device, tandem solar cells based on quantum dots is another approach that raises the possibility of increasing power conversion efficiency beyond the single junction limit[96].

In recent years, the efficiency of QD-based photovoltaic devices has improved significantly, with improvements in new device architectures, such as the quantum heterojunction devices, and the realization of improved ligand exchange and fabrication

* Reprinted with permission from Ahmed, F., Dunlap, J. H., Pellechia, P. J., & Greytak, A. B. (2021). A p-type PbS quantum dot ink with improved stability for solution processable optoelectronics. Chemical Communications, 57(65), 8091-8094 DOI: 10.1039/D1CC03014K

processes, including the introduction of n-type and p-type QD inks.[97,98] Record-setting QDs photovoltaic devices reported so far are fabricated using solid-state ligand exchange to replace long greasy aliphatic ligands used in the synthetic step.[99] The solid-state film fabrication and ligand exchange (SSLE) technique is highly inefficient with dual drawbacks: it leads to waste of material as only about 1% of synthesized quantum dots end up being incorporated into the actual device, and is incompatible for large area application.[7,33] Additionally, the volume change associated with SSLE yields rough and cracked films following exchange treatments, and requires successive layers to fill the cracks and obtain smooth and continuous films. For these reasons, much attention has been given to solution-based ligand exchanged processes to formulate quantum dot inks that can be directly incorporated into devices through more conservative spray or roll-to-roll printing techniques for large area deposition for mass scale photovoltaic applications.

There are many reports in literature for solution-based halide ligand exchanged quantum dot inks forming *n*-type colloidal suspensions, but only a handful of publications focus on *p*-type quantum dot inks.[54,99–101] In SSLE work with PbS QDs, ethanedithiol (EDT) has been a benchmark ligand treatment for the formation of *p*-type films. Besides EDT, 3-mercaptopropionic acid (MPA) is the most explored and suitable organic ligand for PbS QDs to yield high-efficiency quantum dot solar cells through SSLE, as it can achieve a similar interparticle distance to EDT and maintains the thiol functional group.[102–104] MPA has also been a focus for development of PbS QD inks based on the hope that the carboxylic acid group can confer solubility in polar liquids through hydrogen bonding interactions and/or charge stabilization, but it has been challenging to find optimum solvent conditions for stabilizing such inks. For example, MPA-capped quantum dots have been

dispersed in DMF or DMSO, but these solvents also interact with the PbS surface and MPA tends to form crystals in these solvents undermining their stability and subsequent device performance.[96,105] Recently, butylamine has been investigated as a solvent component for p-type inks, including butylamine-stabilized water-soluble MPA-capped QDs,[98] and hybrid inorganic/organic passivated PbS QDs in which the surface is initially treated with halides prior to thiolate ligand exchange.[99,106] Notably, this approach, combined with a SSLE-deposited PbS-EDT and hole transport layer, led to record performance for colloidal QD solar cells. Yet, butylamine can also etch QD surfaces, causing precipitation and loss of quantum confinement within hours[107], presenting concerns for manufacturing QD devices on a large scale and in a reproducible manner.[108] It is important to explore ligand and solvent chemistry for QD inks that can improve processability and device performance, also, to establish the nature and extent of ligand exchange that is occurring when such inks are prepared.

3.2 LIGAND EXCHANGE PROCESS

Here, we report highly stable MPA-capped PbS QDs dispersed in benzylamine (BnzAm) through a rapid biphasic exchange technique using methanol (MeOH) as the ligand exchange solvent. We postulated that small, polar mercaptans can be paired with a suitably matched weakly-coordinating organic solvent. BnzAm is a less polar organic solvent that is also compatible with the rest of the device architecture. In addition, MeOH has the dual advantages of weaker interaction with the QD surface compared to DMF and a boiling point low enough compared to BnzAm that it can be effectively removed from the QD-MPA/BnzAm mixture under partial vacuum.

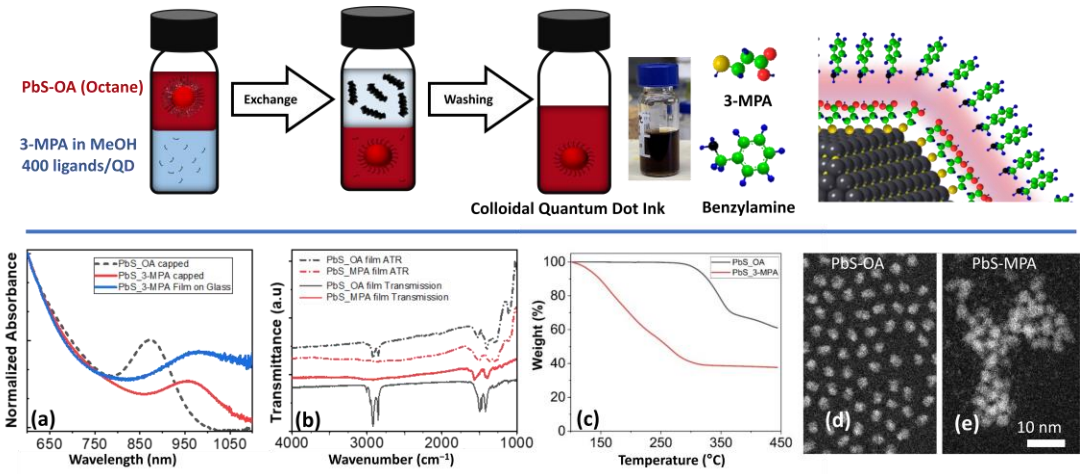

***Figure* 3.1:** *(Top) biphasic ligand exchange process. (a) UV-Vis absorption spectra of pre- and post-ligand exchanged PbS QDs and PbS-MPA film on glass, normalized at 600 nm. Llight scattering and dispersion contribute to the baseline absorption of the film. (b) FTIR absorption and attenuated total reflection spectra of films (c) thermogravimetric weight lose traces of PbS-OA and PbS-MPA QDs solids (e) STEM images of oleic acid and MPA capped PbS QDs*

We have performed comprehensive quantitative and qualitative analysis on the MPA-capped PbS quantum dot ink, and on photoconductive and photovoltaic test devices made using it. These devices are formed at ambient temperature using spin-coating technique. The ink-based approach is highly suitable for making p-n junction and standalone heterojunction solar cell devices using a variety of methods including simple doctor blading, and should be extensible to spray or roll to roll printing processes.

Ligand exchange and film deposition steps were conducted in a N_2-filled glovebox. A solution of MPA in MeOH was stirred with an oleate-capped PbS QD stock solution (880 nm peak absorbance, ~2.8 nm diameter, **Figure 3.1**). After washing with *n*-octane to remove exchanged oleates from the system, the MPA-capped PbS QDs were precipitated from MeOH and BnzAm was added, forming a well-dispersed solution. In a control experiment, addition of butylamine failed to produce a stable colloidal solution, in

agreement with previous observations[99] **Figure. 3.2**. Ultraviolet-visible-NIR absorbance spectra of the oleate-capped QDs in octane and of the ligand-exchanged PbS-MPA QD solution are shown in **Figure 3.1a**. Both spectra show a distinct lowest-energy electronic excitation (exciton) peak indictive of quantum confinement and narrow size distribution.

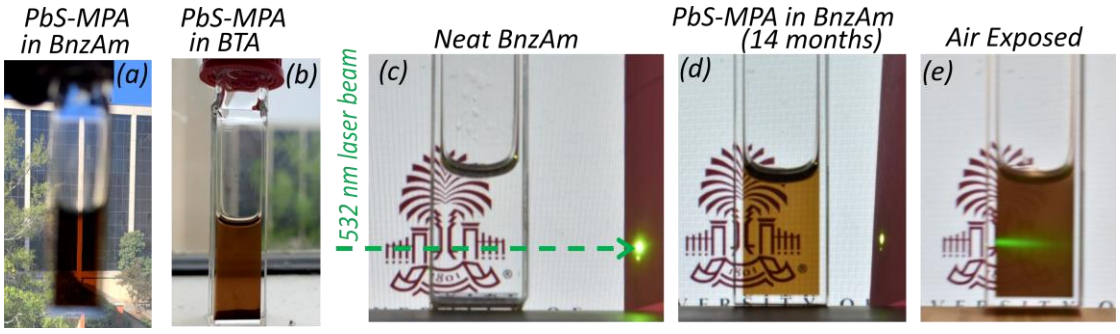

Figure 3.2: *(a) Well-dispersed solution of PbS-MPA QDs in Benzylamine (b) PbS-MPA in butylamine failed to produce a stable and well-dispersed colloidal solution. (d) PbS-MPA in BnzAm remains well dispersed with negligible light scattering after 14 months. photo shows ink diluted in additional dry BnzAm after storage at room temperature under ambient light, in an inert atmosphere. (e) QD aggregation due to air exposure leads to a hazy appearance within a few hours.*

3.3 RESULTS AND DISCUSSION

The presence of a well-defined absorbance peak indicates retention of narrow, quantum-confined size distribution, but a redshift is observed that we attribute primarily to the extension of electron-hole pair's wavefunctions into the capping ligands.[109] The absorption spectrum of the QDs in the BnzAm scales linearly with concentration, and the QDs remained stable for weeks or more with no prominent change in spectrum and no significant light scattering, as illustrated in **Figure 3.2(a,b)**. The exciton peak position is similar in films deposited from the ink.

Infrared spectroscopy performed in attenuated total internal reflectance (ATR) and transmission modes showed that the C-H stretching peaks of oleate ligand around 3000cm^{-1} are absent in films deposited from the MPA-capped ink, indicating a complete ligand exchange **Figure 3.1b.**

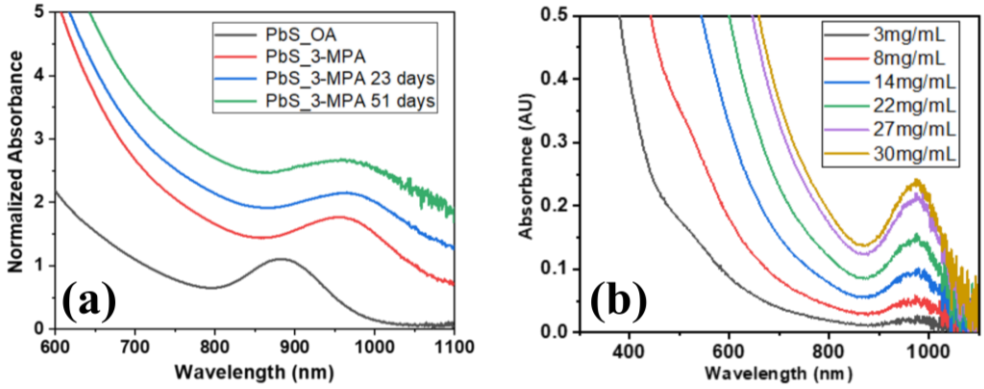

Figure 3.3: *(a) UV-Vis Absorbance of QDs as-synthesized (diluted in n-octane) and post ligand exchange (diluted in BnzAm) over the period of 51 days (normalized at lowest-energy peak minus background; PbS-MPA spectra are vertically offset for clarity). (b) UV-Vis Absorbance of MPA capped QDs for series of dilutions in benzylamine solvent.*

Ligand exchange was further investigated by thermogravimetric (TGA) analysis under inert (N_2) atmosphere. **Figure 3.1c** presents the TGA from PbS-OA and PbS-MPA. The loss of ~30% of initial mass around 360°C is characteristic of OA-molecules attached to QD surface through carbonyl attachment[27]. In contrast, MPA gradually leaves the dried ink sample giving continuous mass loss until 250°C. This long TGA slope is attributed to the presence of strongly- and weakly-bound MPA in the sample, as it is also evident from NMR experiments.

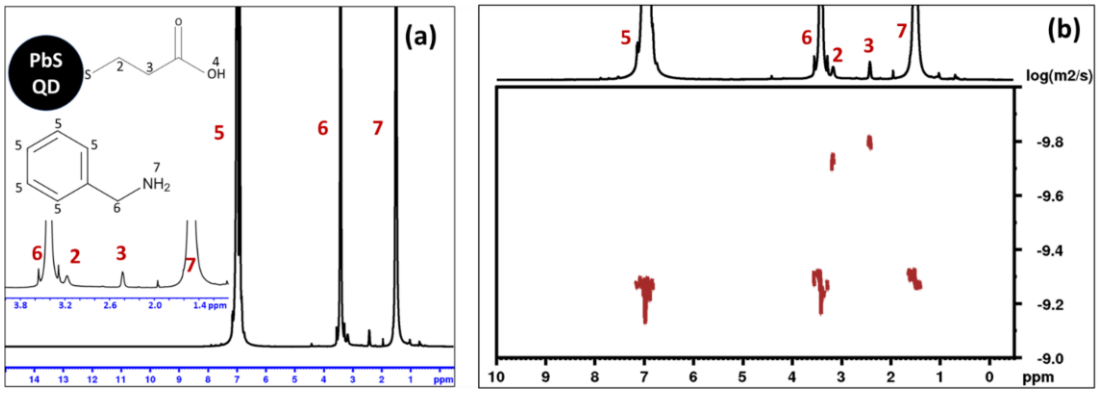

Figure 3.4: *(a) ^{1}H NMR spectrum of PbS-MPA in benzylamine. Inset: magnified scale revealing MPA methylene resonances. (b) Corresponding DOSY plot indicating slow effective diffusion constant for MPA interacting with the QD surface.*

Scanning transmission electron microscopy (STEM) images displayed in **Figure 3.1(d,e)** revealed a significant decrease in the distance between neighboring MPA-capped particles deposited from the BnzAm ink compared to those with oleate capping, consistent with a ligand shell of smaller thickness, while the QDs retain a similar size distribution.

The ligand exchange process was further characterized by 1D ^{1}H NMR, and by diffusion ordered ^{1}H NMR spectroscopy (DOSY). Since a deuterated form of the benzylamine solvent was not easily available for this study, we performed NMR analysis in the natural abundance (proteo) solvent. In the 1D spectra in **Figure 3.4a**, no bound or free OA could be detected in the final ink solution and expanded QD-MPA spectra and reference oleic acid spectra are given in, **Figure.3.8 & 3.7**. The alkyl proton peaks of MPA in the QD-MPA sample are significantly broadened and shifted from those observed when MPA is added to clean BnzAm solvent in the absence of QDs **Figure.3.7**.

These shifts help in establishing the binding mode of MPA ligand. The broad signals at 2.42 and 3.17 ppm suggest that the MPA constitutes a single population that is strongly interacting with the QD surface on the NMR timescale. To further evaluate the

extent of binding, we used a DOSY experiment with gradient pulse δ = 4 ms and diffusion period Δ = 25 ms. The MPA peaks in the QD sample indicate significantly slower diffusion compared to the benzylamine solvent, and compared to the value for the MPA in benzylamine on its own, while the solvent peaks are unchanged **Figure.3.9-3.11**. The hydrodynamic radius of methanol was estimated to be 0.215 nm using the Stokes equation based on a standard DOSY experiment in D_2O. Effective hydrodynamic radii of other species were calculated based on the following equation:

$$\frac{D_s}{D_{ref}} = \frac{R_{ref}}{R_s} \qquad \text{E}q.3.1$$

Where: D_S, D_{ref} are measured diffusion coefficients and R_{ref} and R_s are hydrodynamic radius of sample and reference respectively. We used the effective diffusion constant of MPA in methanol to calculate hydrodynamic size of free MPA molecules Rs=0.34 nm. from **Figure 3.9**, and was likewise used to assign the effective *R*s for MPA in the PbS-MPA ink by comparison of diffusion coefficient (***D)*** for the MPA methylene resonances for free MPA and PbS-MPA in benzylamine solvent as listed in **Table 3.1**.

Table 3.1. Diffusion constants of different samples measured by DOSY

System	D_{BnzAm} 10^{-10} m^2/s	D_{MPA} 10^{-10} m^2/s	$R_{S,MPA}$ nm
MPA in BnzAm solvent	5.5	2.25	0.34
PbS-MPA in BnzAm solvent	5.4	1.25	0.61

The ratio of MPA diffusion constants, through the Stokes-Einstein relationship, gives an effective hydrodynamic diameter of 1.2 nm for MPA in the PbS-MPA ink. This is less than expected for the QD diameter (2.8 nm, from sizing curve), indicating that the

MPA ligand is in dynamic equilibrium between bound and free forms under the conditions studied.

In order to evaluate the film deposition conditions and basic electronic properties of PbS QD solids cast from the PbS-MPA ink, we formed two-terminal lateral transport devices on Si/SiO_2 substrates with pre-patterned Ti/Au (15 nm/25 nm thickness) bottom contacts defined by photolithography and formed by electron beam evaporation. A low-speed spin coating method was used to fabricate thin films for devices to characterize the material for electronic properties (see materials and method section for details). The PbS-MPA film morphology was analyzed using scanning electron microscopy (SEM) **Figure 3.5b** and atomic force microscopy (AFM) **Figure 3.5a**. The surface roughness and film thickness were measured through AFM. The films showed a very smooth surface with uniform film **Figure 3.5c** with a rms surface roughness of 0.5 nm that is superior to SSLE films reported so far.[110,111] Such a smooth film morphology reduces the possibility of current leakage in stacked vertical devices.[112] The intrinsic dark resistivity of the deposited PbS-MPA film was evaluated via the transfer length method (TLM), in which the resistance is measured between pairs of parallel electrodes with increasing distance between them. The method yields the sheet resistance from the slope of this line and, when multiplied by the measured film thickness, the bulk resistivity. For the device examined in **Figure 3.5e**, with a film thickness of 170 nm, we calculated a bulk resistivity of 1.45±0.03 kΩ-cm. This is significantly lower than previous reported values for state-of-the-art EDT-capped SSLE films reported in literature.[43,113] Two terminal lateral devices with smaller active area as shown in **Figure 3.5d** were used for lateral photoconductivity measurements.

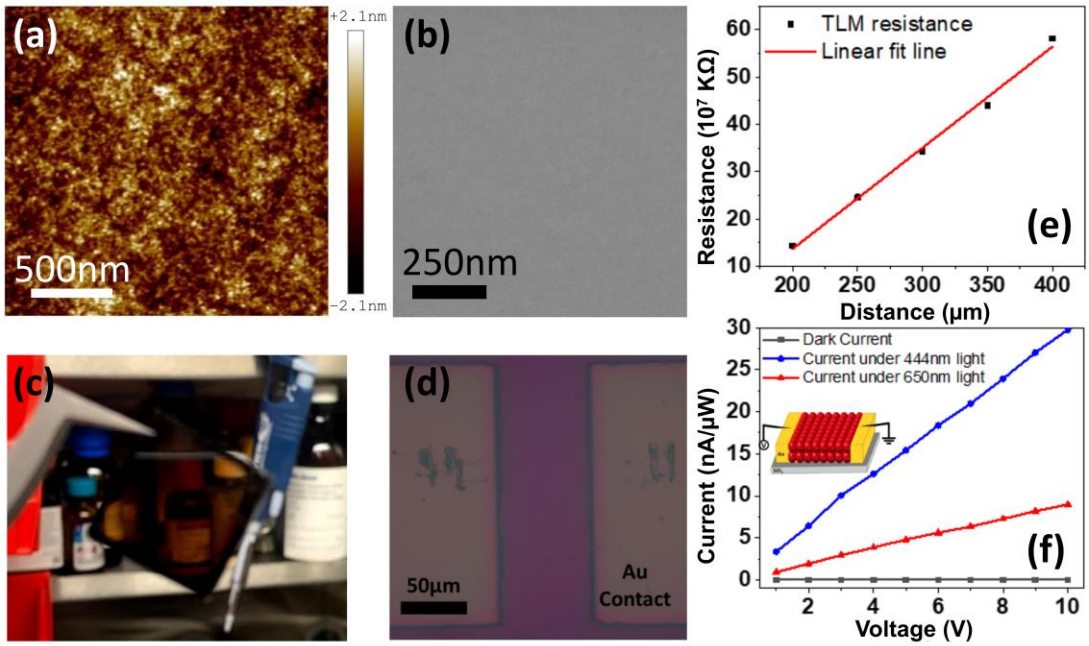

Figure 3.5: *atomic force microscopy (AFM) (b) Scanning electron microscopy (SEM) images of surface morphologies of PbS-MPA film (c,d) optical image of film on glass and Si/SiO2 substrate ((e) TLM measurement graph (f) dark and photocurrent under 560nm and 444nm laser light.*

The devices showed a linear current-voltage (I-V) relationship consistent with ohmic contact to the Au-electrodes as expected based on the TLM results. A significant increase in conductivity was observed when the devices were illuminated with visible or NIR light. Laser illumination at 444nm and 650nm were used to determine responsivities of 3.9mA/W and 3.7mA/W respectively, for a 200 µm×75 µm active area device at 10 V applied bias **Figure 3.5f**

We formed heterojunction photovoltaic devices with a TiO2 n-type component **Figure 3.5.** The devices were kept in a N_2-filled glove box overnight at ambient temperature for aging to remove any residual solvent trapped in QDs film before evaporating metal top contacts through a shadow mask. We used pure Au top contacts to define devices with active areas of $2mm^2$ and $8mm^2$. A total of 12 similar devices were

measured on four different substrates made at same time with similar deposition conditions. These devices were tested for power generation under AM 1.5G 100mW/cm^2 using a home built solar simulator which was calibrated using a standardized Newport photodetector for light intensity Current density-voltage (J-V). characteristics were recorded using Keithley 2636A source meter. The standout device had an efficiency of 5.53% with a fill factor of 50%.

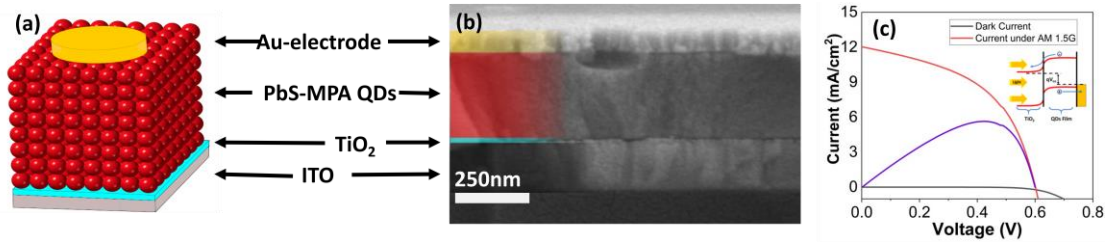

Figure 3.6: *(a) Heterojunction solar cell device architecture (b) cross-sectional SEM image of solar cell device (c) performance of the QD solar cell measured under AM 1.5G. The purple curve indicates the power on an arbitrary scale.*

We emphasize that this result was achieved without any SSLE QD deposition steps, whereas some previous work on QD inks has employed a SSLE-deposited PbS/EDT layer as a hole transport layer. We achieved an even larger open circuit voltage of 720 mV with an additional poly-TPD electron blocking/hole transport layer between the PbS QDs and the Au contact, but this caused the device efficiency to fall below 2%. While the efficiency stands the be improved with further optimization of device design, this open circuit voltage was on par to some of the highest reported V_{OC} for similar size quantum dots.

3.3 CONCLUSION

In summary we have synthesized a *p*-type PbS quantum dot ink using BnzAm as an organic ink solvent which is stable for several weeks under inert atmosphere. Benzylamine showed significantly greater solubility and stability of MPA-capped PbS

QDs than did butylamine under identical conditions. We have demonstrated the applicability of this material in the fabrication of a heterojunction quantum dot solar cell with an efficiency over 5% under AM 1.5G radiation. Semiconductor inks are compatible with spin coating, spray coating and drop casting methods to make thick films for optoelectronic devices, especially solar cells. We note that the use of a low-boiling exchange solvent and higher-boiling ink carrier enables greater flexibility in formulation of the QD ink. For example, we have noticed that complete drying of the MPA-capped PbS QDs under vacuum, as might be required to remove a higher-boiling exchange solvent, can lead to difficulty in subsequent re-dispersion of the QDs. With MeOH as the exchange solvent, only gentle drying following exchange is necessary, and residual MeOH can be removed from the BnzAm solution under partial vacuum if desired. The character of the organic benzylamine solvent employed here raises the possibility of forming *p*-*n* junction type solar cells and detectors by incorporating solution-based *n*-type inks as well, and using printing or spray coating techniques to apply such materials to heat-sensitive flexible substrates.

3.4 MATERIALS AND METHODS

The following reagents for synthesis and subsequent ligand exchange were used as received. Lead (II) oxide (PbO, 99.9%), anhydrous toluene (99.8%), and 1,2-ethanedithhiol (EDT, 98%) were purchased from Alfa Aesar. Bis(trimethylsilyl) sulfide ($(TMS)_2S$, 95%) and 1-octadecene (ODE, 90%) were purchased from Acros Organics. For PR (Precipitation/re-dispersion) purification, methyl acetate (MeOAc, 99 %) purchased from Millipore Sigma was purged with nitrogen for 60 minutes and dried over activated 4A molecular sieves in a nitrogen glovebox.

PbS colloidal quantum dots synthesis: PbS QD were synthesized according to the previously reported method by Zhang et al.[114] with slight modifications. In particular, after synthesis, precipitated and re-dispersion (PR) were carried out under nitrogen atmosphere using anhydrous methyl acetate and *n*-octane respectively. The process was repeated twice to remove impurities and synthesis solvent. As-synthesized oleate capped PbS QDs have lowest energy electronic transition (λ_{1s}) peak centered at 880 nm (1.4 eV), indicating 2.8 nm diameter as estimated through a previously published sizing curve.[115]

Biphasic Ligand Exchange Process: In the bi-phasic ligand exchange process, 2 mL of 50 mg/mL of purified, oleate-capped PbS QDs in *n*-octane was added drop wise to 2 mL MeOH containing 0.205 g 3-MPA (~400x ligand/QD) while stirring at room temperature. The ligand exchange process completed within few seconds and quantum dots were transferred from octane into MeOH forming a dark brown polar phase. Octane supernatant was removed, 5 mL of fresh octane was added to wash PbS-MPA capped quantum dots, and the washing step was repeated three times to remove exchanged oleate/oleic acid ligands. After the final wash and separation of non-polar phase, 2 mL of toluene was added to the MeOH solution to promote flocculation of the 3-MPA capped QDs (we note that flocculation of the 3-MPA capped QDs in MeOH solution occurs slowly even in the absence of toluene). The mixture was centrifuged at 4000 rpm for 10 min to pull down the QDs, and the supernatant was decanted away. The QDs were then dried under flowing nitrogen, and 2 mL of BnzAm was added (or, in a control experiment, 2 mL butylamine). After stirring the PbS-MPA and BnzAm mixture, QDs were centrifuged at 10000 rpm for five minutes to get rid of any undissolved particulates and filtered through 0.1 µm PTFE

filter before spin coating on devices. Typically, the QD/BnzAm ink was obtained with a final concentration of ~40 mg/mL.

NMR spectroscopy: ^{1}H NMR of the PbS-MPA in benzylamine and all DOSY measurements were performed on a Bruker Avance III-HD 500 MHz spectrometer. Reference spectra to aid in peak assignment were recorded on a Bruker Avance III-HD 400 MHz spectrometer. Measurements of the ink were conducted directly on the sample at ~40 mg/mL PbS QDs in normal-abundance (proteo) benzylamine, and employed 16 acquisitions with 30s delay. Measurements for MPA/benzylamine mixtures were conducted similarly and chemical shift was referenced to a tetramethylsilane (TMS) external standard. Reference spectra for MPA and benzylamine in methanol were recorded in methanol-d_4 and referenced to the methanol residual CH_3 peak and a TMS internal standard respectively. Full scale ^{1}H NMR spectra. And peak assignments for MPA in methanol-d4 were made as follows: multiplets at δ = 2.65 ppm and δ = 2.74 ppm correspond to the methylene protons nearest to and farthest from the thiol group, respectively. These assignments are also consistent with findings by Reinhart et al. for MPA in DMSO-d6. Peak assignments for benzylamine in methanol-d4, in which NH2 exchanges with the solvent. (c,d) Spectra for 3% MPA and a higher concentration (~10%) respectively in proteo-benzylamine. We note that in the MPA methylene peak positions are nearly identical to those in methanol-d4, and we make the same assignment. In ^{1}H NMR spectrum of the ink the free MPA peaks are absent, and broadened resonances are found at δ = 2.42 ppm and δ = 3.17 ppm. We assign the peak at δ = 3.17 ppm to the methylene protons nearest the thiol on the basis of its greater shift and broadening (as expected for ligands bound to QD surfaces).

Figure 3.7 contains full scale ^{1}H NMR spectra. of (a) MPA in methanol-d4 (b) benzylamine in methanol-d4, in which NH_2 exchanges with the solvent. (c,d) Spectra for 3% MPA and a higher concentration (~10%) respectively in proteo-benzylamine. We note that in the MPA methylene peak positions are nearly identical to those in methanol-d4, and we make the same assignment. (e) ^{1}H NMR spectrum of the ink.

Device Fabrication: ITO coated glass substrates with area ~2 cm^2 were cleaned by washing with detergent and then sequentially sonicated in acetone, IPA, ethanol, and dionized water for 5 minutes each before drying by nitrogen flow. Three drops of 5% tetrabutyl *titanate* solution in dry ethanol were spin coated at 4000 rpm. These coated substrates were annealed at 450°C for 30 minutes to form compact TiO_2 films and were used for photovoltaic device fabrication without further treatment. 15 μL of PbS-MPA solution was dropped and spread on entire substrate by spinning at 1500 rpm for 30 s, followed by annealing at 90° and left in glove box to dry. The process was repeated to make a ~200 nm thick film. Each layer was annealed at 90°C for five minutes before subsequent coating. The top Au-contacts were deposited using MDC e-Vap 4000 Electron Beam Evaporation System with a base pressure 1×10^{-6} torr through a shadow mask. The shadow mask also defines the active area of the devices. Au metal was deposited at a rate of 2Å/s to get a final metal thickness of 100nm. Similarly, conductive PbS QD films were fabricated onto a prepatterned SiO_2-coated silicon substrates by spinning 15 uL QD solution yielding a 170nm think film for lateral devices to measure sheet resistance and photoconductivity. While spin coating and annealing were conducted under nitrogen, all electronic measurements were done at room temperature and under ambient atmosphere.

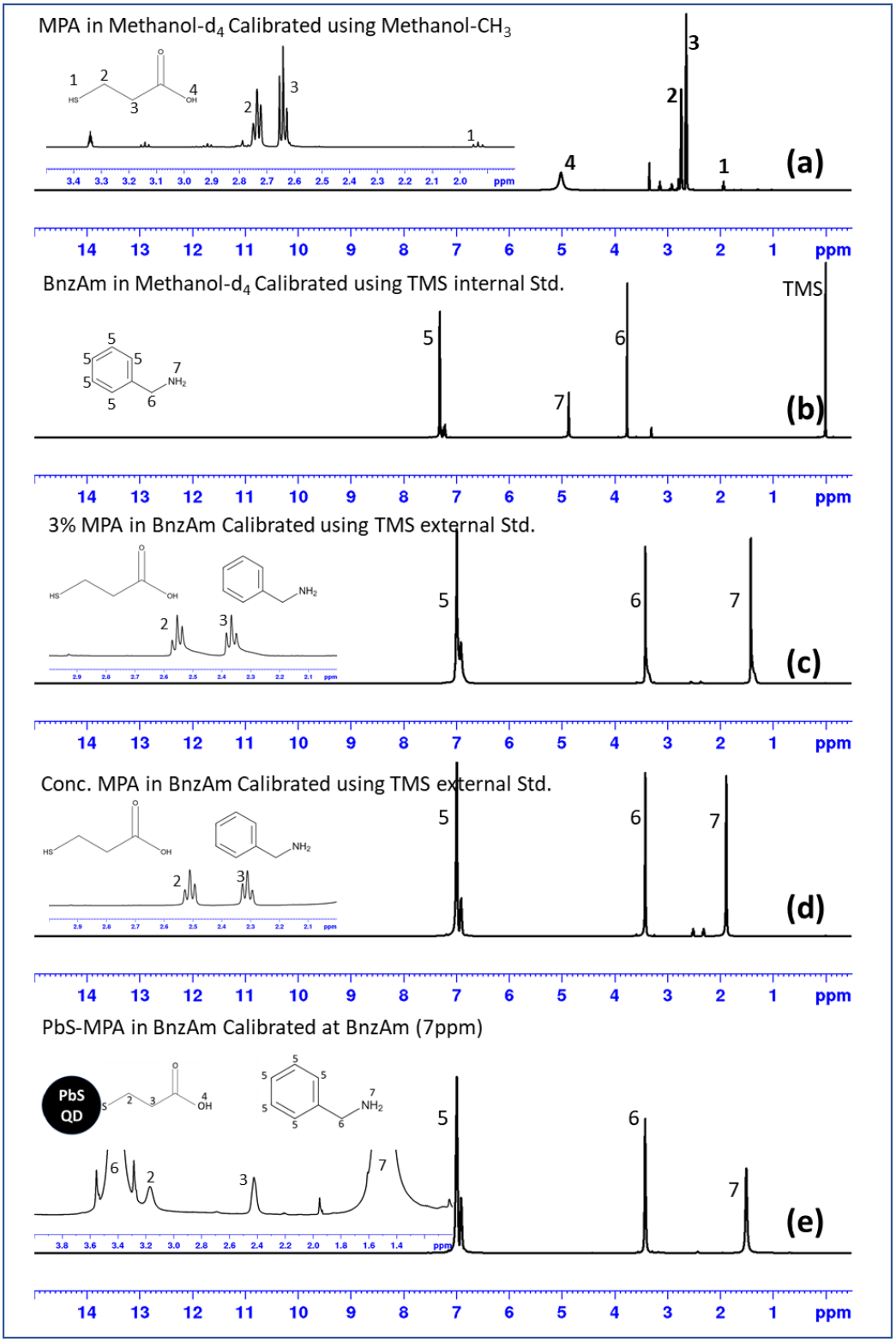

Figure 3.7: *Full scale ^{1}H NMR spectra.*

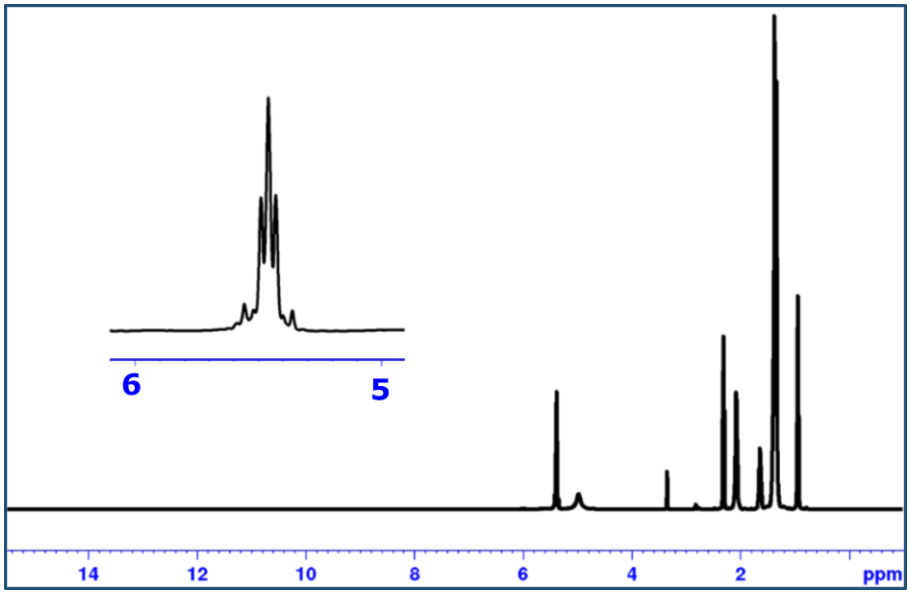

Figure 3.8: *Full scale ^{1}H NMR spectra of Oleate ligand in Toluene d_8.*

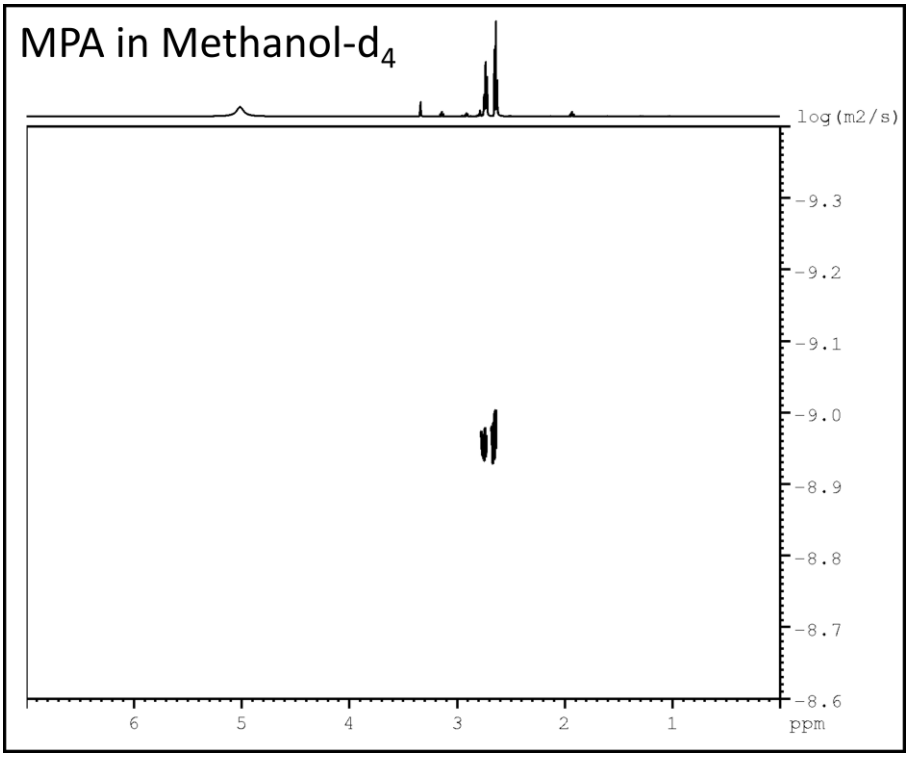

Figure 3.9: *Full scale ^{1}H DOSY NMR spectra of MPA in MeOD.*

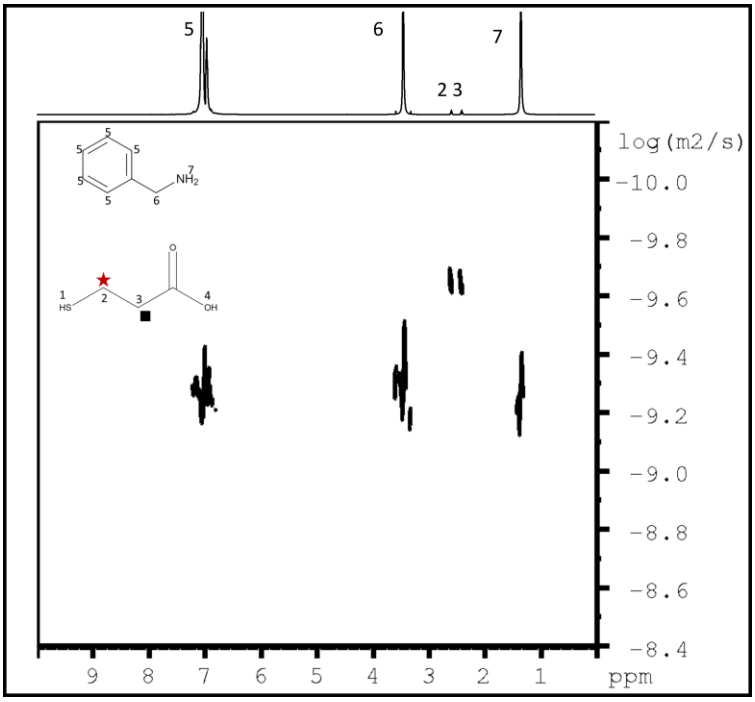

Figure 3.10: *Full scale ^{1}H DOSY NMR spectra of MPA ligand in BnzAm*

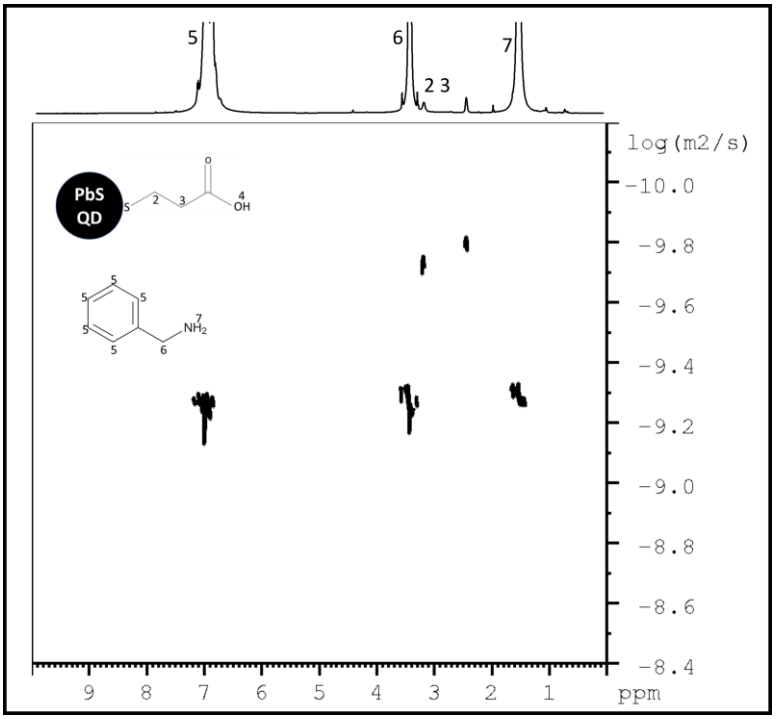

Figure 3.11: *Full scale ^{1}H DOSY NMR spectra of PbS-MP QDs in BnzAm*

CHAPTER 4

SINGLE SOLVENT-BASED p-TYPE AND n-TYPE PbS QUANTUM DOT INKS FOR SOLUTION PROCESSABLE OPTOELECTRONICS

4.1 INTRODUCTION

Colloidal semiconducting quantum dots (QDs) have garnered great interest for next generation of solar cells and photodetectors in recent decades. They have been explored for this role due to their size-tunable optical properties, compatibility with solution processing, and applicability to flexible substrates. These favorable characteristics stimulate the realization of low-cost and scalable devices on platforms unattainable with conventional single crystalline semiconductors. For example, multijunction solar cells incorporating QDs offer the possibility of increasing power conversion efficiency beyond the Shockley-Quiesser limit.

Record-setting QDs photovoltaic devices reported so far are fabricated either entirely or in part using solid-state ligand exchange (SSLE) technique to replace long aliphatic ligands used in the synthesis process. This is an inefficient process as only about 1% of synthesized quantum dots ends up being incorporated into the actual device[116]**.** This process is also incompatible and complications are further compounded when vertically stacked devices are fabricated through successive layer deposition processes.

During this process, underneath layers are exposed to solvents with varying polarity and ligand solutions that deteriorates the entire stack of layers. An alternative approach is to perform solution-phase ligand exchange to formulate QD ink that can subsequently be used to form compact film using more conservative processes e.g., spray painting or roll to roll printing technique in a single deposition step. Attention has been given to solution-based ligand exchanged processes to formulate quantum dot inks that can be used to produce inexpensive photovoltaic devices with minimal waste using printing techniques. In past, it has been reported that organic ligands with thiol moiety such as 3-mercaptopropionic acid (3-MPA) yields p-type QD and halide passivation (I/Br) yields n-type QD[107]. These QDs can be used to make a p-n junction type solar cell device. Previously these inks have suffered from stability issues mainly due to dispersion in highly polar coordinating solvents such as butylamine, DMF or DMSO that interact strongly with the PbS QD surface[34]. However, the exposure of n-type lead chalcogenides to oxygen tends to switch n-type QD to p-type material because oxygen can act as a p-type dopant. This shift in charge polarity limits their use in various photovoltaic device architectures[117–119].

Clearly, it is advantageous to explore more stable QD materials with enhanced solution and ambient stability. Furthermore, having n-type and p-type ink in single solvent system will improve the stacked device fabrication process as it'll eliminate the introduction of other polar solvents necessary to introduce secondary short ligand and to wash away free original long chain ligands from the film matrix.

In this study we have developed a simple, robust and scalable solution-phase ligand exchange process for the formation of p-type and n-type ink in a single solvent. In this chapter we are only focusing on n-type ink as p-type ink has been explained in previous

chapter (Chapter 3). This single solvent-based approach has raised the possibility of forming p-n junction solar cells and photodetectors using flexible and heat-sensitive flexible substrates. The use of benzylamine (BnzAm) as a stabilizing solvent has also improved the stability issues arising from highly coordinating and oxidizing solvents used previously. [96,105,107].

4.2 LIGAND EXCHANGE PROCESS

In this report we are describing highly stable halide (I^{-1}, Br^{-1}) capped PbS QDs, dispersed in a single non-coordinating organic solvent, that can be used to form p-type and n-type PbS QD solids, respectively. These inks can be used to form standalone heterojunction and p-n junction photovoltaic devices, and should be applicable to drop casting, spray, or roll-to-roll printing processes. The solvent system has advantage due to its compatibility to stabilize both p-type and n-type QDs, and with rest of the device architecture.

The biphasic ligand exchange and film deposition steps were conducted in a N_2 filled glovebox. Briefly, bound oleate concentration per QD were analyzed by quantitative NMR using ferrocene as an internal reference. A ligand population of 117/QD was obtained by integrating bound oleate peak around 5.6ppm and ferrocene peak at ~4 ppm. We used ~ 4-time access of I^{-1} and Br^{-1} ligands (1:1 ratio) with respect to original oleates per quantum dot. For this purpose, 16mg of NH_4I, 39mg of $PbBr_2$ and 99mg of PbI_2 were dissolved in 1mL of benzylamine. We noted that addition of NH_4I is required to dissolve $PbBr_2$ completely in BnzAm. One milliliter PbS QD stock solution (890 nm peak absorbance, 2.8 nm diameter) in n-octane (PbS QDs, 1076 nanomole/mL) were added drop wise to perform biphasic ligand exchange reaction.

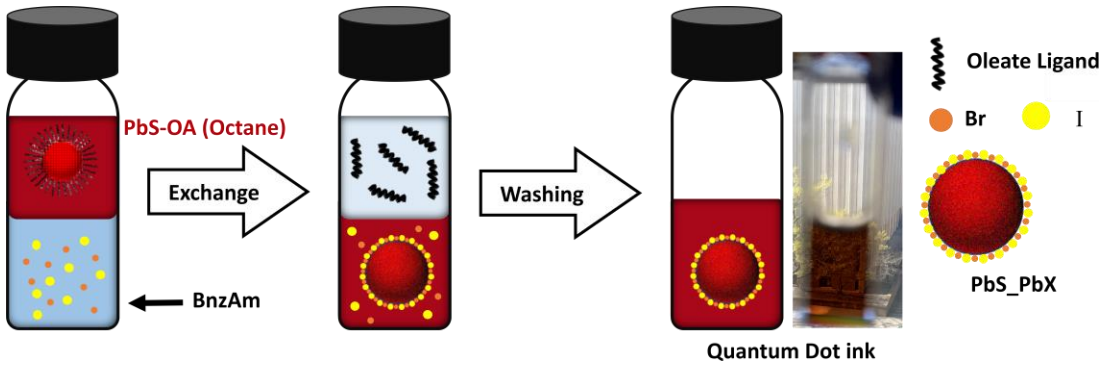

***Figure* 4.1:** *Biphasic ligand exchange process.*

QDs were transferred from non-polar n-octane phase to polar BnzAm solvent after ligand exchange reaction. Non-polar octane phase was carefully removed from top and QD solution was washed with 2mL of neat octane solvent three time to remove any free oleate ligand from the system. Finally, more BnzAm was added to make up the total volume to 500µL. The solution was filtered through 0.1µm PTFE syringe filter prior to chemical analysis and film fabrication.

4.3 RESULTS AND DISCUSSIONS

Ultraviolet-visible-NIR absorbance spectra of the oleate-capped QDs in n-octane and of the ligand-exchanged QD (PbS-X) solution are shown in **Figure 4.2**. Both spectra show a distinct lowest-energy electronic excitation (exciton) peak indicating presence of quantum confinement associated with of narrow size distribution of nanocrystals in the samples. A red shift was observed in ligand exchanged quantum dots, that we attribute primarily to change in surface chemistry and extension of QD's wavefunctions to nearest neighboring dots due to thinner ligand shell. We obtained homogenously dispersed QD solution without significant light scattering that could have been an indication of aggregation.

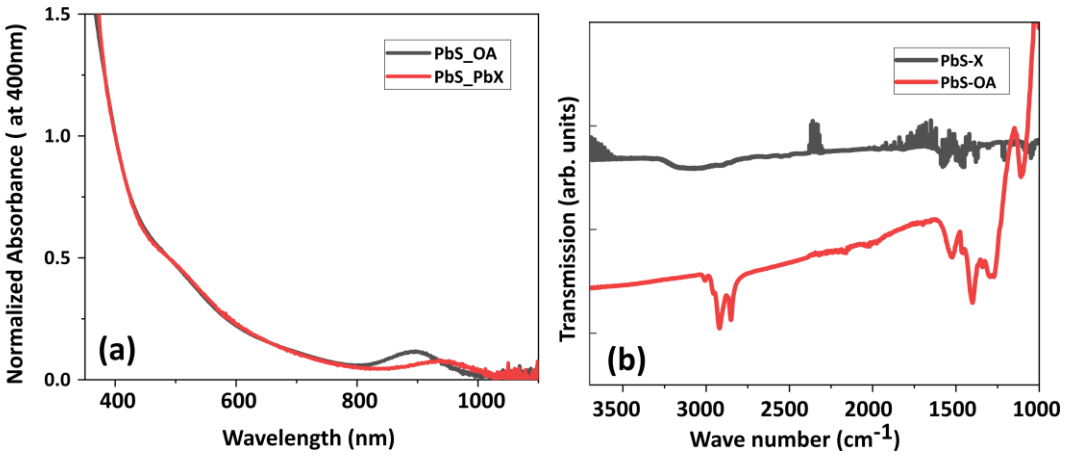

***Figure* 4.2:** *(a) UV-Vis absorption spectra (b) transmission FTIR of pre- and post-ligand exchanged PbS QDs*

Transmission Fourier Transform Infrared (FTIR) spectroscopy was used to assess the extent of the ligand exchange process by drop-casting thin film on salt plate. The absence of -CH_2 stretches in ligand exchange QDs in the broad range of 2800–3200 cm^{-1}, confirms that organic oleate ligands have been replaced successfully **Figure 4.2**. Furthermore, a comparison of the ^{1}H NMR spectra **Figure. 4.3** of PbS-OA and PbS-X showed distinct differences. The peak at 5.7 ppm associated with vinyl protons is significantly broadened for the oleate capped PbS QD that is an indication of strong ligand integration to QD surface. The reference peak at ~4ppm belongs to ferrocene which was used to quantify organic ligands in the sample.

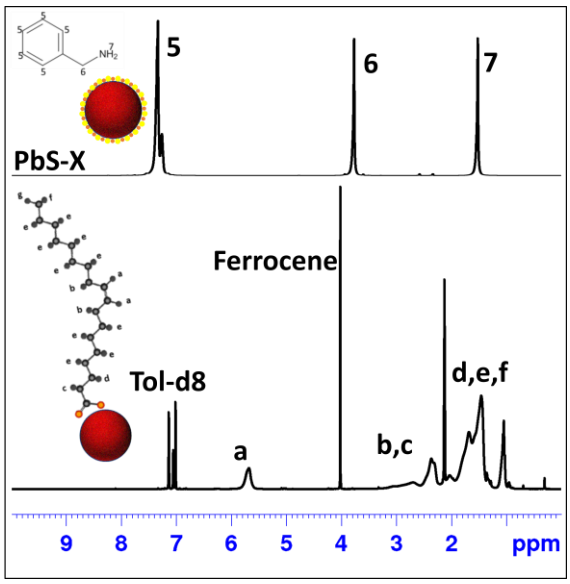

Figure 4.3: *^{1}H NMR spectra of (bottom) oleate capped PbS and (top) ligand exchanged PbS-X QDs*

The PbS-X QD solution NMR spectrum showed a lack of proton peaks associated with free or bound oleate and only peaks associated with BnzAm are present (reference Figure 3.7). The combination of FTIR and ^{1}H NMR spectroscopic analysis suggests the complete exchange of native oleate ligands and the installation of halide ligands (I^{-1}, Br^{-1}) on QD surface.

Previously it has been shown that energy level alignment plays an important role in solar cell device performance[89,120]. Therefore, it is important to analyze relative band edge and Fermi level positions for optimal device performance especially in vertical p-n junction heterostructures where QDs are treated with different ligands. We employed Ultraviolet Photoelectron Spectroscopy (UPS), Inverse Photo emission Spectroscopy (IPES) and X-ray Photoelectron Spectroscopy (XPS) to characterize position of Fermi level, valance band maximum, and conduction band minimum and surface composition in assembled films. Different capping ligands influence the Fermi level, ionization energy (IE) and

electron affinity (EA) in QD films differently. In this study, IE and EA are equated with valance band maximum and conduction band minimum respectively. We used a H Lyman-α photon source (E-LUX™121) with an incident photon energy of 10.2 eV for UPS and IPES experiments.

For this purpose, QD films were fabricated in an inert glovebox environment, and films were introduced to air atmosphere for 60 minutes to analyze the effect of air exposure on electronic properties. **Figure. 4.4(a,c)** shows the secondary cutoff region that was used to calculate the work function (WF), the graphs in the middle (b,d), shows the IE onset with the linear fit and the graphs at right (c,e), shows the IPES with the linear fit for PbS-MPA and PbS-X samples respectively.

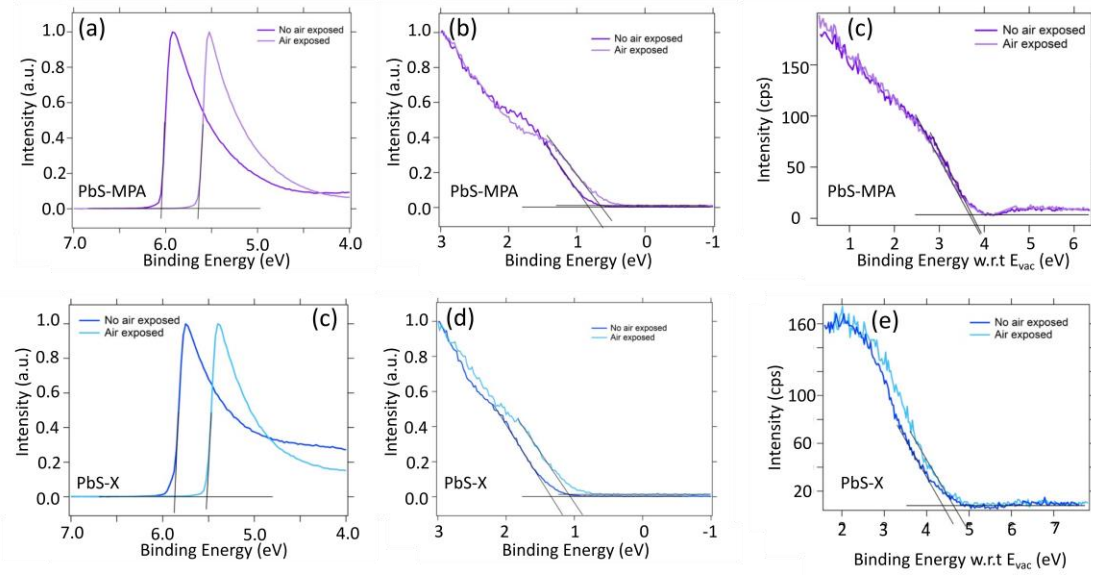

Figure 4.4: *The UPS graphs of as prepared and air exposed thin films of PbS-MPA and PbS-X showing (a,c) the secondary cut-off region to calculate the work function (WF) (b,d) the IE onset with the linear fit and (c,e) the IPES graphs with the linear fit*

Under inert atmosphere, it was observed that I/Br treatment leads to a more n-type character in assembled films (EA is essentially at E_F). On the contrary, MPA capped QDs

are fairly neutral. Exposure to air has a significant effect on band energies. It has comparatively less influence on PbS-X QDs but PbS-MPA samples has developed a more p-type character. This shift in Fermi level can play an important role in charge separation in heterojunction stacked devices operating in a normal air atmosphere.

The Fermi energy levels of PbS QDs shifted by up to 0.2 eV and conduction band up to 0.6eV in air as compared to inert atmosphere, depending on the ligand chemistry. This shift in energy can be credited to the influence of the total sum of ligand-QD interface dipole moment and the intrinsic dipole moment of the ligand[117,121]. Th shift in energy levels in air exposed samples could be due to oxidation of QD surface. The energy levels can also be influenced by the degree of passivation because trap filling can affect the surface doping parameters. The shift of PbS-MPA samples towards more p-type character is an indication of surface oxidation that is consistent with reported literature[122]. We confirmed this hypothesis by probing the surface chemistry using XPS analysis. The XPS spectra of Pb 4f core level indicates the shift in binding energy that we attributed to oxidation of Pb atoms on the surface.

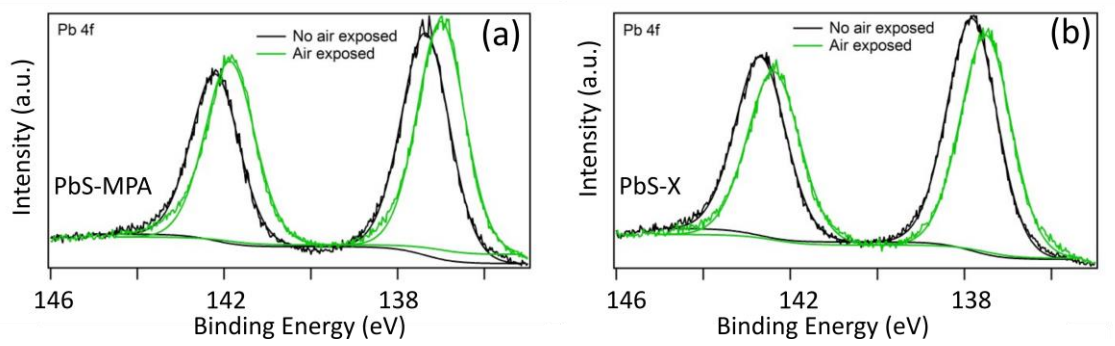

Figure 4.5: *XPS spectrum of the Pb 4f peak for PbS-MPA and PbS- for air free and air exposed samples.*

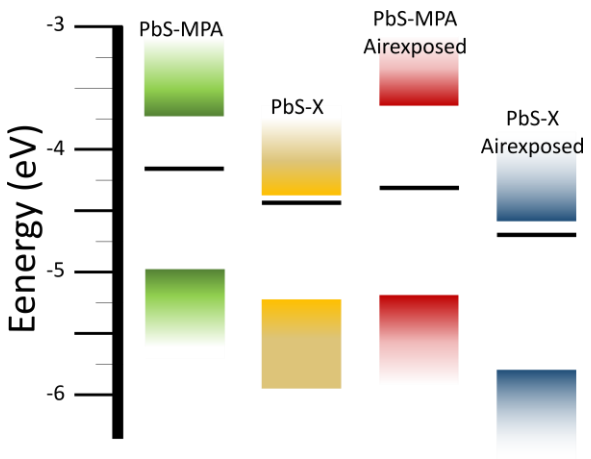

Figure 4.6: *Energy levels E_{CBM}, E_{VBM} and E_F (with respect to vacuum level) for PbS-MPA and PbS-X measured through UPS for air free and air exposed samples.*

UPS measurements on PbS QD films fabricated in inert atmosphere and exposed to air offer information on occupied electronic states providing numerical data about Fermi level E_F, CBM and VBM that is given in **Figure 4.6**. These results indicate the importance of the measurements and the knowledge of energy levels while designing an optoelectronic device architecture. It also stresses on the fact that chemical environment greatly influence these values and the measurements must be carried out in an environment that is close to the working environment during the device operation.

4.4 FUTURE PROSPECTS

In literature, high efficiency photovoltaic devices based on colloidal quantum dots are based on p-n junction heterostructures. This architecture allows efficient charge separation and extraction during device operation. Many of these device uses a p-type QD layer or polymeric hole transport layer that is deposited through layer-by-layer ligand exchange and film fabrication approach. This LBL technique exposes the previous layers to polar solvents. This process also introduced the incoming ligands and the one that are

being replaced, deep into already formed film matrix. This process compromises the chemical structure of entire device and electronic charge transport. To deal with these issues, in this study we have developed n-type and p-type QDs that are dispersed in a single solvent system. This will allow researchers to not only fabricate stacked devices using more conservative film fabrication routes like spray coating and printing but will also preserve the chemistry of previous layers protecting its optoelectronic properties for maximum power output. Additionally, these colloidally stable inks fulfil an important design criterion for efficient p-n junction design that is a positive ΔE_{CB}, given by[123]:

$$\boldsymbol{\Delta E_{CB} = E^{D}_{CBM} - E^{A}_{CBM}} \qquad \text{Eq.4.1}$$

Here, E^{D}_{CBM} is the VBM of donor (p-type, electron donor) and E^{A}_{CBM} VBM of accepter (n-type, electron accepter) material. ΔE_{CB} must be sufficiently large for efficient separation of photogenerated charge carriers by preventing unwanted back transfer.

4.5 MATERIALS AND METHODS

The following reagents for synthesis and subsequent ligand exchange were used as received. Lead (II) oxide (PbO, 99.9%), anhydrous toluene (99.8%), and 1,2-ethanedithhiol (EDT, 98%) were purchased from Alfa Aesar. Bis(trimethylsilyl) sulfide ((TMS)2S, 95%) and 1-octadecene (ODE, 90%) were purchased from Acros Organics. For PR (Precipitation/re-dispersion) purification, methyl acetate (MeOAc, 99 %) purchased from Millipore Sigma was purged with nitrogen for 60 minutes and dried over activated 4A molecular sieves in a nitrogen glovebox.

PbS colloidal quantum dots synthesis: PbS QD were synthesized as mentioned in Chapter 3. As-synthesized oleate capped PbS QDs have lowest energy electronic transition

(λ1s) peak centered at 880 nm (1.4 eV), indicating 2.8 nm diameter as estimated through a previously published sizing curve.

Biphasic Ligand Exchange Process: A ligand population of 117/QD was measured by integrating bound oleate peak around 5.6ppm and ferrocene peak at ~4 ppm. The 4-time access of I^{-1} and Br^{-1} ligands (1:1 ratio) with respect to original oleates per quantum dot by dissolving 16mg of NH_4I, 39mg of $PbBr_2$ and 99mg of PbI_2 in 1mL of benzylamine. We noted that addition of NH_4I is required to dissolve $PbBr_2$ completely in BnzAm. One milliliter PbS QD stock solution (890 nm peak absorbance, 2.8 nm diameter) in n-octane (PbS QDs, 1076 nanomole/mL) were added drop wise to perform biphasic ligand exchange reaction. QDs were transferred from non-polar n-octane phase to polar BnzAm solvent after ligand exchange reaction. Non-polar phase was carefully removed from top and QD solution was washed with 2mL of neat n-octane three time to get rid of any free oleate ligand from the system. Finally, more BnzAm was added to make up the total volume to 500μL and solution was filtered through 0.1μm PTFE syringe filter.

NMR spectroscopy: ^{1}H NMR of the PbS-OA and PbS-X deuterated toluene and in normal proteo benzylamine were performed on a Bruker Avance III-HD 400 MHz spectrometer. Reference spectra for PbS-OA and benzylamine in methanol were recorded in methanol-d4 and are given in Chapter 3. Figure 3.7 contains full scale ^{1}H NMR spectra

Sample preparation for UPS/IPES/XPS: ITO coated glass substrates with area ~2 cm^2 were cleaned by washing with detergent and then sequentially sonicated in acetone, IPA, ethanol, and dionized water for 5 minutes each before drying by nitrogen flow. 15 μL of PbS-X solution was dropped and spread on entire substrate by spinning at 1500 rpm for 30 s, and left in glove box to dry. The process was repeated to make a ~50 nm thick film.

UPS: H Lyman-α photon source (E-LUX™121) with photon energy 10.2 eV was used to collect data that is plotted as binding energy with respect to E_{Fermi}.

XPS: PHI 5600 ultrahigh vacuum system (UHV) with a hemispherical electron energy analyzer was used. The system was equipped with Al Kα source (1486.6 eV, PHI 04-548 dual anode X-ray source) for excitation. The sample were analyzed for small area at 45° angle and the pass energy of 23.5 eV

IPES: A 280 nm filter was used and data is plotted as binding energy with respect to E_{vac}.

CHAPTER 5

$AgBiS_2$ QUANTUM DOT INK FOR ENVIRONMENT FRIENDLY SOLUTION PROCESSABLE OPTOELECTRONICS

5.1 INTRODUCTION

Solution processable semiconducting materials, especially colloidal quantum dots (QD) with size-dependent bandgap, have gained much attention for their applications in flexible optoelectronic devices. These materials are important as they don't need complicated equipment and hug setup investment for industrial applications[124]. Among the available most economical processing technologies, spray or roll to roll printing, require a kind of nano-ink that can be deposited in a single step fabrication process. Doing so, thin-film stacked devices and circuitry can be formed on heat-sensitive and flexible substrates to make flexible wearable devices and sensors[125,126]. To date, cadmium and lead sulfide are the best performing and promising QD nanomaterial systems for solar cells and Near infrared (NIR) photodetectors[127]. However, these QDs are affected by restriction of hazardous substances (RoHS) directives. In many parts of the world there is now, or soon to be, legislation to restrict, and in some cases ban the toxic heavy metals in consumer and household appliances such as lighting equipment, consumer electronics, leisure & sports equipment[125,128]. Therefore, there is a strive for non-hazardous, earth-abundant QD materials, free of toxic heavy metals.

Recently, environment-friendly silver bismuth sulfide ($AgBiS_2$) nanocrystals has emerged as a RoHS compliant material for its application in low cost and flexible optoelectronics[129]. Inert under ambient atmospheric conditions, $AgBiS_2$ colloidal nanocrystals with lower dimensions exhibit the band gap values of 1–1.32eV with high extinction coefficient of $< 10^5\,cm^{-1}$, and promising photoconductivity has been demonstrated as an alternative to PbS CQDs[18,130–132].

Since the discovery of colloidal QDs, one of the main challenges is to assemble these NCs into defect free and compact film. Mostly, NCs are synthesized in the presence of surfactant molecules (surface ligands) to preserve NC's size and maintain colloidal solubility. In order to fabricate functional device and promote charge transport, these bulky insulating ligands are partially or fully exchanged with smaller molecules during device fabrication process. Early studies of ligand exchange reaction in $AgBiS_2$ systems are limited to a tedious layer-by-layer (LBL) solid state deposition and ligand exchange process. In order to get a reasonably thick and compact films, 10-15 cycles of alternating coating, treatment, and washing steps are involved suing large amount of solutions, which is a waste of resources and as only about 1% of the synthesized NCs ends up being incorporated into final assembled device[133]. This sequential technique does not allow good quality films and the extent of ligand exchange depends on reactivity and penetration depth of incoming ligand molecule. This LBL technique is not suitable to form flexible devices on polymeric substrates that is a major application for colloidal quantum dots. This process also involves washing steps using large quantities of polar and non-polar solvents that deteriorates the previous layers and the substrate itself. Electronically, unwashed residual ligands incoming ligands and unreplaced native ligands along with dangling bonds can also

form barriers and traps to limit the flow of charge carriers[126,134]. These problems can be overcome by performing ligand exchange completely in solution phase to form NCs inks. These inks then can be used through more conservative and industrial film deposition techniques that are free from sequential chemistry such as, spray coating, roll to roll printing and doctor blading. This process offers the potential for deposition of thicker uniform films in a single step fashion to fabricate large area and flexible devices on heat and solvent sensitive substrates.

Previously, almost all $AgBiS_2$ device reports to date have used a solid-state ligand exchange (SSLE) process form NCs assembly to fabricate conductive thin films. We recently published a study on a fast solution phase ligand exchange process to generate iodide stabilized $AgBiS_2$ nanocrystal inks through a biphasic transfer reaction. In this approach NCs with long chain ligands are dispersed in a non-polar solvent while short chain ligands and ions are dissolved in polar solvent. After biphasic ligand exchange, these NCs then can be washed with neat non-polar solvent to remove native ligands. The ligand exchange reaction, on mixing both solutions, brings the NCs from non-polar to polar solvent where the stability of particles relies largely on electrostatic stabilization[34,135]. To date, most solution phase ligand exchange reports are on installing metal-free inorganic ligands or metal chalcogenide complexes [134,136–138] resulting in n-type conductivity in these films. There are handful reports on p-type inks due to the difficulty of stabilizing thiol based small molecules in polar solvents. We published a report on stabilizing 3-marcatopropionic acid (MPA) capped PbS QDs in benzylamine through electrostatic interaction between ligand and solvent. In this report, we are extending the concept in formulation of environment friendly, less toxic MPA stabilized $AgBiS_2$ QDs ink to

fabricate flexible NIR photodetectors for advanced deployment in next-generation of robotics in food industry and personal healthcare in biomedical devices.

5.2 SOLUTION PHASE LIGAND EXCHANGE PROCESS

The $AgBiS_2$ ink formulation process is outlined in **Figure 5.1**. Briefly, oleate capped $AgBiS_2$ QD were synthesized through a hot injection method. In first step, silver and bismuth precursor are reacted with oleic acid to form metal oleates in the presence of octadecene which is a high boiling noncoordinating solvent. In second step, Sulphur was added to the oleate mixture at an elevated temperature under inert atmosphere to form $AgBiS_2$ QD (detailed procedure is given in method section). As synthesized QDs were isolated from growth solvent and reaction by-products using centrifugation process. Methyl acetate was used as anti-solvent to promote aggregation. Isolated QD were then redispersed in neat n-octane, aggregated again using methyl acetate, centrifuged and were isolated. These purified solid QD were then redispersed back into anhydrous n-octane solvent inside glove box. Oleate concentration in this QD sample was estimated using quantitative NMR, by introducing ferrocene as an internal standard. Since nanocrystal sizing curves are not available in literature for $AgBiS_2$ to calculate QD concentration and consequently ligand per dot, we used quantitative NMR to measure total oleate ligand concentration in the system. We compared the ferrocene peaks as reference to quantify strongly interacting oleate specie to estimate the oleate concentration in the sample. We estimated oleate concentration ~ 2.9×10^{-5} mole/mL. For ligand exchange, 32mg of MPA (doubled the oleate concentration) was dissolved in methanol. 2mL of QDs, dispersed in n-octane were added to MPA solution dropwise under vigorous stirring to accelerate ligand exchange. As a result of this exchange, QDs were transferred from non-polar n-octane

phase (top) to polar MeOH phase (bottom). The top n-octane layer was carefully decanted. Fresh n-octane was added to dissolve and remove any leftover oleate ligand from the system, this process was repeated three times. After removal of n-octane in last wash cycle, QDs were centrifuged at 2000rpm and access MeOH was removed. Benzylamine was added as solvent and leftover MeOH from the mixture was removed under partial vacuum. This prepared ink was then passed through a 0.1um PTFE syringe filter and was used for analytical characterization and to build photodetector devices using spin coating technique. Here, MeOH has the dual advantages of weaker interaction with the QD surface as compared to mostly used dimethylformamide (DMF). Its low boiling point compared to BnzAm allows the effective removal of methanol from the QD-MPA/BnzAm/MeOH mixture under partial vacuum.

We have performed comprehensive quantitative and qualitative analysis on the MPA-capped $AgBiS_2$ quantum dot ink, and on photoconductive test devices made using it.

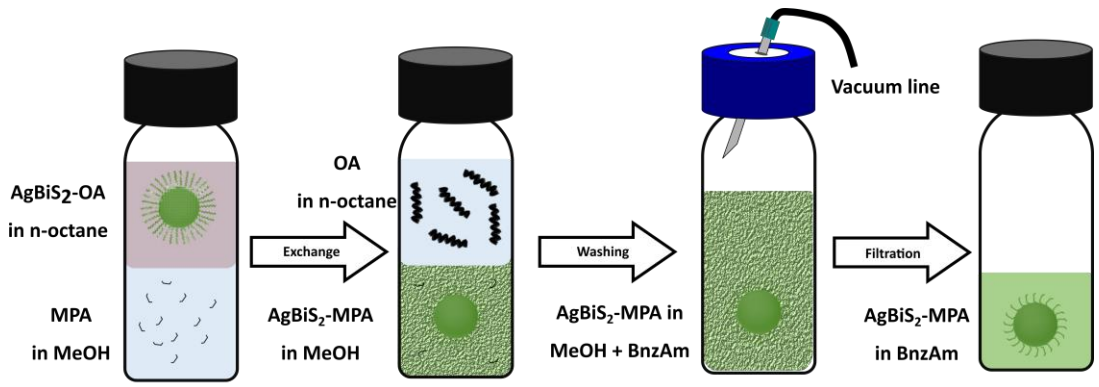

Figure 5.1: *Biphasic ligand exchange process.*

5.3 RESULTS AND DISCUSSIONS

Ultraviolet-visible absorbance spectra of the oleate-capped QDs in octane and of the ligand-exchanged $AgBiS_2$-MPA QD in BnzAm are shown in **Figure 5.2a**. Since, $AgBiS_2$ does not exhibit a strong quantum confinement, it lacks the characteristic's absorbance peak as observed for other such QDs with stronger confinement due to larger Bohr's radius. The overall absorbance curve is similar for both pre and post ligand exchanged QDs. To further evaluate efficacy of ligand exchange process, we used transmission mode FTIR spectroscopy. For this purpose, thin QD films were prepared using drop casting technique onto salt plat.

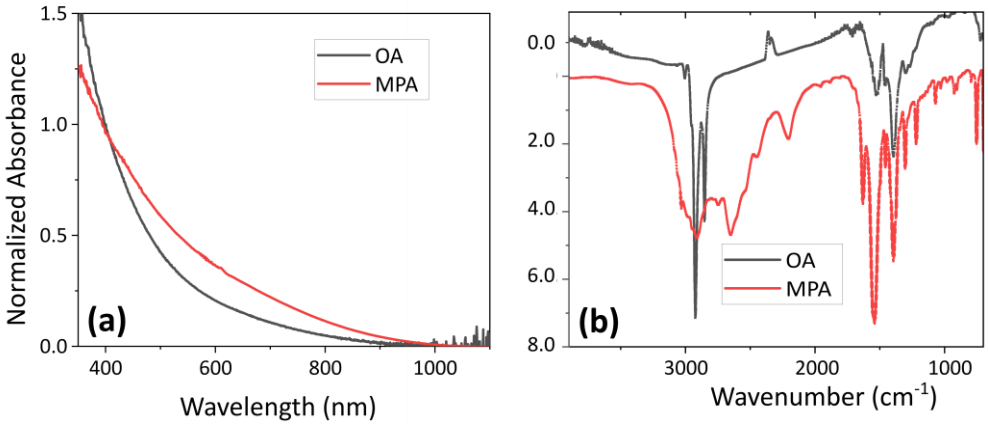

***Figure* 5.2:** *(a) UV-Vis absorption spectra of pre- and post-ligand exchanged $AgBiS_2$ QDs (b) FTIR absorption spectra of films*

Resulting transmission FTIR spectra are shown in **Figure 5.2b**. The suppression of strong peak around 2900cm^{-1} indicates the removal of -CH_2 of oleate ligand. A new peak around corresponds to -SH around 2800cm^{-1} appears that confirms the installation of thiol containing MPA ligands on $AgBiS_2$ quantum dots[139,140]. Since both native ligand (oleate) and incoming ligand (MPA) contains -CH_2 groups, it is difficult to establish the extent of

ligand exchange process. NMR is a convenient and most suitable technique to identify organic matter in solution samples. We used 1D ^{1}HNMR and Diffusion Ordered ^{1}H Spectroscopy (DOSY) NMR techniques to identify the species present in pre and post ligand exchange samples.

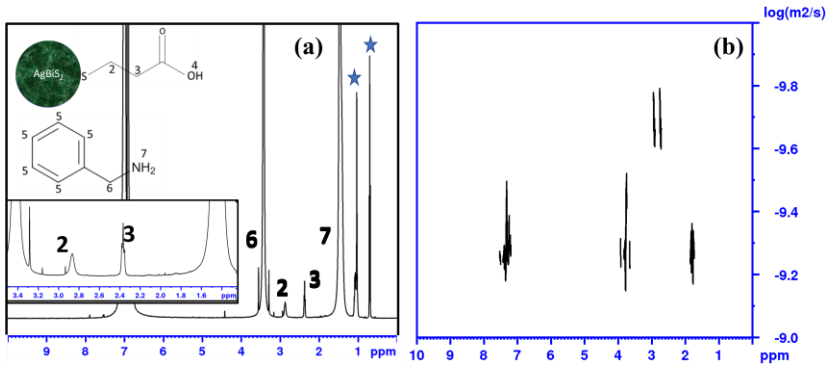

Figure 5.3: *(a) ^{1}H NMR spectrum of QD-MPA in benzylamine. Inset: magnified scale revealing MPA methylene resonances. (b) Corresponding DOSY plot indicating slow effective diffusion constant for MPA interacting with the QD surface.*

For the ligand exchanged samples, proteo solvent with natural abundance of proton was used due to unavailability of deuterated BnzAm solvent. In the 1D ^{1}H spectrum is shown in **Figure 5.3a**, indicates no free or bound or OA could be detected in the final ink solution. On the other hand, the alkyl proton peaks of MPA in the QD-MPA sample are significantly broadened and shifted from those observed when MPA is added to clean BnzAm solvent in the absence of QDs (**Figure 3.7**). The broadening of NMR signals indicates that there is only single species of MPA in the sample that is strongly coordinating with QD's surface at NMR's timescale. Diffusion ordered spectroscopy; a pseudo-two-dimensional NMR technique, is a powerful tool to separates NMR signal based on difference in diffusion constants and identifies which species in solution participate at the surface of QDs[141,142]. Any such specie attached to the surface of the QD act as a large

molecule and diffuse slowly. DOSY technique taking advantage of difference in diffusion constants, separates the ^{1}H signals of species bound to the QD from those that are free molecules. For a molecule with free and bound population in a sample, the observed diffusion coefficient is weighted average of free and bound fractions.

DOSY NMR analysis **Figure 5.3b** confirms the identify of ligands on the surface of QDs by comparing the diffusion coefficient of MPA in $AgBiS_2$-MPA sample to that of free MPA in neat BnzAm solvent. The diffusion constant of MPA in QD sample was significantly lower indicating that MPA is the only specie bound to the QD under the conditions studied.

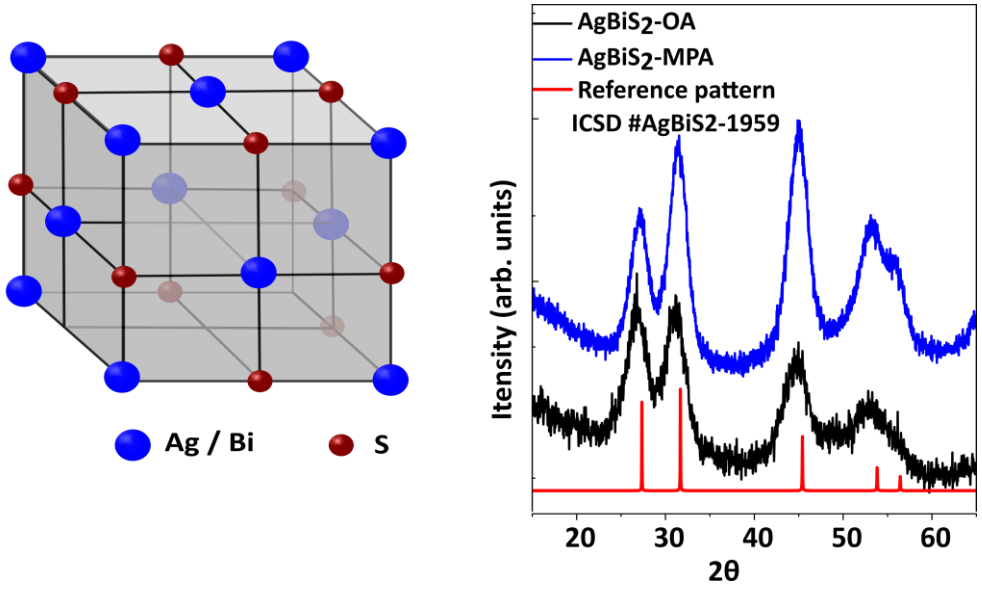

Figure 5.4: *Powder Xray Diffraction (P-XRD) analysis of pre and post ligand exchanged quantum dots with a reference peak pattern of $AgBiS_2$ unit cell in the cubic phase*

$AgBiS_2$ system has been shown to exhibit two phases, β-phase with a cubic structure and α-phase which has a trigonal-hexagonal structure. However, it is important to obtain single phase material to mitigate disorder in fabricated films and only cubic phase has been shown to exhibit quantum confinement when nano crystallite size is reduced with

high extinction coefficient[127]. As, Ag metal nanoparticles, AgS_2 and BiS_2 form stable compositions with all possible intermediate species $Ag_{(x)}Bix_{(x-1)}S_2$, it is vital to characterize the material crystal structure. We performed powder x-ray diffraction (XRD) analysis to examine crystal structures of nanocrystals. Powder XRD patterns of as-prepared and ligand exchanged $AgBiS_2$ nanocrystals is shown in **Figure 5.4**, that confirms the formation of phase pure highly crystalline cubic $AgBiS_2$ nanocrystals without the presence of any other species or additional impurities. All XRD peaks are in perfect agreement with reference ICDD $AgBiS_2$ -1959 confirming cubic schapbachite phase of $AgBiS_2$.

Table 5.1. Elemental composition of pre and post ligand exchanged dot

Element	$AgBiS_2$ OA Atomic (%)	$AgBiS_2$ MPA Atomic (%)
Ag	25.01 ± 2.6	19.41 ± 2.06
Bi	23.01 ± 1.4	20.6 ± 1.28
S	51.98 ± 2.8	59.99 ± 2.9

For the quantitative examination, we used energy dispersive X-ray analysis (EDX) to determine the elemental composition of QDs. Our results indicates that Ag and Bi are present in nearly 1:1 ratio, in as synthesized and ligand exchanged quantum dots **Table 5.1**. There is no observable change in elemental composition pre and post ligand exchanged QD except the increased Sulphur (S) content from the edition of MPA which contain thiol moiety to bound to QD surface.

Scanning transmission electron microscope (STEM) was used to confirm the formation of nanocrystals and observe any change before and after ligand exchange process. Images displayed in **Figure 5.5** revealed a significant decrease in the interparticle

distance between neighboring MPA-capped dots deposited from the BnzAm solvent compared to those with oleate capping. This is consistent with a thinner ligand shell in post ligand exchange dots, while the QDs retain a similar size distribution. Any change in the quantum dot size is negligible.

Spin coating technique is a convenient method at laboratory scale to form very thin, smooth, and uniform films for test devices but the ink-based approach can be used in variety of other deposition techniques such as spray coating, doctor blading and roll to roll printing for industrial applications. For this study, assembled $AgBiS_2$ quantum dot film morphology and electronic properties were analyzed by depositing QD ink on Si/SiO_2 substrate using a low-speed spin coating technique. We formed two-terminal lateral transport devices on Si/SiO_2 substrates with pre-patterned Ti/Au (15 nm/25 nm thickness) bottom contacts defined by photolithography and formed by electron beam evaporation. Atomic force microscopy was used to analyses film thickness and film morphology **Figure 5.5c.**

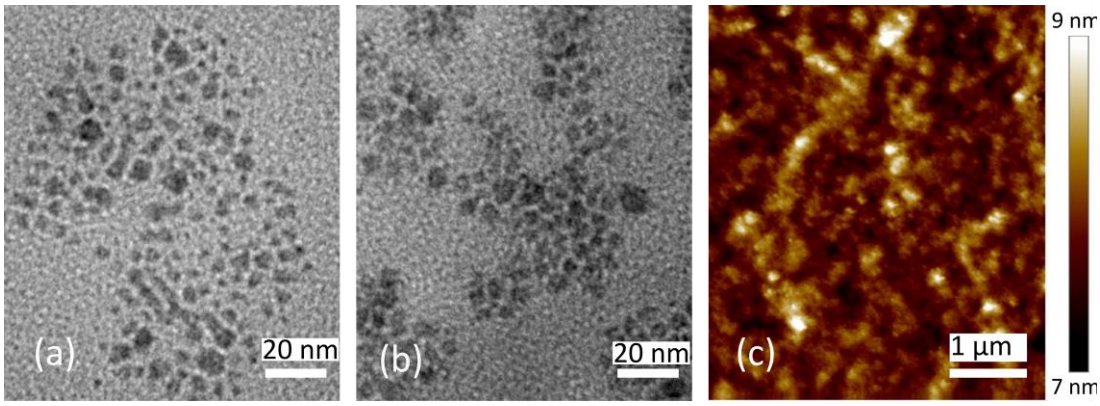

Figure 5.5: *STEM images of (a) oleate capped and (b) MPA capped $AgBiS_2$ QDs (c) atomic force microscopy micrograph*

The film showed a very smooth surface morphology with a RMS surface roughness of 2.2nm that is comparable to other state of the art quantum dot systems deposited through more traditional layer by layer ligand exchange and film fabrication approach[110,111]. Such a smooth film morphology is important to reduces the possibility of short circuiting and prevent current leakage in vertically stacked devices.[112]. In first set of electronic measurements, film conductivity was measured using the transfer line model (TLM) that can separate material's resistivity from contact resistance. For a ~90nm thick film deposited through spin coating technique, we obtained a film resistivity of 3.6×10^{3} KΩ.cm (conductivity of 2.8×10^{-7} S/cm). These conductivity values are an order of magnitude better than previously published[18] values for $AgBiS_2$ and on par to some early reports of the other state of the art quantum dot systems[70]. Since this material is developed for application in photodetection devices, the devices were tested for photoresponse.

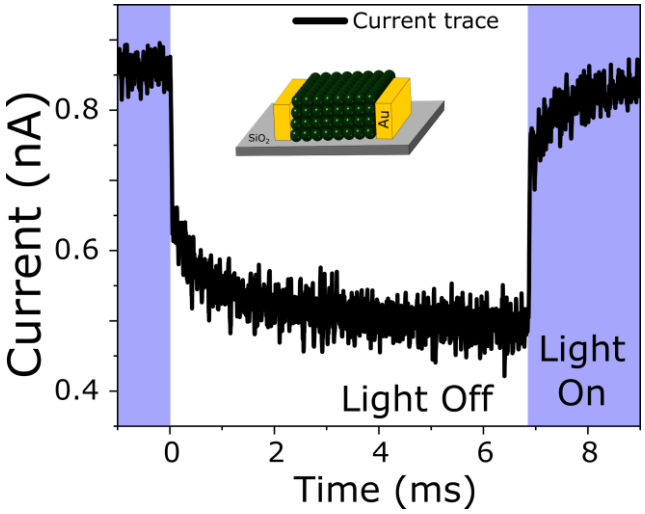

Figure 5.6: *Photocurrent trace of bottom contacted device under chopped 444nm light*

When shined with 444nm laser light the device responded very quickly to exhibit increased conductivity under 10V applied bias. The 55 microseconds turn Off time was observed indicating material's suitability in high-speed photodetectors **Figure 5.6**. This on/off time is much shorter than previously reported values that are in several seconds[143].

The heterojunction vertical stacked device is an appropriate configuration for a photodetection device that allowed us to make asymmetric contacts to the light absorbing layer. This is also an appropriate structure to establish the type of majority charge carriers in the material. In this configuration, an n-type wide bandgap oxide (ZnO, TiO_2) is used as electron collection layer improving charge extraction in photovoltaic operations[144] . To evaluate $AgBiS_2$ material for photodetection application, we fabricated a vertical stacked device (ITO/TiO_2/$AgBiS_2$-MPA/Au) using spin coating TiO_2 and QD ink. A top gold electrode approximately 100nm thick was defined and deposited using a shadow mask and ebeam metal evaporation technique.

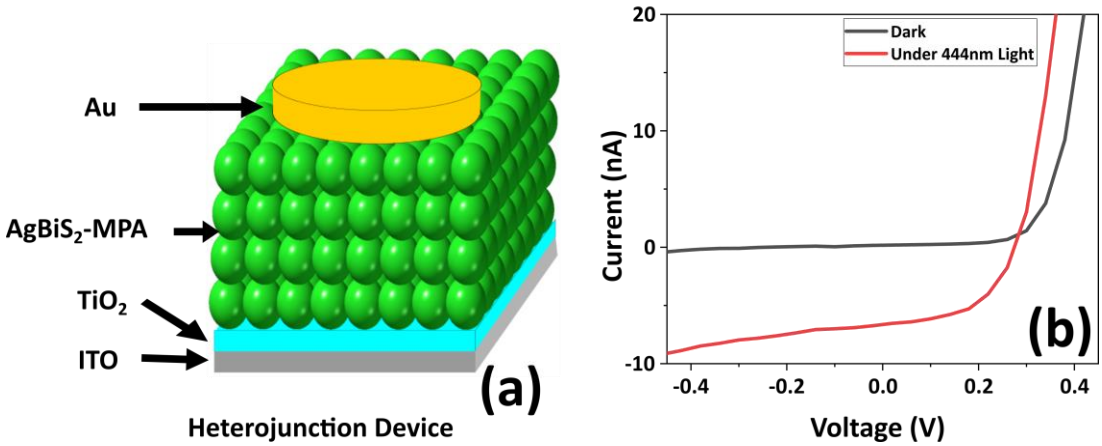

Figure 5.7: *(a) a vertically stacked heterojunction device structure (b) I-V curve under dark and 444nm monochromatic light, inset depicts the band edge positions*

The I-V curves under dark and illumination is shown in Figure 5.7. This rectifying *I-V* confirms $AgBiS_2$ as a p-type material. This is a key requirement to efficiently extract photoexcited holes by keeping the dark conductivity as low as possible to get improved detectivity of photo detecting devices[145]. We used an unoptimized film thickness for this test device that can be optimized for improved device performance. Film thickness plays an important role for a photodetection device as there is always a trade-off between light absorption and charge extraction before it recombines. The later can be overcome by operating the device in reverse bias that widens the depletion region and enhances the photocurrent generation. We measured the external quantum efficiency (EQE) in NIR region near the bandgap (800nm to 1500nm) at 500mV reverse bias using **Equation 5.1**.

$$R = \frac{I_{Light} + I_{Dark}}{P_{incident}} \qquad \text{Eq.5.1}$$

Figure 5.8 indicates the responsivity curve for a heterojunction device, while the incident power was measured using a commercial photodetector with known responsivity.

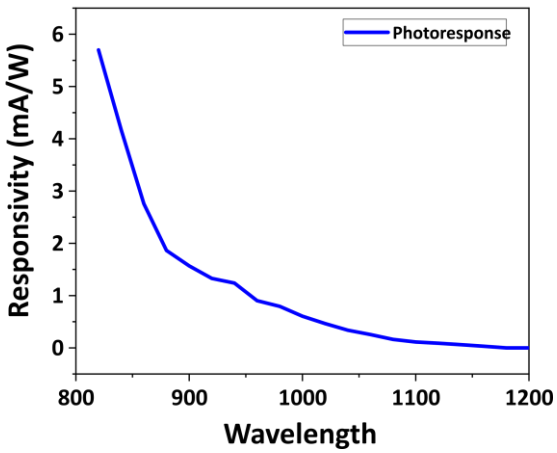

Figure 5.8: *Action spectrum of heterojunction device at 500mV reverse bias indicating wavelength dependent response in terms of responsivity.*

This device exhibits similar photoresponsivity as reported earlier[146]. We also measured the optical and electronic bandgap of $AgBiS_2$ QD using UV-vis-NIR absorbance in solution, assembled solid film and using responsivity curve. The tauc plot fitting model for amorphous materials was used to estimate a bandgap of 1.1eV in post ligand exchange solution phase QD sample, 1.02eV in thin film on glass and 1.05eV electronic bandgap **Figure 5.9**. These values are consistent with previous reports and confirms the detectivity of $AgBiS_2$ QD up to NIR wavelengths making it a suitable choice for light detection in biomedical applications[18].

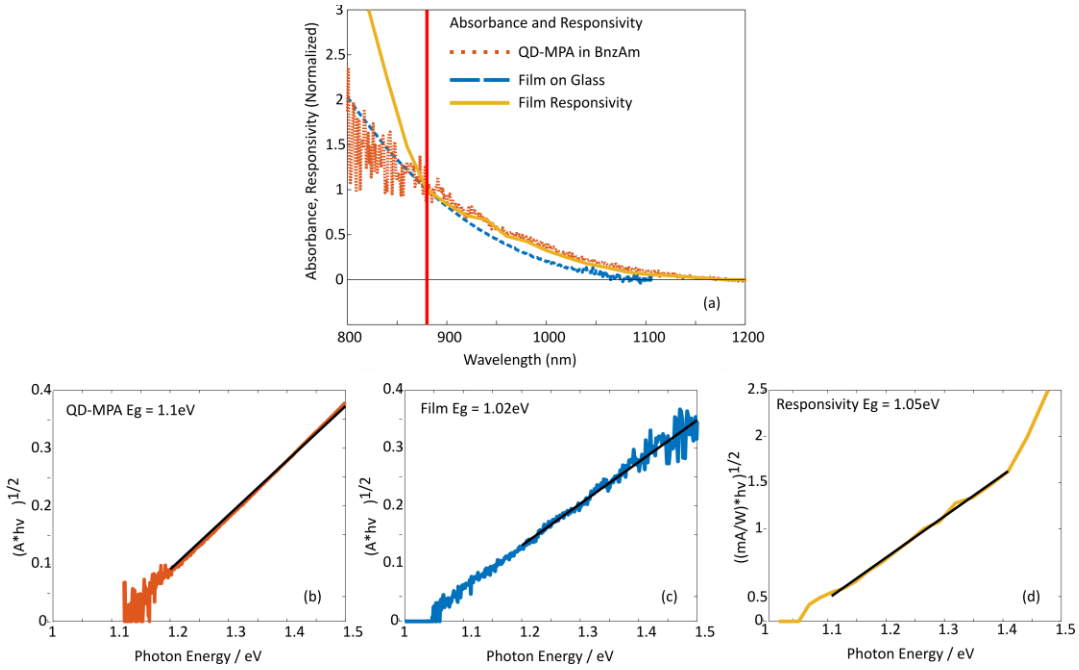

Figure 5.9: *(a) Action spectrum of heterojunction device, absorption curves for solution phase and a thin film of $AgBiS_2$ QDs (b) Tuac plot fitting curves for (b) QD in solution (c) QD thin film on glass substrate (d) photoresponse action spectrum at 500mV reverse bias.*

5.4 FLEXIBLE PHOTODETECTOR

For the fabrication of flexible QD photodetectors, we have fabricated a photodetection device using polyethylene terephthalateto (PET) substrate in a lateral device configuration.

The assembled device with top gold electrodes works as a photoresistor. For this purpose, a 100nm thick QD film was fabricated using low speed spin coating technique and top gold contacts were realized using a shadow mask and electron beam metal deposition process. Assembled devices were tested in flat and bent mode to demonstrate a bendable performance under 444nm incident light **Figure 5.10**. Surprisingly, the photoresponse of these lateral flexible devices was almost unchanged when bent to 180° as demonstrated in Figure 5.10f. The devices were tested in flat mode and when curved with 1" and 0.5" radius of curvature.

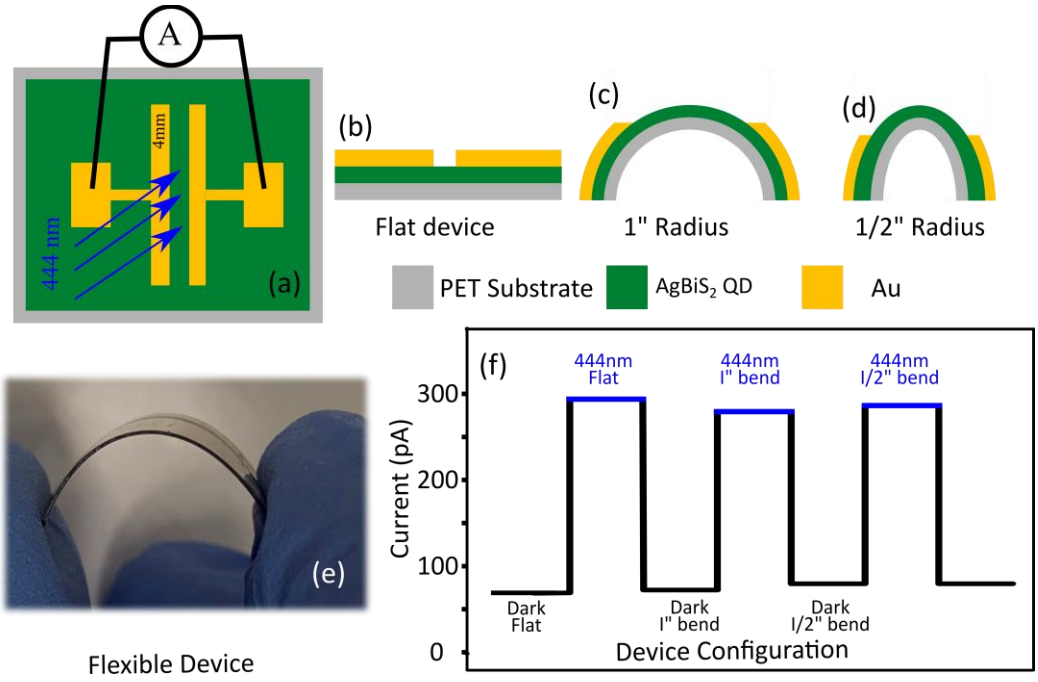

Figure 5.10: *Flexible device structure fabricated on PET substrate (a) top view of lateral device (b) side cross-sectional view of device (c) bent device with 1 inch radius (d) bent device with ½ in radius (e) optical image of actual flexible device in bent form (f)dark and photocurrent response of the device in flat and bent forms.*

5.5 CONCLUSION

In this study, we realized an environment friendly, less toxic QD ink that combines excellent colloidal stability with anticipated industrially compatible thin film deposition using spray coating and roll to roll printing techniques. This low-cost ink exhibit excellent optoelectronic characteristics and smooth film morphology important for stacked heterojunction devices necessary to obtain superior photo detectivity. We then employed this ink to demonstrate its applicability in heterojunction and flexible photodetection devices operating in NIR spectral range for food industry and biomedical applications. This low-cost solution processable will enable integration of QDs into mechanically robust flexible photodetectors for various advanced utilizations that the rigid counterparts cannot perform.

5.6 MATERIALS AND METHODS

Silver(I) acetate (Ag(OAc), ≥ 99 %), Bismuth(III) acetate (Bi(OAc)3, ≥ 99 %), and ammonium iodide (NH_4I, ≥ 99.0 %) were purchased from BeanTown Chemical. Oleic acid (≥90 %) was purchased from Alfa Aesar. Bis(trimethylsilyl) sulfide ((TMS)2S, 95 %), n-octane (97 %), and 1-octadecene (ODE, 90 %) were purchased from Acros Organics. Methyl acetate (MeOAc, 99 %) was purchased from Millipore Sigma. Octane, ODE and MeOAc were dried under activated molecular sieves in a nitrogen glovebox following degassing under partial vacuum prior to use. All other reagents were used as received without further modification.

$AgBiS_2$ colloidal quantum dots synthesis: Colloidal $AgBiS_2$ nanocrystals were synthesized using a modified reported procedure[130]. In a nitrogen glovebox, $Bi(OAc)_3$ (1 mmol, 386 mg), Ag(OAc) (0.8 mmol, 134 mg), ODE (2 mL) and Oleic acid (17 mmol,

4.974 g) were loaded to a 100 mL 3-neck round bottom flask attached with an air condenser. The reaction mixture was degassed under vacuum at 100 °C for 30 minutes with stirring to form silver and bismuth precursors. The reaction vessel was then purged with nitrogen gas, and TMS_2S (1 mmol, 210 µL) diluted in 5 mL of ODE was swiftly injected at an injection temperature of 100 °C, forming the crude, brown reaction product. The heating mental was removed and reaction flask was cooled to room temperature naturally and the reaction flask was protected from light until the precipitation step.

$AgBiS_2$ nanocrystals were isolated from reaction mixture under air free conditions using dry MeOAc as the antisolvent. Separated QDs were redispersed in neat n-octane solvent and process was repeated twice to remove reaction by-products and solvents. The purified sample was stored in a nitrogen glovebox in n-octane for further use.

Biphasic Ligand Exchange Process: For ligand exchange, 32mg of MPA (doubled the oleate concentration) was dissolved in 2mL of methanol. 2mL of QDs, dispersed in n-octane were added to MPA solution dropwise under vigorous stirring to accelerate ligand exchange process. As a result of this exchange, QDs were transferred from non-polar n-octane phase (top) to polar MeOH phase (bottom) and the top n-octane layer was carefully decanted. Octane layer from top was removed, fresh n-octane was added to dissolve and remove any leftover oleate ligand from the system, this process was repeated three times. After removal of n-octane in last wash cycle, benzylamine was added as solvent and MeOH from the mixture was removed under partial vacuum. This prepared ink was then passed through a 0.1um PTFE syringe filter and was used for analytical characterization and to build photodetector devices using spin coating technique.

NMR spectroscopy: ^{1}H NMR of the $AgBiS_2$-OA were performed on a Bruker Avance III-HD 400 MHz spectrometer and $AgBiS_2$-MPA in benzylamine and all DOSY measurements were performed on a Bruker Avance III-HD 500 MHz spectrometer. Oleate concentration in this QD sample was estimated using quantitative NMR, where ferrocene was used an internal standard. Since nanocrystal sizing curves are not available in literature for $AgBiS_2$ to calculate QD concentration consequently ligand per dot, we used quantitative NMR to measure total oleate ligand concentration in the system. Ferrocene was used as an internal reference to quantify strongly interacting oleate specie to estimate the secondary ligand concertation to achieve a complete ligand exchange. We estimated oleate concentration ~ 2.9×10^{-5} mole/mL.

Device Fabrication: ITO coated glass substrates with area ~2 cm^2 were cleaned by washing with detergent and then sequentially sonicated in acetone, IPA, ethanol, and dionized water for 5 minutes each before drying by nitrogen flow. Three drops of 5% tetrabutyl *titanate* solution in dry ethanol were spin coated at 4000 rpm. These coated substrates were annealed at 450°C for 30 minutes to form compact TiO_2 films and were used for photodetecting device fabrication without further treatment. 15 µL of $AgBiS_2$-MPA solution was dropped and spread on entire substrate by spinning at 1500 rpm for 30s, the process was repeated to make a ~100 nm thick film. The top Au-contacts were deposited using MDC e-Vap 4000 Electron Beam Evaporation System with a base pressure 1×10^{-6} torr through a shadow mask. The shadow mask also defines the active area of the devices. Au metal was deposited at a rate of 2Å/s to get a final metal thickness of 100nm. Similarly, conductive $AgBiS_2$ QD films were fabricated onto a prepatterned SiO_2-coated silicon substrates and PET flexible substrates by spinning 15 uL QD solution and repeating

the process 4 times to yiel a ~100nm think film for lateral devices. While spin coating and annealing were conducted under nitrogen, all electronic measurements were done at room temperature and under ambient atmosphere.

CHAPTER 6

PROBING GROWTH INTERFACE DEFECTS AND CONDUCTION MECHANISM IN AlGaN/GaN HEMT DEVICES USING SCANNING PHOTOCURRENT MICROSCOPY

6.1 INTRODUCTION

III-nitride semiconductor materials (Al, In, Ga)N, that provide good charge mobility, high breakdown electric field, and excellent thermal conductivity, have been explored for their applications in high-frequency, high power, and high-temperature power electronics. The GaN based High electron mobility transistors (HEMTs) are currently taking over consumer power electronics such as laptop and mobile chargers converting 110 V AC power to 19 or 6 V DC, smart solar inverter and compact power switches for electric vehicles, 5G switches, and nuclear powerplant applications[147–150]. The tunable wide bandgap AlxGa1-xN (AlGaN) alloys (<300nm for ~40% Al) also enables them for true solar blind photodetection devices with potential applications in secure space communications, highly sensitive missile plume detectors, flame detectors, and ozone monitoring systems[151,152]. These devices are compatible with monolithic integration, and with sufficiently low dark current, these are suitable for low noise, fast, and compact photodetector operating at large bandwidth[153,154]. These advantages are all expected to improve with scaling from GaN to Al-rich AlGaN alloys due to their increased ultra-wide bandgap (UWBG).

The UWBG provides for low leakage, high power handling and improved thermal management in a small footprint.

Despite these advantages, AlGaN/GaN based HEMT devices are limited by electrically active defects leading to slow response times >100s, often accompanied by persistent photocurrent (PPC)[155,156]. These could lead to catastrophic degradation in applications, such as in class D amplifiers and power switches[150,157,158]. These deep-level defects lead not only to slow speeds but also contribute towards a large unwanted sub-bandgap photoresponse[159]. These defects are associated with the surface, material, and/or interface states, especially in the barrier layer and back interfaces[160,161]. it is generally recognized that both, extended 1D threading dislocations and point defects are challenging the material's application. The extended defects arise from epitaxial growth of GaN on non-native substrates, induce premature breakdown and limit peak electric field strength[162,163]. Point defects arise from strain and atomic vacancies from growth, act as electron/hole trap centers, delaying the escape of charge carriers thereby increasing the response time[164,165]. Collectively, these sub-bandgap defects result in visible light sensitivity, loss of gate control, frequency dispersion, current collapse, and shift in threshold voltages[151]. While these defects influence the on-state performance, they more severely impact the off-state performance. Low levels of defects can cause large amounts of leakage, and speed limiting in switching applications, where nanosecond rise times are required to exceed the performance of silicon based devices[166,167].

The physical mechanisms underlying how sub-bandgap defects in III-N influence a device’s performance is important to understand and predict the behavior and failure mechanism of these devices. Given the geometry of these devices, neither capacitance

measurements nor current-based techniques have the spatial resolution to isolate the influence of these sub-bandgap defects.

Here we show that Scanning photocurrent microscopy (SPCM) with visible excitation (443nm) can spectrally isolate and image these sub-bandgap defects **Figure 6.1c**. We established that, it is possible to spatially resolve electrically active traps using gate dependent SPCM analysis. The technique also enables us to study current conduction mechanisms in AlGaN/GaN devices in different operating regimes through polarity resolved SPCM measurements. Based on our SPCM results, we hypothesize that traps at the back interface in these device structures worked as a parallel conduction path along with the two dimensional electron gas (2DEG) channel **Fig-6.2c**.

SPCM is a nondestructive and ideal technique to characterize photoelectrical properties of light-sensitive devices. It has been used to study junction behavior, electronic band structures of metal-semiconductor contacts, and defects in a variety of materials[168,169]. Recently we have extended this technique to two-dimensional material systems based on graphene to report defect analysis and junction behavior in a hybrid quantum dot graphene device[67,170,171]. This technique uses a diffraction-limited, focused light beam to locally excite a semiconductor into non-equilibrium, generating electron-hole pairs. If these injected charge carriers can reach the nearby electrodes before recombination, a photocurrent signal is observed. This photocurrent is recorded simultaneously with the light signal reflected from the sample as a function of position to create a 2D photocurrent map that is spatially registered to the device layout. The incident light beam is chopped, resulting in AC photocurrent signal that is detected with a lock-in amplifier, locked at the

laser frequency, recording only photocurrent, rejecting dark and DC components, enabling us to measure small photocurrent responses on top of a large dark current.

6.2 RESULTS AND DISCUSSION

A schematic of the device is shown in **Figure 6.1a**. The AlGaN/GaN HEMT was grown on a single side polished sapphire substrate. Metal-organic chemical vapor deposition (MOCVD) technique was used to fabricate 3µm *AlN* template, 3µm *GaN* channel, 1.5nm *AlN spacer*, and 30nm $Al_{0.28}Ga_{0.72}N$ delta-doped barrier. Photolithography and e-beam metal evaporation techniques were used to pattern and deposit TiAl/TiAu (thickness: 110/130nm), source and drain electrodes that were subsequently annealed to form ohmic contacts with the 2DEG and were capped with *NiAu* contact pads. A Ni/Au schottky gate electrode was defined and deposited by a similar process without annealing.

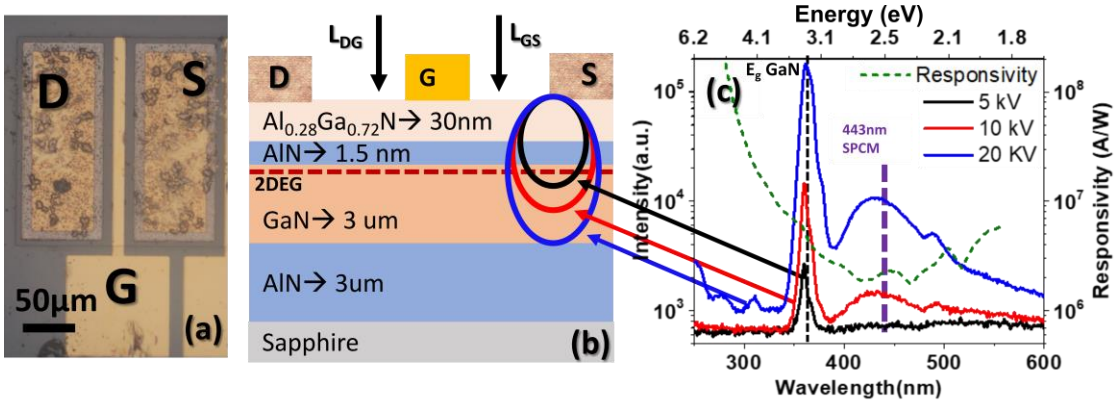

Figure 6.1: *(a) optical micrograph of HEMT device (b) schematic diagram of AlGaN/GaN L_{DG} & L_{GS} represents access region (channel between drain-gate and gate-source electrodes), these are not covered with any contact metals, ovels indicating beam penetration depth of incident electrons for cathodoluminescence measurements (c) cathodoluminescence spectrum indicating sub-bandgap emission and responsivity action spectrum*

This final device was 20μm between source and drain, and 10μm wide gate leaving access regions L_{DG} and L_{GS} with length of ~5μm each **Figure 6.1b**. This HEMT device exhibited a characteristic *n*-channel (Ns = 1.2×10^{13} cm^{-2}) FET transconductance with an on/off ratio of 2.1×10^{4} and a pinch-off at ~10.2V **Figure 6.2a**.

These structures were characterized using luminescence and photoresponsivity techniques that provide qualitative and quantitative information about growth defects[155]. These techniques can provide beam energy dependent (penetration depth increase with increased beam energy) vertical spatial information. From the cathodoluminescence (CL) spectrum **Figure 6.1c**, it is evident that sub-bandgap defects in GaN, as well as at the AlN/GaN interface are responsible for the broad defect shoulder centered around 440nm, as reported before in literature[155]. To spectrally isolate this defect signature, a sub-bandgap 443nm laser was chosen to probe these optically active growth defects using SPCM. The choice of this sub-bandgap wavelength corresponds to ~100x lower photoresponsivity (A/W) compared to above-bandgap region. This 100x fall-off is much weaker than the $>10^{4}$ expected for GaN due to its direct bandgap indicating the strong role of sub-bandgap defects[172].

To demonstrate the significant sub-threshold photoresponse required for SPCM, steady state, spot I-V measurements under 443nm sub-bandgap illumination were performed **Figure 6.2a**. A significant photocurrent in the output characteristics leading to responsivities as high as 2.1×10^{5}A/W (**Figure 6.1c**) or external quantum efficiencies > 10^{4} was observed. The transfer characteristics showed a 0.6V shift in threshold voltage (V_{th}) under illumination, corresponding to a photogenerated sheet carrier (Ns) density increase of $7\times10^{11}cm^{-2}$ or ~6%.

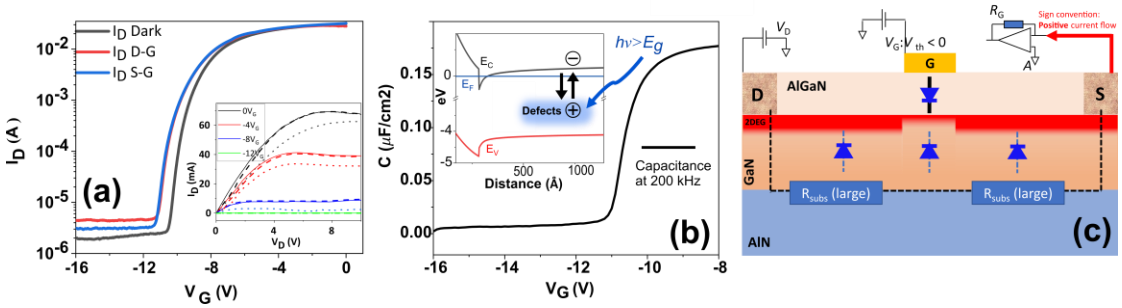

Figure 6.2: *(a) Transfer curves under L_{DG} and L_{SG} side illumination, inset shows output characteristics (b) C-V curve, inset shows band diagram (c) Proposed parallel conduction path at back interface underneath the 2DEG*

This shift was persistent for wide area and spot I-Vs on ***L_{DG}*** and ***L_{SG}*** regions. The large increase in photocurrent for the relatively small increase in Ns is due to photoconductive gain, also known as persistent photocurrent (PPC), commonly observed in III-N devices [173,172]. This PPC is often ascribed purely to the channel arising from bare surfaces and sub-optimal interfaces. The physics responsible for these leakage pathways are incorporated in GaN device circuit models and the gate leakage is ignored as it is typically a small component of overall leakage above V_{th} in the on-state.

In this study, we demonstrate experimentally that an additional leakage mechanism through the gate/source diode is required to completely describe sub-threshold non-idealities. Given that the activation energies for the Schottky gate are likely different from that of the bulk GaN channel layer, as well as from that at the AlN/GaN interface (band diagram, **Figure 6.2b**) this is critical for developing temperature dependent circuit models in GaN devices for near term applications in power amplification. This becomes even more important in emerging UWBG AlGaN devices, which are pseudomorphic to the AlN templates, presenting a very different interface than the AlN/GaN.

This is the first study in AlGaN/GaN HEMTS, reporting the observation of photocurrent due to sub-bandgap response, and not the thermal current as reported previously[174]. We ruled out any significant contribution from thermal photocurrent on the basis that photocurrent signals are centered in the access regions and there are is no appreciable photocurrent under the contacts because they are opaque to incident light[174].

We use V_G dependence of SPCM to vertically profile sub-bandgap photocurrent, while the spatial distribution around contacts is monitored using the ~1um spot size in our SPCM. A V_{DS} dependence allows pinch-off near the drain to also be imaged above V_{th} as the device is biased from triode region into saturation **Figure 6.3b**. Considering the slow photoresponse (39 ms) of the device **Figure 6.6b** we chose a chopping frequency of 27Hz for SPCM and "X" (in-phase) & "Y" (out of phase) current components were recorded and mapped separately to better understand the direction of flow of current. That is different from commonly used wide-area illumination experiments for photoresponse. As a result, we have identified a parallel conduction pathway that is present at the back interface, underneath the 2DEG's active channel. These defects can manifest in the drain-source channel, as well as the gate-source diode.

We fixed the V_{DS} at 2V, which is small enough to ensure both mechanisms to be there, without pinching-off drain end too severely and scanned the gate in three distinct operating regimes, above threshold ($V_G >> V_{th}$), near subthreshold ($V_G \sim V_{th}$), and deep sub threshold ($V_G << V_{th}$).

In the first set of measurements, we observed that when $V_{GS} >> V_{th}$, there is no noticeable photocurrent and conduction is dominated by the highly conductive 2DEG channel. In this

state, any contribution from photogenerated charge carriers is overwhelmed by the channel's very high conductivity **Figure 6.3**.

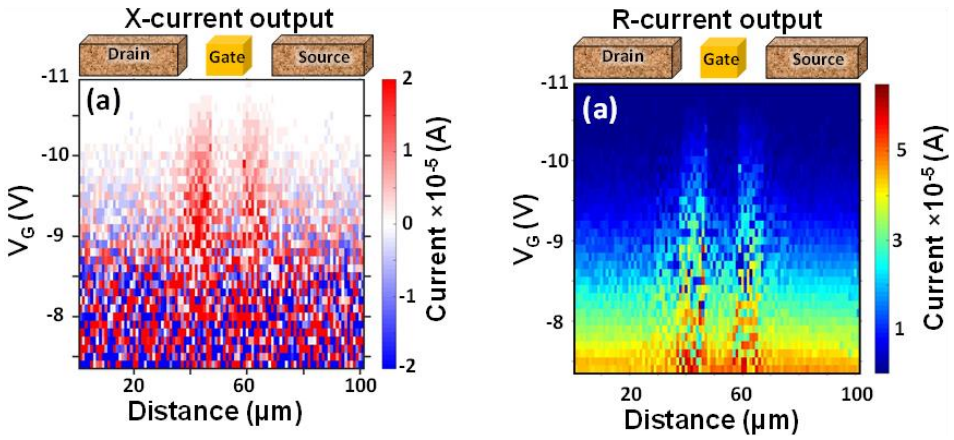

Figure 6.3: *Gate sweep SPCM at fixed $2V_{SD}$ (a) In phase photocurrent map (a) Total photocurrent current (magnitude) map*

In second set of measurement: the gate was scanned just below V_{th}. As we started to approach near V_{th}, photocurrent signals started to appear in access regions that we attributed to photo gain. It was observed that, when scanned around the threshold voltage, the in-phase component of photocurrent switched directions from positive to negative and started to flow in opposite direction in $\boldsymbol{L_{DG}}$ and $\boldsymbol{L_{SG}}$ access regions indicating two different conduction mechanisms appear at different drain-gate bias combinations **Figure 6.4a**.

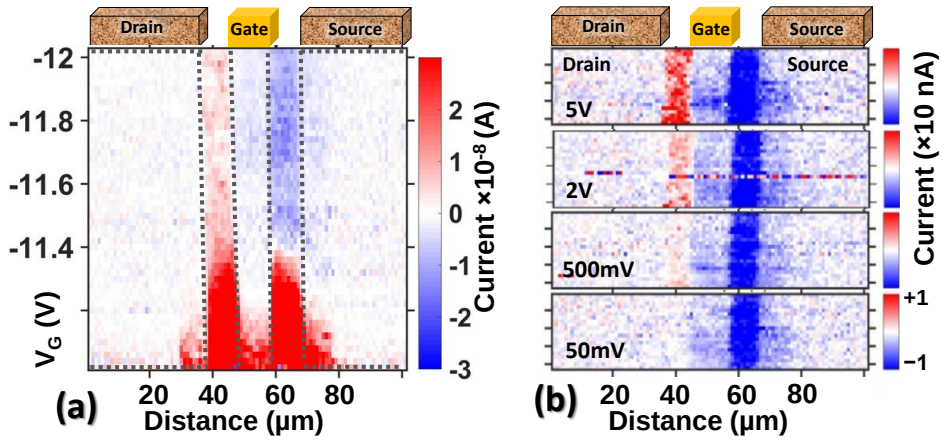

Figure 6.4: *In phase photocurrent maps (a) Gate sweep SPCM at fixed $2V_{SD}$ (b) Drain voltage sweep SPCM at fixed V_G = -12V*

In near-threshold regime, on exciting on $\boldsymbol{L_{DG}}$ and $\boldsymbol{L_{SG}}$ side, the observed photocurrent is positive (forward current increases when light intensity increases). This positive photocurrent is due to the ionization of the traps at the back interface that enables electron injection into the 2DEG channel, effectively shifting its threshold **Figure 6.5a**. The de-trapped electron from the defects has to re-trap thermally upon removal of illumination (**Figure 6.2b**, band diagram), leading to a slow transient **Figure 6.6b**, thereby resulting in the large photoconductive gain and corresponding high responsivity 2×10^5A/W **Figure 6.1c.** This is the classic PPC identified previously[173].

In the second case, just below threshold ($V_G = -12V < V_{th}$), on exciting on $\boldsymbol{L_{DG}}$ side, drain potential is enough to pull the photogenerated electrons. The positive charges left behind by trap ionization are eventually neutralized by the electron flow through the back interface, the overall result being a positive photocurrent (indicated by red color) observed at the source **Figure 6.5bx**. While we excite on the $\boldsymbol{L_{SG}}$ side, drain's potential is insufficient to catch generated electrons and positive charges are quickly neutralized by gate leakage

current and electrons then make their way to source as shown in Fig-4bx, giving a negative photocurrent signal on the SPCM map at L_{SG} side **Figure 6.5by**.

In third case: further going in the deep sub-threshold regime we, see that negative photocurrent in L_{DG} channel as well which can be explained by if there is conduction and electron collection through this back interface **Figure 6.5c**. All electron conduction in the channel is shut down by further depletion of 2DEG. The back interface charges up under illumination changing the Ns in channel. Electron in channel recirculates until the original carrier re-traps thermally back to the charged trap at interface.

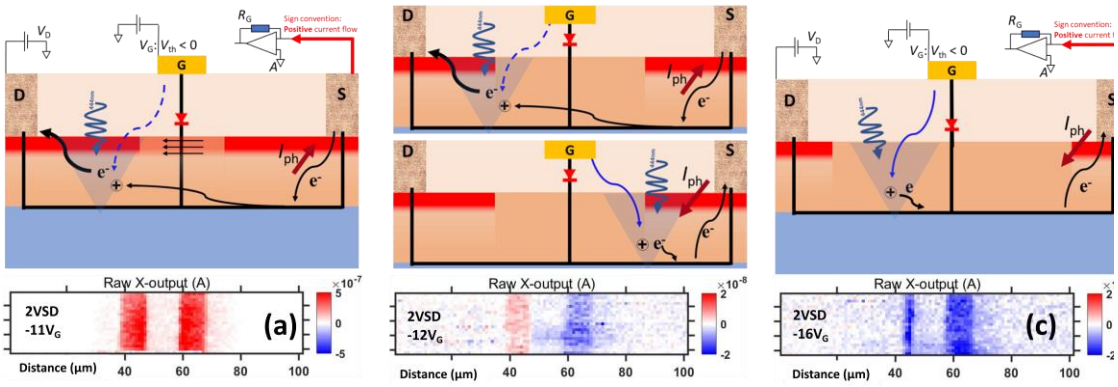

Figure 6.5: *From top to bottom schematic of charge separation, current flow under illumination, and resulting SPCM's in-phase output measured at source electrode at 2VSD, -11VG (b) 2VSD, -12VG, "bx" indicates and illumination on L_{SG} side and "by"*

The photo generated positively charged defects left behind by de-trapped electrons are then fulfilled by the gate's leakage current giving a negative photocurrent signal on the SPCM map on both L_{DG} and L_{SG} channels.

The depletion of 2DEG, and trap assisted conduction mechanism is further supported by drain voltage sweep **Figure 6.4b**, in which drain voltages were increased from low (50mV) to high (5V) at the fixed gate $-12V_G$. Results indicate that if a large enough drain bias is applied, one can have collection of photogenerated carriers at the drain-side channel as well which is not visible for near-zero drain voltages. That means relative contribution from gate and drain varies depending upon the applied bias conditions. Also, a controlled experiment with shorted and floating drain confirms the collection at gate schottky junction **Figure 6.6a**. At low/zero drain-source voltage, with the 2DEG channel firmly switched off with $V_G < V_{th}$, only the buried path plays a role in conduction.

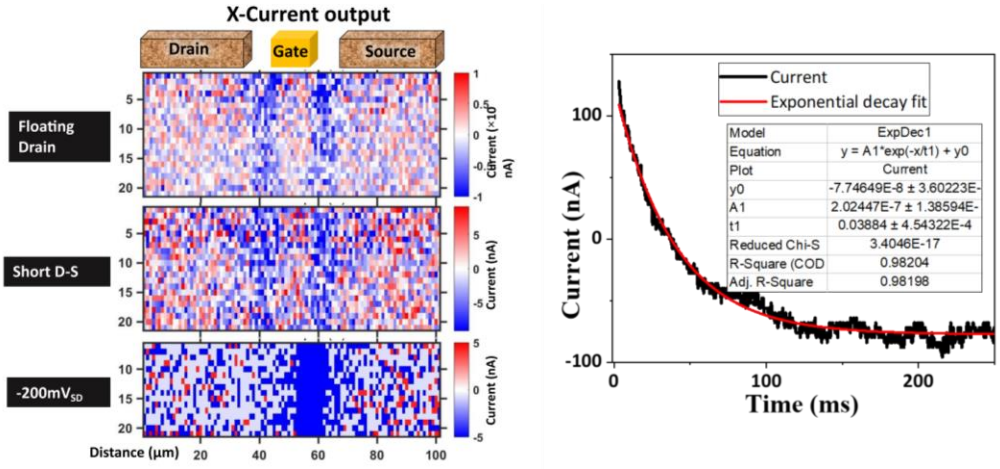

Figure 6.6: (a) In phase photocurrent map of controlled SPCM experiment with drain floating, short to ground and -200mV bias (a) lifetime measurement under sub-threshold condition (-12VG) and sub-bandgap (444nm) illumination

The direction of the photocurrent on each side corresponds to what one might expect for charge separation between the semi-insulating GaN layer and the n-type channel. But, as the gate voltage approaches the threshold, some of the electrons generated at this buried junction make their way into the channel, which has high mobility and gives a positive current, for positive drain-source voltages. At large negative gate bias, $V_G << V_{th}$, the gate

Schottky collection contributes significantly and dominates the current collection on both sides of the gate.

6.3 CONCLUSION

In conclusion, for the first time, we show that charge collection at the gate-source Schottky junction, as well as photoconductive gain due to drain-source channel modulation by sub-bandgap light that can be distinguished for AlGaN/GaN HEMT device. We also show that by varying the gate voltage to tune the channel carrier density, the sub-bandgap response is significantly reduced in the on-state, demonstrating the use of SPCM for diagnosing device-limiting deep defects in the III-nitrides. Our results from floating/short Drain based SPCM indicates photo-induced charge carrier generation is deep in GaN structure and the charge collection at the gate is responsible for the opposite sign of current collected at lead-in regions. These results will enable more robust device designs by spatially isolating these defects.

REFERENCES

(1) Climate Change: Annual greenhouse gas index | NOAA Climate.gov https://www.climate.gov/news-features/understanding-climate/climate-change-annual-greenhouse-gas-index (accessed 2021 -09 -07).

(2) EIA projects nearly 50% increase in world energy usage by 2050, led by growth in Asia - Today in Energy - U.S. Energy Information Administration (EIA) https://www.eia.gov/todayinenergy/detail.php?id=41433 (accessed 2021 -09 -07).

(3) Kagan, C. R.; Murray, C. B. Charge Transport in Strongly Coupled Quantum Dot Solids. *Nat. Nanotechnol.* **2015**, *10* (12), 1013. https://doi.org/10.1038/nnano.2015.247.

(4) Kagan, C. R.; Lifshitz, E.; Sargent, E. H.; Talapin, D. V. Building Devices from Colloidal Quantum Dots. *Science* **2016**, *353* (6302). https://doi.org/10.1126/science.aac5523.

(5) Sahu, A.; Garg, A.; Dixit, A. A Review on Quantum Dot Sensitized Solar Cells: Past, Present and Future towards Carrier Multiplication with a Possibility for Higher Efficiency. *Sol. Energy* **2020**, *203*, 210–239. https://doi.org/10.1016/j.solener.2020.04.044.

(6) Liu, M.; Yazdani, N.; Yarema, M.; Jansen, M.; Wood, V.; Sargent, E. H. Colloidal Quantum Dot Electronics. *Nat. Electron.* **2021**, 1–11. https://doi.org/10.1038/s41928-021-00632-7.

(7) Lee, H.; Song, H.-J.; Shim, M.; Lee, C. Towards the Commercialization of Colloidal Quantum Dot Solar Cells: Perspectives on Device Structures and Manufacturing. *Energy Environ. Sci.* **2020**, *13* (2), 404–431. https://doi.org/10.1039/C9EE03348C.

(8) Tang, J.; Sargent, E. H. Infrared Colloidal Quantum Dots for Photovoltaics: Fundamentals and Recent Progress. *Adv. Mater.* **2011**, *23* (1), 12–29. https://doi.org/10.1002/adma.201001491.

(9) Moreels, I.; Lambert, K.; Smeets, D.; De Muynck, D.; Nollet, T.; Martins, J. C.; Vanhaecke, F.; Vantomme, A.; Delerue, C.; Allan, G. Size-Dependent Optical Properties of Colloidal PbS Quantum Dots. *ACS Nano* **2009**, *3* (10), 3023–3030. https://doi.org/10.1021/nn900863a.

(10) De Vos, A. Detailed Balance Limit of the Efficiency of Tandem Solar Cells. *J. Phys. Appl. Phys.* **1980**, *13* (5), 839.

(11) García de Arquer, F. P.; Talapin, D. V.; Klimov, V. I.; Arakawa, Y.; Bayer, M.; Sargent, E. H. Semiconductor Quantum Dots: Technological Progress and Future Challenges. *Science* **2021**, *373* (6555), eaaz8541. https://doi.org/10.1126/science.aaz8541.

(12) Giansante, C. Surface Chemistry Control of Colloidal Quantum Dot Band Gap. *J. Phys. Chem. C* **2018**, *122* (31), 18110–18116. https://doi.org/10.1021/acs.jpcc.8b05124.

(13) Song, J. H.; Jeong, S. Colloidal Quantum Dot Based Solar Cells: From Materials to Devices. *Nano Converg.* **2017**, *4* (1), 21. https://doi.org/10.1186/s40580-017-0115-0.
(14) Nugraha, M. I. Charge Transport and Trap States in Lead Sulfide Quantum Dot Field-Effect Transistors, Ph. D. Dissertation, University of Groningen, 2017. https://research.rug.nl/en/publications/charge-transport-and-trap-states-in-lead-sulfide-quantum-dot-fiel (accessed 2021-09-10).
(15) Brus, L. E. Electron–Electron and Electron-Hole Interactions in Small Semiconductor Crystallites: The Size Dependence of the Lowest Excited Electronic State. *J. Chem. Phys.* **1984**, *80* (9), 4403–4409. https://doi.org/10.1063/1.447218
(16) Ahmed, F.; Kelley, M. L.; Chandrashekhar, M.; Greytak, A. B. Improved Charge Transport in PbS Quantum Dot Thin Films Following Gel Permeation Chromatography Purification. *J. Phys. Chem. C* **2021**. https://doi.org/10.1021/acs.jpcc.1c04218.
(17) Bae, S. Y.; Oh, J. T.; Park, J. Y.; Ha, S. R.; Choi, J.; Choi, H.; Kim, Y. Improved Eco-Friendly Photovoltaics Based on Stabilized AgBiS2 Nanocrystal Inks. *Chem. Mater.* **2020**, *32* (23), 10007–10014. https://doi.org/10.1021/acs.chemmater.0c03126.
(18) Kelley, M. L.; Ahmed, F.; Abiodun, S. L.; Usman, M.; Jewel, M. U.; Hussain, K.; zur Loye, H.-C.; Chandrashekhar, M. V. S.; Greytak, A. B. Photoconductive Thin Films Composed of Environmentally Benign AgBiS2 Nanocrystal Inks Obtained through a Rapid Phase Transfer Process. *ACS Appl. Electron. Mater.* **2021**, *3* (4), 1550–1555. https://doi.org/10.1021/acsaelm.0c01107.
(19) Hetsch, F.; Zhao, N.; Kershaw, S. V.; Rogach, A. L. Quantum Dot Field Effect Transistors. *Mater. Today* **2013**, *16* (9), 312–325. https://doi.org/10.1016/j.mattod.2013.08.011.
(20) Li, Z.; Zhao, X.; Huang, C.; Gong, X. Recent Advances in Green Fabrication of Luminescent Solar Concentrators Using Nontoxic Quantum Dots as Fluorophores. *J. Mater. Chem. C* **2019**, *7* (40), 12373–12387. https://doi.org/10.1039/C9TC03520F.
(21) Tang, X.; Ackerman, M. M.; Guyot-Sionnest, P. Colloidal Quantum Dots Based Infrared Electronic Eyes for Multispectral Imaging; International Society for Optics and Photonics, 2019; Vol. 11088, p 1108803. https://doi.org/10.1117/12.2528595.
(22) Abib, M. H.; Yao, X.; Li, G.; Mi, L.; Chang, Y.; Wang, H.; Yu, D.; Jiang, Y. Simulation-Based Optical Spectra Analyses and Synthesis of Highly Monodispersed Mn-Doped ZnSe Nanocrystal. *Nano* **2016**, *11* (8), 1650086. https://doi.org/10.1142/S1793292016500867.
(23) Zhang, J.; Crisp, R. W.; Gao, J.; Kroupa, D. M.; Beard, M. C.; Luther, J. M. Synthetic Conditions for High-Accuracy Size Control of PbS Quantum Dots. *J. Phys. Chem. Lett.* **2015**, *6* (10), 1830–1833. https://doi.org/10.1021/acs.jpclett.5b00689.
(24) Murray, C. B.; Kagan, a C.; Bawendi, M. Synthesis and Characterization of Monodisperse Nanocrystals and Close-Packed Nanocrystal Assemblies. *Annu.*

Rev. Mater. Sci. **2000**, *30* (1), 545–610. https://doi.org/10.1146/annurev.matsci.30.1.545.

(25) Ahmed, F.; Kelley, M. L.; Chandrashekhar, M.; Greytak, A. B. Improved Charge Transport in PbS Quantum Dot Thin Films Following Gel Permeation Chromatography Purification. *J. Phys. Chem. C* **2021**. https://doi.org/10.1021/acs.jpcc.1c04218.

(26) Shen, Y.; Gee, M. Y.; Tan, R.; Pellechia, P. J.; Greytak, A. B. Purification of Quantum Dots by Gel Permeation Chromatography and the Effect of Excess Ligands on Shell Growth and Ligand Exchange. *Chem. Mater.* **2013**, *25* (14), 2838–2848. https://doi.org/10.1021/cm4012734.

(27) Roberge, A.; Dunlap, J. H.; Ahmed, F.; Greytak, A. B. Size-Dependent PbS Quantum Dot Surface Chemistry Investigated via Gel Permeation Chromatography. *Chem. Mater.* **2020**, *32* (15), 6588–6594. https://doi.org/10.1021/acs.chemmater.0c02024.

(28) Roberge, A.; Stein, J. L.; Shen, Y.; Cossairt, B. M.; Greytak, A. B. Purification and in Situ Ligand Exchange of Metal-Carboxylate-Treated Fluorescent InP Quantum Dots via Gel Permeation Chromatography. *J. Phys. Chem. Lett.* **2017**, *8* (17), 4055–4060. https://doi.org/10.1021/acs.jpclett.7b01772.

(29) Abiodun, S. L.; Pellechia, P. J.; Greytak, A. B. Effective Purification of CsPbBr3 Nanocrystals with High Quantum Yield and High Colloidal Stability via Gel Permeation Chromatography. *J. Phys. Chem. C* **2021**, *125* (6), 3463–3471. https://doi.org/10.1021/acs.jpcc.1c00207.

(30) Dunlap, J. H.; Loszko, A. F.; Flake, R. A.; Huang, Y.; Benicewicz, B. C.; Greytak, A. B. Multiply-Binding Polymeric Imidazole Ligands: Influence of Molecular Weight and Monomer Sequence on Colloidal Quantum Dot Stability. *J. Phys. Chem. C* **2018**, *122* (46), 26756–26763. https://doi.org/10.1021/acs.jpcc.8b08984.

(31) Balazs, D. M.; Loi, M. A. Lead-Chalcogenide Colloidal-Quantum-Dot Solids: Novel Assembly Methods, Electronic Structure Control, and Application Prospects. *Adv. Mater.* **2018**, *30* (33), 1800082. https://doi.org/10.1002/adma.201800082.

(32) Choi, J.-H.; Fafarman, A. T.; Oh, S. J.; Ko, D.-K.; Kim, D. K.; Diroll, B. T.; Muramoto, S.; Gillen, J. G.; Murray, C. B.; Kagan, C. R. Bandlike Transport in Strongly Coupled and Doped Quantum Dot Solids: A Route to High-Performance Thin-Film Electronics. *Nano Lett.* **2012**, *12* (5), 2631–2638. https://doi.org/10.1021/nl301104z.

(33) Kirmani, A. R. Commercializing Colloidal Quantum Dot Photovoltaics. *MRS Bull.* **2019**, *44* (7), 524–525. https://doi.org/10.1557/mrs.2019.163.

(34) Ahmed, F.; Dunlap, J. H.; Pellechia, P. J.; Greytak, A. B. A P-Type PbS Quantum Dot Ink with Improved Stability for Solution Processable Optoelectronics. *Chem. Commun.* **2021**, *57* (65), 8091–8094. https://doi.org/10.1039/D1CC03014K.

(35) Gilmore, R. H.; Lee, E. M. Y.; Weidman, M. C.; Willard, A. P.; Tisdale, W. A. Charge Carrier Hopping Dynamics in Homogeneously Broadened PbS Quantum Dot Solids. *Nano Lett.* **2017**, *17* (2), 893–901. https://doi.org/10.1021/acs.nanolett.6b04201.

(36) Whitham, K.; Yang, J.; Savitzky, B. H.; Kourkoutis, L. F.; Wise, F.; Hanrath, T. Charge Transport and Localization in Atomically Coherent Quantum Dot Solids. *Nat. Mater.* **2016**, *15* (5), 557–563. https://doi.org/10.1038/nmat4576.

(37) Houtepen, A. J.; Hens, Z.; Owen, J. S.; Infante, I. On the Origin of Surface Traps in Colloidal II–VI Semiconductor Nanocrystals. *Chem. Mater.* **2017**, *29* (2), 752–761. https://doi.org/10.1021/acs.chemmater.6b04648.

(38) Giansante, C.; Infante, I. Surface Traps in Colloidal Quantum Dots: A Combined Experimental and Theoretical Perspective. *J. Phys. Chem. Lett.* **2017**, *8* (20), 5209–5215. https://doi.org/10.1021/acs.jpclett.7b02193.

(39) Reeves, G.; Harrison, H. Obtaining the Specific Contact Resistance from Transmission Line Model Measurements. *IEEE Electron Device Lett.* **1982**, *3* (5), 111–113. https://doi.org/10.1109/EDL.1982.25502.

(40) Singh, J. *Optoelectronics: An Introduction to Materials and Devices*; McGraw-Hill College, 1996.

(41) Bederak, D.; Balazs, D. M.; Sukharevska, N. V.; Shulga, A. G.; Abdu-Aguye, M.; Dirin, D. N.; Kovalenko, M. V.; Loi, M. A. Comparing Halide Ligands in PbS Colloidal Quantum Dots for Field-Effect Transistors and Solar Cells. *ACS Appl. Nano Mater.* **2018**, *1* (12), 6882–6889. https://doi.org/10.1021/acsanm.8b01696.

(42) Otto, T.; Miller, C.; Tolentino, J.; Liu, Y.; Law, M.; Yu, D. Gate-Dependent Carrier Diffusion Length in Lead Selenide Quantum Dot Field-Effect Transistors. *Nano Lett.* **2013**, *13* (8), 3463–3469. https://doi.org/10.1021/nl401698z.

(43) Kelley, M. L.; Letton, J.; Simin, G.; Ahmed, F.; Love-Baker, C. A.; Greytak, A. B.; Chandrashekhar, M. Photovoltaic and Photoconductive Action Due to PbS Quantum Dots on Graphene/SiC Schottky Diodes from NIR to UV. *ACS Appl. Electron. Mater.* **2019**, *2* (1), 134–139. https://doi.org/10.1021/acsaelm.9b00651.

(44) Strasfeld, D. B.; Dorn, A.; Wanger, D. D.; Bawendi, M. G. Imaging Schottky Barriers and Ohmic Contacts in PbS Quantum Dot Devices. *Nano Lett.* **2012**, *12* (2), 569–575. https://doi.org/10.1021/nl204116b.

(45) Park, J. D.; Son, B. H.; Park, J. K.; Kim, S. Y.; Park, J.-Y.; Lee, S.; Ahn, Y. H. Diffusion Length in Nanoporous TiO2 Films under Above-Band-Gap Illumination. *AIP Adv.* **2014**, *4* (6), 067106. https://doi.org/10.1063/1.4881875.

(46) Konstantatos, G.; Sargent, E. H. *Colloidal Quantum Dot Optoelectronics and Photovoltaics*; Cambridge University Press, 2013. https://doi.org/10.1017/CBO9781139022750.

(47) De Iacovo, A.; Venettacci, C.; Colace, L.; Scopa, L.; Foglia, S. PbS Colloidal Quantum Dot Photodetectors Operating in the near Infrared. *Sci. Rep.* **2016**, *6*, 37913. https://doi: 10.1038/srep37913.

(48) Kim, G.-H.; García de Arquer, F. P.; Yoon, Y. J.; Lan, X.; Liu, M.; Voznyy, O.; Yang, Z.; Fan, F.; Ip, A. H.; Kanjanaboos, P. High-Efficiency Colloidal Quantum Dot Photovoltaics via Robust Self-Assembled Monolayers. *Nano Lett.* **2015**, *15* (11), 7691–7696. https://doi.org/10.1021/acs.nanolett.5b03677.

(49) Kagan, C. R.; Lifshitz, E.; Sargent, E. H.; Talapin, D. V. Building Devices from Colloidal Quantum Dots. *Science* **2016**, *353* (6302), aac5523. https://doi.org/10.1126/science.aac5523.

(50) de Arquer, F. P. G.; Armin, A.; Meredith, P.; Sargent, E. H. Solution-Processed Semiconductors for next-Generation Photodetectors. *Nat. Rev. Mater.* **2017**, *2* (3), 16100. https://doi.org/10.1038/natrevmats.2016.100.

(51) Moreels, I.; Justo, Y.; De Geyter, B.; Haustraete, K.; Martins, J. C.; Hens, Z. Size-Tunable, Bright, and Stable PbS Quantum Dots: A Surface Chemistry Study. *ACS Nano* **2011**, *5* (3), 2004–2012. https://doi.org/10.1021/nn103050w.

(52) Ellingson, R. J.; Beard, M. C.; Johnson, J. C.; Yu, P.; Micic, O. I.; Nozik, A. J.; Shabaev, A.; Efros, A. L. Highly Efficient Multiple Exciton Generation in Colloidal PbSe and PbS Quantum Dots. *Nano Lett.* **2005**, *5* (5), 865–871. https://doi.org/10.1021/nl0502672.

(53) Konstantatos, G.; Sargent, E. H. Solution-Processed Quantum Dot Photodetectors. *Proc. IEEE* **2009**, *97* (10), 1666–1683. https://doi.org/10.1109/JPROC.2009.2025612.

(54) Wang, R.; Shang, Y.; Kanjanaboos, P.; Zhou, W.; Ning, Z.; Sargent, E. H. Colloidal Quantum Dot Ligand Engineering for High Performance Solar Cells. *Energy Environ. Sci.* **2016**, *9* (4), 1130–1143. https://doi.org/10.1039/C5EE03887A.

(55) Lin, Q.; Yun, H. J.; Liu, W.; Song, H.-J.; Makarov, N. S.; Isaienko, O.; Nakotte, T.; Chen, G.; Luo, H.; Klimov, V. I. Phase-Transfer Ligand Exchange of Lead Chalcogenide Quantum Dots for Direct Deposition of Thick, Highly Conductive Films. *J. Am. Chem. Soc.* **2017**, *139* (19), 6644–6653. https://doi.org/10.1021/jacs.7b01327.

(56) Ip, A. H.; Thon, S. M.; Hoogland, S.; Voznyy, O.; Zhitomirsky, D.; Debnath, R.; Levina, L.; Rollny, L. R.; Carey, G. H.; Fischer, A. Hybrid Passivated Colloidal Quantum Dot Solids. *Nat. Nanotechnol.* **2012**, *7* (9), 577. https://doi.org/10.1038/nnano.2012.127.

(57) Oh, S. J.; Straus, D.; Zhao, T.; Choi, J.-H.; Lee, S.-W.; Gaulding, E.; Murray, C.; Kagan, C. Engineering the Surface Chemistry of Lead Chalcogenide Nanocrystal Solids to Enhance Carrier Mobility and Lifetime in Optoelectronic Devices. *Chem. Commun.* **2017**, *53* (4), 728–731. https://doi.org/10.1039/C6CC07916D.

(58) King, L. A.; Riley, D. J. Importance of QD Purification Procedure on Surface Adsorbance of QDs and Performance of QD Sensitized Photoanodes. *J. Phys. Chem. C* **2012**, *116* (5), 3349–3355. https://doi.org/10.1021/jp210290j.

(59) Sambur, J. B.; Riha, S. C.; Choi, D.; Parkinson, B. Influence of Surface Chemistry on the Binding and Electronic Coupling of CdSe Quantum Dots to Single Crystal TiO2 Surfaces. *Langmuir* **2010**, *26* (7), 4839–4847. https://doi.org/10.1021/la903618x.

(60) Shen, Y.; Tan, R.; Gee, M. Y.; Greytak, A. B. Quantum Yield Regeneration: Influence of Neutral Ligand Binding on Photophysical Properties in Colloidal Core/Shell Quantum Dots. *ACS Nano* **2015**, *9* (3), 3345–3359. https://doi.org/10.1021/acsnano.5b00671.

(61) Shakeri, B.; Meulenberg, R. W. A Closer Look into the Traditional Purification Process of CdSe Semiconductor Quantum Dots. *Langmuir* **2015**, *31* (49), 13433–13440. https://doi.org/10.1021/acs.langmuir.5b03584.

(62) Morris-Cohen, A. J.; Donakowski, M. D.; Knowles, K. E.; Weiss, E. A. The Effect of a Common Purification Procedure on the Chemical Composition of the Surfaces

of CdSe Quantum Dots Synthesized with Trioctylphosphine Oxide. *J. Phys. Chem. C* **2009**, *114* (2), 897–906. https://doi.org/10.1021/jp909492w.

(63) Kim, T.; Kelley, M. L.; Kim, D.; Greytak, A. B.; Jeong, S. Purification of Colloidal Nanocrystals Along the Road to Highly Efficient Photovoltaic Devices. *Int. J. Precis. Eng. Manuf.-Green Technol.* **2020**. https://doi.org/10.1007/s40684-020-00231-5.

(64) Shcherbakov-Wu, W.; Tisdale, W. A. A Time-Domain View of Charge Carriers in Semiconductor Nanocrystal Solids. *Chem. Sci.* **2020**, *11* (20), 5157–5167. https://doi.org/10.1039/C9SC05925C.

(65) Shen, Y.; Gee, M. Y.; Greytak, A. Purification Technologies for Colloidal Nanocrystals. *Chem. Commun.* **2017**, *53* (5), 827–841. https://doi.org/10.1039/C6CC07998A.

(66) Roberge, A.; Dunlap, J. H.; Ahmed, F.; Greytak, A. B. Size-Dependent PbS Quantum Dot Surface Chemistry Investigated via Gel Permeation Chromatography. *Chem. Mater.* **2020**, *32* (15), 6588–6594. https://doi.org/10.1021/acs.chemmater.0c02024.

(67) Kelley, M. L.; Letton, J.; Simin, G.; Ahmed, F.; Love-Baker, C. A.; Greytak, A. B.; Chandrashekhar, M. V. S. Photovoltaic and Photoconductive Action Due to PbS Quantum Dots on Graphene/SiC Schottky Diodes from NIR to UV. *ACS Appl. Electron. Mater.* **2020**, *2* (1), 134–139. https://doi.org/10.1021/acsaelm.9b00651.

(68) Weidman, M. C.; Yager, K. G.; Tisdale, W. A. Interparticle Spacing and Structural Ordering in Superlattice PbS Nanocrystal Solids Undergoing Ligand Exchange. *Chem. Mater.* **2015**, *27* (2), 474–482. https://doi.org/10.1021/cm503626s.

(69) Talapin, D. V.; Lee, J.-S.; Kovalenko, M. V.; Shevchenko, E. V. Prospects of Colloidal Nanocrystals for Electronic and Optoelectronic Applications. *Chem. Rev.* **2010**, *110* (1), 389–458. https://doi.org/10.1021/cr900137k.

(70) Klem, E. J. D.; Shukla, H.; Hinds, S.; MacNeil, D. D.; Levina, L.; Sargent, E. H. Impact of Dithiol Treatment and Air Annealing on the Conductivity, Mobility, and Hole Density in PbS Colloidal Quantum Dot Solids. *Appl. Phys. Lett.* **2008**, *92* (21), 1–4. https://doi.org/10.1063/1.2917800.

(71) Johnston, K. W.; Pattantyus-Abraham, A. G.; Clifford, J. P.; Myrskog, S. H.; Hoogland, S.; Shukla, H.; Klem, E. J. D.; Levina, L.; Sargent, E. H. Efficient Schottky-Quantum-Dot Photovoltaics: The Roles of Depletion, Drift, and Diffusion. *Appl. Phys. Lett.* **2008**, *92* (12), 122111. https://doi.org/10.1063/1.2896295.

(72) Rath, A. K.; Lasanta, T.; Bernechea, M.; Diedenhofen, S. L.; Konstantatos, G. Determination of Carrier Lifetime and Mobility in Colloidal Quantum Dot Films via Impedance Spectroscopy. *Appl. Phys. Lett.* **2014**, *104* (6), 063504. https://doi.org/10.1063/1.4865089.

(73) Kwan Kim, J.; Hoon Song, J.; Choi, H.; Jae Baik, S.; Jeong, S. Space Charge Limited Conduction in Ultrathin PbS Quantum Dot Solid Diodes. *J. Appl. Phys.* **2014**, *115* (5), 054302. https://doi.org/10.1063/1.4863725.

(74) Cao, Y.; Stavrinadis, A.; Lasanta, T.; So, D.; Konstantatos, G. The Role of Surface Passivation for Efficient and Photostable PbS Quantum Dot Solar Cells. *Nat. Energy* **2016**, *1* (4), 1–6. https://doi.org/10.1038/nenergy.2016.35.

(75) Kim, Y.; Cho, S.; Jeong, S.; Ko, D.-H.; Ko, H.; You, N.; Chang, M.; Reichmanis, E.; Park, J.-Y.; Park, S. Y.; Lee, J. S.; Yang, H.; In, I.; Park, B. Competition between Charge Transport and Energy Barrier in Injection-Limited Metal/Quantum Dot Nanocrystal Contacts. *Chem. Mater.* **2014**, *26* (22), 6393–6400. https://doi.org/10.1021/cm502763z.

(76) Lai, Y.; Li, H.; Kim, D. K.; Diroll, B. T.; Murray, C. B.; Kagan, C. R. Low-Frequency (1/f) Noise in Nanocrystal Field-Effect Transistors. *ACS Nano* **2014**, *8* (9), 9664–9672. https://doi.org/10.1021/nn504303b.

(77) Otto, T.; Miller, C.; Tolentino, J.; Liu, Y.; Law, M.; Yu, D. Gate-Dependent Carrier Diffusion Length in Lead Selenide Quantum Dot Field-Effect Transistors. *Nano Lett.* **2013**, *13* (8), 3463–3469. https://doi.org/10.1021/nl401698z.

(78) Zhang, J.; Crisp, R. W.; Gao, J.; Kroupa, D. M.; Beard, M. C.; Luther, J. M. Synthetic Conditions for High-Accuracy Size Control of PbS Quantum Dots. *J. Phys. Chem. Lett.* **2015**, *6* (10), 1830–1833. https://doi.org/10.1021/acs.jpclett.5b00689.

(79) Shen, Y.; Roberge, A.; Tan, R.; Gee, M. Y.; Gary, D. C.; Huang, Y.; Blom, D. A.; Benicewicz, B. C.; Cossairt, B. M.; Greytak, A. B. Gel Permeation Chromatography as a Multifunctional Processor for Nanocrystal Purification and On-Column Ligand Exchange Chemistry. *Chem. Sci.* **2016**, *7* (9), 5671–5679. https://doi.org/10.1039/C6SC01301E.

(80) De Roo, J.; Yazdani, N.; Drijvers, E.; Lauria, A.; Maes, J.; Owen, J. S.; Van Driessche, I.; Niederberger, M.; Wood, V.; Martins, J. C. Probing Solvent–Ligand Interactions in Colloidal Nanocrystals by the NMR Line Broadening. *Chem. Mater.* **2018**, *30* (15), 5485–5492. https://doi.org/10.1021/acs.chemmater.8b02523.

(81) Weir, M. P.; Toolan, D. T. W.; Kilbride, R. C.; Penfold, N. J. W.; Washington, A. L.; King, S. M.; Xiao, J.; Zhang, Z.; Gray, V.; Dowland, S.; Winkel, J.; Greenham, N. C.; Friend, R. H.; Rao, A.; Ryan, A. J.; Jones, R. A. L. Ligand Shell Structure in Lead Sulfide–Oleic Acid Colloidal Quantum Dots Revealed by Small-Angle Scattering. *J. Phys. Chem. Lett.* **2019**, *10* (16), 4713–4719. https://doi.org/10.1021/acs.jpclett.9b01008.

(82) Kessler, M. L.; Dempsey, J. L. Mapping the Topology of PbS Nanocrystals through Displacement Isotherms of Surface-Bound Metal Oleate Complexes. *Chem. Mater.* **2020**, *32* (6), 2561–2571. https://doi.org/10.1021/acs.chemmater.0c00014.

(83) Tang, J.; Kemp, K. W.; Hoogland, S.; Jeong, K. S.; Liu, H.; Levina, L.; Furukawa, M.; Wang, X.; Debnath, R.; Cha, D.; Chou, K. W.; Fischer, A.; Amassian, A.; Asbury, J. B.; Sargent, E. H. Colloidal-Quantum-Dot Photovoltaics Using Atomic-Ligand Passivation. *Nat Mater* **2011**, *10* (10), 765–771. https://doi.org/10.1038/nmat3118.

(84) Kuo, C.-Y.; Su, M.-S.; Ku, C.-S.; Wang, S.-M.; Lee, H.-Y.; Wei, K.-H. Ligands Affect the Crystal Structure and Photovoltaic Performance of Thin Films of PbSe Quantum Dots. *J. Mater. Chem.* **2011**, *21* (31), 11605–11612. https://doi.org/10.1039/C0JM04417B.

(85) Yang, Z.; Fan, J. Z.; Proppe, A. H.; de Arquer, F. P. G.; Rossouw, D.; Voznyy, O.; Lan, X.; Liu, M.; Walters, G.; Quintero-Bermudez, R. Mixed-Quantum-Dot Solar Cells. *Nat. Commun.* **2017**, *8* (1), 1–9. https://doi.org/10.1038/s41467-017-01362-1.

(86) Kirmani, A. R.; Walters, G.; Kim, T.; Sargent, E. H.; Amassian, A. Optimizing Solid-State Ligand Exchange for Colloidal Quantum Dot Optoelectronics: How Much Is Enough? *ACS Appl. Energy Mater.* **2020**, *3* (6), 5385–5392. https://doi.org/10.1021/acsaem.0c00389.

(87) Schroder, D. K. *Semiconductor Material and Device Characterization*; John Wiley & Sons, 2015. https://doi.org/10.1002/0471749095.

(88) Zarghami, M. H.; Liu, Y.; Gibbs, M.; Gebremichael, E.; Webster, C.; Law, M. P-Type PbSe and PbS Quantum Dot Solids Prepared with Short-Chain Acids and Diacids. *ACS Nano* **2010**, *4* (4), 2475–2485. https://doi.org/10.1021/nn100339b.

(89) Chuang, C.-H. M.; Brown, P. R.; Bulović, V.; Bawendi, M. G. Improved Performance and Stability in Quantum Dot Solar Cells through Band Alignment Engineering. *Nat. Mater.* **2014**, *13* (8), 796–801. https://doi.org/10.1038/nmat3984.

(90) Jeong, K. S.; Tang, J.; Liu, H.; Kim, J.; Schaefer, A. W.; Kemp, K.; Levina, L.; Wang, X.; Hoogland, S.; Debnath, R.; Brzozowski, L.; Sargent, E. H.; Asbury, J. B. Enhanced Mobility-Lifetime Products in PbS Colloidal Quantum Dot Photovoltaics. *ACS Nano* **2012**, *6* (1), 89–99. https://doi.org/10.1021/nn2039164.

(91) Tang, J.; Brzozowski, L.; Barkhouse, D. A. R.; Wang, X.; Debnath, R.; Wolowiec, R.; Palmiano, E.; Levina, L.; Pattantyus-Abraham, A. G.; Jamakosmanovic, D.; Sargent, E. H. Quantum Dot Photovoltaics in the Extreme Quantum Confinement Regime: The Surface-Chemical Origins of Exceptional Air- and Light-Stability. *ACS Nano* **2010**, *4* (2), 869–878. https://doi.org/10.1021/nn901564q.

(92) Graham, R.; Yu, D. Scanning Photocurrent Microscopy in Semiconductor Nanostructures. *Mod. Phys. Lett. B* **2013**, *27* (25), 1330018. https://doi.org/10.1142/S0217984913300184.

(93) Barker Jr, B. G.; Chava, V. S. N.; Daniels, K. M.; Chandrashekhar, M. V. S.; Greytak, A. B. Sub-Bandgap Response of Graphene/SiC Schottky Emitter Bipolar Phototransistor Examined by Scanning Photocurrent Microscopy. *2D Mater.* **2017**, *5* (1), 11003. https://doi.org/10.1088/2053-1583/aa90b1.

(94) Sargent, E. H. Colloidal Quantum Dot Solar Cells. *Nat. Photonics* **2012**, *6* (3), 133–135. https://doi.org/10.1038/nphoton.2012.33.

(95) Kim, J.; Ouellette, O.; Voznyy, O.; Wei, M.; Choi, J.; Choi, M.-J.; Jo, J. W.; Baek, S.-W.; Fan, J.; Saidaminov, M. I.; Sun, B.; Li, P.; Nam, D.-H.; Hoogland, S.; Lu, Z.-H.; García de Arquer, F. P.; Sargent, E. H. Butylamine-Catalyzed Synthesis of Nanocrystal Inks Enables Efficient Infrared CQD Solar Cells. *Adv. Mater.* **2018**, *30* (45), 1803830. https://doi.org/10.1002/adma.201803830.

(96) Gao, Y.; Zheng, J.; Chen, W.; Yuan, L.; Teh, Z. L.; Yang, J.; Cui, X.; Conibeer, G.; Patterson, R.; Huang, S. Enhancing PbS Colloidal Quantum Dot Tandem Solar Cell Performance by Graded Band Alignment. *J. Phys. Chem. Lett.* **2019**, *10* (19), 5729–5734. https://doi.org/10.1021/acs.jpclett.9b02423.

(97) Liu, M.; Voznyy, O.; Sabatini, R.; de Arquer, F. P. G.; Munir, R.; Balawi, A. H.; Lan, X.; Fan, F.; Walters, G.; Kirmani, A. R. Hybrid Organic–Inorganic Inks Flatten the Energy Landscape in Colloidal Quantum Dot Solids. *Nat. Mater.* **2017**, *16* (2), 258–263. https://doi.org/10.1038/nmat4800.

(98) Aqoma, H.; Jang, S.-Y. Solid-State-Ligand-Exchange Free Quantum Dot Ink-Based Solar Cells with an Efficiency of 10.9%. *Energy Environ. Sci.* **2018**, *11* (6), 1603–1609. https://doi.org/10.1039/C8EE00278A.

(99) Choi, M.-J.; de Arquer, F. P. G.; Proppe, A. H.; Seifitokaldani, A.; Choi, J.; Kim, J.; Baek, S.-W.; Liu, M.; Sun, B.; Biondi, M. Cascade Surface Modification of Colloidal Quantum Dot Inks Enables Efficient Bulk Homojunction Photovoltaics. *Nat. Commun.* **2020**, *11* (1), 1–9. https://doi.org/10.1038/s41467-019-13437-2.

(100) Tang, J.; Kemp, K. W.; Hoogland, S.; Jeong, K. S.; Liu, H.; Levina, L.; Furukawa, M.; Wang, X.; Debnath, R.; Cha, D. Colloidal-Quantum-Dot Photovoltaics Using Atomic-Ligand Passivation. *Nat. Mater.* **2011**, *10* (10), 765–771. https://doi.org/10.1038/nmat3118.

(101) Ning, Z.; Dong, H.; Zhang, Q.; Voznyy, O.; Sargent, E. H. Solar Cells Based on Inks of N-Type Colloidal Quantum Dots. *ACS Nano* **2014**, *8* (10), 10321–10327. https://doi.org/10.1021/nn503569p.

(102) Zvaigzne, M. A.; Aleksandrov, A. E.; Goltyapin, Y.; Tameev, A. R.; Chistyakov, A. A. Influence of the Surface Ligands on the Optical and Electrical Properties of PbS QD Solids; International Society for Optics and Photonics, 2018; Vol. 10672, p 1067235. https://doi.org/10.1117/12.2306912.

(103) Teh, Z. L.; Hu, L.; Zhang, Z.; Gentle, A. R.; Chen, Z.; Gao, Y.; Yuan, L.; Hu, Y.; Wu, T.; Patterson, R. J.; Huang, S. Enhanced Power Conversion Efficiency via Hybrid Ligand Exchange Treatment of P-Type PbS Quantum Dots. *Acs Appl. Mater. Interfaces* **2020**, *12* (20), 22751–22759. https://doi.org/10.1021/acsami.9b23492.

(104) Jeong, K. S.; Tang, J.; Liu, H.; Kim, J.; Schaefer, A. W.; Kemp, K.; Levina, L.; Wang, X.; Hoogland, S.; Debnath, R. Enhanced Mobility-Lifetime Products in PbS Colloidal Quantum Dot Photovoltaics. *ACS Nano* **2012**, *6* (1), 89–99. https://doi.org/10.1021/nn2039164.

(105) Reinhart, C. C.; Johansson, E. Colloidally Prepared 3-Mercaptopropionic Acid Capped Lead Sulfide Quantum Dots. *Chem. Mater.* **2015**, *27* (21), 7313–7320. https://doi.org/10.1021/acs.chemmater.5b02786.

(106) Gu, M.; Wang, Y.; Yang, F.; Lu, K.; Xue, Y.; Wu, T.; Fang, H.; Zhou, S.; Zhang, Y.; Ling, X. Stable PbS Quantum Dot Ink for Efficient Solar Cells by Solution-Phase Ligand Engineering. *J. Mater. Chem. A* **2019**, *7* (26), 15951–15959. https://doi.org/10.1039/C9TA02393C.

(107) Sliz, R.; Lejay, M.; Fan, J. Z.; Choi, M.-J.; Kinge, S.; Hoogland, S.; Fabritius, T.; García de Arquer, F. P.; Sargent, E. H. Stable Colloidal Quantum Dot Inks Enable Inkjet-Printed High-Sensitivity Infrared Photodetectors. *ACS Nano* **2019**, *13* (10), 11988–11995. https://doi.org/10.1021/acsnano.9b06125.

(108) Bederak, D.; Sukharevska, N.; Kahmann, S.; Abdu-Aguye, M.; Duim, H.; Dirin, D. N.; Kovalenko, M. V.; Portale, G.; Loi, M. A. On the Colloidal Stability of PbS Quantum Dots Capped with Methylammonium Lead Iodide Ligands. *ACS Appl. Mater. Interfaces* **2020**, *12* (47), 52959–52966. https://doi.org/10.1021/acsami.0c16646.

(109) Giansante, C.; Infante, I.; Fabiano, E.; Grisorio, R.; Suranna, G. P.; Gigli, G. "Darker-than-Black" PbS Quantum Dots: Enhancing Optical Absorption of

Colloidal Semiconductor Nanocrystals via Short Conjugated Ligands. *J. Am. Chem. Soc.* **2015**, *137* (5), 1875–1886. https://doi.org/10.1021/ja510739q.

(110) Kiani, A.; Sutherland, B. R.; Kim, Y.; Ouellette, O.; Levina, L.; Walters, G.; Dinh, C.-T.; Liu, M.; Voznyy, O.; Lan, X. Single-Step Colloidal Quantum Dot Films for Infrared Solar Harvesting. *Appl. Phys. Lett.* **2016**, *109* (18), 183105. https://doi.org/10.1063/1.4966217.

(111) Hickey, R. T.; Jedlicka, E.; Pokuri, B. S. S.; Colbert, A. E.; Bedolla-Valdez, Z. I.; Ganapathysubramanian, B.; Ginger, D. S.; Moulé, A. J. Morphological Consequences of Ligand Exchange in Quantum Dot-Polymer Solar Cells. *Org. Electron.* **2018**, *54*, 119–125. https://doi.org/10.1016/j.orgel.2017.12.018.

(112) Hu, L.; Patterson, R. J.; Hu, Y.; Chen, W.; Zhang, Z.; Yuan, L.; Chen, Z.; Conibeer, G. J.; Wang, G.; Huang, S. High Performance PbS Colloidal Quantum Dot Solar Cells by Employing Solution-Processed CdS Thin Films from a Single-Source Precursor as the Electron Transport Layer. *Adv. Funct. Mater.* **2017**, *27* (46), 1703687. https://doi.org/10.1002/adfm.201703687.

(113) Klem, E. J.; Shukla, H.; Hinds, S.; MacNeil, D. D.; Levina, L.; Sargent, E. H. Impact of Dithiol Treatment and Air Annealing on the Conductivity, Mobility, and Hole Density in PbS Colloidal Quantum Dot Solids. *Appl. Phys. Lett.* **2008**, *92* (21), 212105. https://doi.org/10.1063/1.2917800.

(114) Zhang, J.; Crisp, R. W.; Gao, J.; Kroupa, D. M.; Beard, M. C.; Luther, J. M. Synthetic Conditions for High-Accuracy Size Control of PbS Quantum Dots. *J. Phys. Chem. Lett.* **2015**, *6* (10), 1830–1833. https://doi.org/10.1021/acs.jpclett.5b00689.

(115) Moreels, I.; Lambert, K.; Smeets, D.; De Muynck, D.; Nollet, T.; Martins, J. C.; Vanhaecke, F.; Vantomme, A.; Delerue, C.; Allan, G. Size-Dependent Optical Properties of Colloidal PbS Quantum Dots. *ACS Nano* **2009**, *3* (10), 3023–3030. https://doi.org/10.1021/nn900863a.

(116) Hovden, R.; Muller, D. A. Electron Tomography for Functional Nanomaterials. *MRS Bull.* **2020**, *45* (4), 298–304. https://doi.org/10.1557/mrs.2020.87.

(117) Song, J. H.; Choi, H.; Pham, H. T.; Jeong, S. Energy Level Tuned Indium Arsenide Colloidal Quantum Dot Films for Efficient Photovoltaics. *Nat. Commun.* **2018**, *9* (1), 1–9. https://doi.org/10.1038/s41467-018-06399-4.

(118) Talapin, D. V.; Murray, C. B. PbSe Nanocrystal Solids for N-and p-Channel Thin Film Field-Effect Transistors. *Science* **2005**, *310* (5745), 86–89. https://doi.org/10.1126/science.1116703.

(119) Zhitomirsky, D.; Furukawa, M.; Tang, J.; Stadler, P.; Hoogland, S.; Voznyy, O.; Liu, H.; Sargent, E. H. N-type Colloidal-quantum-dot Solids for Photovoltaics. *Adv. Mater.* **2012**, *24* (46), 6181–6185. https://doi.org/10.1002/adma.201202825.

(120) Park, S. M.; Abtahi, A.; Boehm, A. M.; Graham, K. R. Surface Ligands for Methylammonium Lead Iodide Films: Surface Coverage, Energetics, and Photovoltaic Performance. *ACS Energy Lett.* **2020**, *5* (3), 799–806. https://doi.org/10.1021/acsenergylett.0c00054.

(121) Yang, S.; Prendergast, D.; Neaton, J. B. Tuning Semiconductor Band Edge Energies for Solar Photocatalysis via Surface Ligand Passivation. *Nano Lett.* **2012**, *12* (1), 383–388. https://doi.org/10.1021/nl203669k.

(122) Chen, J.; Zheng, S.; Jia, D.; Liu, W.; Andruszkiewicz, A.; Qin, C.; Yu, M.; Liu, J.; Johansson, E. M.; Zhang, X. Regulating Thiol Ligands of P-Type Colloidal Quantum Dots for Efficient Infrared Solar Cells. *ACS Energy Lett.* **2021**, *6* (5), 1970–1979. https://doi.org/10.1021/acsenergylett.1c00475.

(123) Brown, P. R.; Kim, D.; Lunt, R. R.; Zhao, N.; Bawendi, M. G.; Grossman, J. C.; Bulovic, V. Energy Level Modification in Lead Sulfide Quantum Dot Thin Films through Ligand Exchange. *ACS Nano* **2014**, *8* (6), 5863–5872. https://doi.org/10.1021/nn500897c.

(124) Subramanian, V.; Chang, J. B.; de la Fuente Vornbrock, A.; Huang, D. C.; Jagannathan, L.; Liao, F.; Mattis, B.; Molesa, S.; Redinger, D. R.; Soltman, D. Printed Electronics for Low-Cost Electronic Systems: Technology Status and Application Development; IEEE, 2008; pp 17–24. http://dx.doi.org/10.1109/ESSCIRC.2008.4681785.

(125) Nakazawa, T.; Kim, D.; Oshima, Y.; Sato, H.; Park, J.; Kim, H. Synthesis and Application of AgBiS2 and Ag2S Nanoinks for the Production of IR Photodetectors. *ACS Omega* **2021**. https://doi.org/10.1021/acsomega.1c03463.

(126) Sukharevska, N.; Bederak, D.; Goossens, V. M.; Momand, J.; Duim, H.; Dirin, D. N.; Kovalenko, M. V.; Kooi, B. J.; Loi, M. A. Scalable PbS Quantum Dot Solar Cell Production by Blade Coating from Stable Inks. *ACS Appl. Mater. Interfaces* **2021**, *13* (4), 5195–5207. https://doi.org/10.1021/acsami.0c18204.

(127) Oberg, V. A.; Johansson, M. B.; Zhang, X.; Johansson, E. M. Cubic AgBiS2 Colloidal Nanocrystals for Solar Cells. *ACS Appl. Nano Mater.* **2020**, *3* (5), 4014–4024. https://doi.org/10.1021/acsanm.9b02443.

(128) Akgul, M. Z.; Figueroba, A.; Pradhan, S.; Bi, Y.; Konstantatos, G. Low-Cost RoHS Compliant Solution Processed Photovoltaics Enabled by Ambient Condition Synthesis of AgBiS2 Nanocrystals. *ACS Photonics* **2020**, *7* (3), 588–595. https://doi.org/10.1021/acsphotonics.9b01757.

(129) Jun, H. K. Solution-Processed Quantum Dot-Sensitized Solar Cell Based on "Green" Materials. In *Sustainable Materials for Next Generation Energy Devices*; Elsevier, 2021; pp 133–147. https://doi.org/10.1016/B978-0-12-822838-8.09994-4.

(130) Bernechea, M.; Miller, N. C.; Xercavins, G.; So, D.; Stavrinadis, A.; Konstantatos, G. Solution-Processed Solar Cells Based on Environmentally Friendly AgBiS 2 Nanocrystals. *Nat. Photonics* **2016**, *10* (8), 521–525. https://doi.org/10.1038/nphoton.2016.108.

(131) Guin, S. N.; Biswas, K. Cation Disorder and Bond Anharmonicity Optimize the Thermoelectric Properties in Kinetically Stabilized Rocksalt AgBiS2 Nanocrystals. *Chem. Mater.* **2013**, *25* (15), 3225–3231. https://doi.org/10.1021/cm401630d.

(132) Burgués-Ceballos, I.; Wang, Y.; Akgul, M. Z.; Konstantatos, G. Colloidal AgBiS2 Nanocrystals with Reduced Recombination Yield 6.4% Power Conversion Efficiency in Solution-Processed Solar Cells. *Nano Energy* **2020**, *75*, 104961. https://doi.org/10.1016/j.nanoen.2020.104961.

(133) Lai, M.; Lei, T.; Zhang, Y.; Jin, J.; Steele, J. A.; Yang, P. Phase Transition Dynamics in One-Dimensional Halide Perovskite Crystals. *MRS Bull.* **2021**, *46* (4), 310–316. https://doi.org/10.1557/s43577-021-00047-x.

(134) Lin, Q.; Yun, H. J.; Liu, W.; Song, H.-J.; Makarov, N. S.; Isaienko, O.; Nakotte, T.; Chen, G.; Luo, H.; Klimov, V. I.; Pietryga, J. M. Phase-Transfer Ligand Exchange of Lead Chalcogenide Quantum Dots for Direct Deposition of Thick, Highly Conductive Films. *J. Am. Chem. Soc.* **2017**, *139* (19), 6644–6653. https://doi.org/10.1021/jacs.7b01327.

(135) Kagan, C. R.; Murray, C. B. Charge Transport in Strongly Coupled Quantum Dot Solids. *Nat. Nanotechnol.* **2015**, *10*, 1013. https://doi.org/10.1038/nnano.2015.247.

(136) Papagiorgis, P.; Tsokkou, D.; Gahlot, K.; Protesescu, L.; Manoli, A.; Hermerschmidt, F.; Christodoulou, C.; Choulis, S. A.; Kovalenko, M. V.; Othonos, A. Exciton–Ligand Interactions in PbS Quantum Dots Capped with Metal Chalcogenides. *J. Phys. Chem. C* **2020**, *124* (50), 27848–27857. https://doi.org/10.1021/acs.jpcc.0c09790.

(137) Wang, L.; Wang, Y.; Jia, Y.; Liu, X.; Liu, T.; Fu, T.; Li, J.; Weng, B.; Zhang, X.; Liu, Y. Manipulation of Phase-Transfer Ligand-Exchange Dynamics of PbS Quantum Dots for Efficient Infrared Photovoltaics. *J. Phys. Chem. C* **2019**, *123* (50), 30137–30144. https://doi.org/10.1021/acs.jpcc.9b09231.

(138) Yuan, M.; Wang, X.; Chen, X.; He, J.; Li, K.; Song, B.; Hu, H.; Gao, L.; Lan, X.; Chen, C. Phase-Transfer Exchange Lead Chalcogenide Colloidal Quantum Dots: Ink Preparation, Film Assembly, and Solar Cell Construction. *Small* **2021**, 2102340. https://doi.org/10.1002/smll.202102340.

(139) Dai, Q.; Chen, J.; Lu, L.; Tang, J.; Wang, W. PbS Quantum Dots Prepared by Pulsed Laser Deposition for Photovoltaic Applications and Ligand Effects on Device Performance. *Appl. Phys. Lett.* **2013**, *102* (20), 203904. https://doi.org/10.1063/1.4807935.

(140) Maulu, A.; Rodríguez-Cantó, P. J.; Navarro-Arenas, J.; Abargues, R.; Sánchez-Royo, J. F.; García-Calzada, R.; Pastor, J. P. M. Strongly-Coupled PbS QD Solids by Doctor Blading for IR Photodetection. *RSC Adv.* **2016**, *6* (83), 80201–80212. https://doi.org/10.1039/C6RA14782H.

(141) Reinhart, C. C.; Johansson, E. Colloidally Prepared 3-Mercaptopropionic Acid Capped Lead Sulfide Quantum Dots. *Chem. Mater.* **2015**, *27* (21), 7313–7320. https://doi.org/10.1021/acs.chemmater.5b02786.

(142) Hens, Z.; Martins, J. C. A Solution NMR Toolbox for Characterizing the Surface Chemistry of Colloidal Nanocrystals. *Chem. Mater.* **2013**, *25* (8), 1211–1221. https://doi.org/10.1021/cm303361s.

(143) Mak, C. H.; Qian, J.; Rogée, L.; Lai, W. K.; Lau, S. P. Facile Synthesis of AgBiS 2 Nanocrystals for High Responsivity Infrared Detectors. *RSC Adv.* **2018**, *8* (68), 39203–39207. https://doi.org/10.1039/C8RA08509A.

(144) Sliz, R.; Lejay, M.; Fan, J. Z.; Choi, M.-J.; Kinge, S.; Hoogland, S.; Fabritius, T.; García de Arquer, F. P.; Sargent, E. H. Stable Colloidal Quantum Dot Inks Enable Inkjet-Printed High-Sensitivity Infrared Photodetectors. *ACS Nano* **2019**, *13* (10), 11988–11995. https://doi.org/10.1021/acsnano.9b06125.

(145) Zhang, M.; Zhang, F.; Wang, Y.; Zhu, L.; Hu, Y.; Lou, Z.; Hou, Y.; Teng, F. High-Performance Photodiode-Type Photodetectors Based on Polycrystalline Formamidinium Lead Iodide Perovskite Thin Films. *Sci. Rep.* **2018**, *8* (1), 11157. https://doi.org/10.1038/s41598-018-29147-6.

(146) Jiang, L.; Li, Y.; Peng, J.; Cui, L.; Li, R.; Xu, Y.; Li, W.; Li, Y.; Tian, X.; Lin, Q. Solution-Processed AgBiS 2 Photodetectors from Molecular Precursors. *J. Mater. Chem. C* **2020**, *8* (7), 2436–2441. https://doi.org/10.1039/C9TC06499K.

(147) Su, M.; Chen, C.; Rajan, S. Prospects for the Application of GaN Power Devices in Hybrid Electric Vehicle Drive Systems. *Semicond. Sci. Technol.* **2013**, *28* (7), 074012. https://doi.org/10.1088/0268-1242/28/7/074012.

(148) Mishra, U. K.; Parikh, P.; Wu, Y.-F. AlGaN/GaN HEMTs-an Overview of Device Operation and Applications. *Proc. IEEE* **2002**, *90* (6), 1022–1031. https://doi.org/10.1109/JPROC.2002.1021567.

(149) Muhtadi, S.; Hwang, S.; Coleman, A.; Asif, F.; Lunev, A.; Chandrashekhar, M.; Khan, A. High Temperature Operation of N-AlGaN Channel Metal Semiconductor Field Effect Transistors on Low-Defect AlN Templates. *Appl. Phys. Lett.* **2017**, *110* (19), 193501. https://doi.org/10.1063/1.4982656.

(150) Kizilyalli, I. C.; Edwards, A. P.; Aktas, O.; Prunty, T.; Bour, D. Vertical Power Pn Diodes Based on Bulk GaN. *IEEE Trans. Electron Devices* **2014**, *62* (2), 414–422. https://doi.org/10.1109/TED.2014.2360861.

(151) Armstrong, A. M.; Klein, B. A.; Allerman, A. A.; Baca, A. G.; Crawford, M. H.; Podkaminer, J.; Perez, C. R.; Siegal, M. P.; Douglas, E. A.; Abate, V. M. Visible- and Solar-Blind Photodetectors Using AlGaN High Electron Mobility Transistors with a Nanodot-Based Floating Gate. *Photonics Res.* **2019**, *7* (6), B24–B31. https://doi.org/10.1364/PRJ.7.000B24.

(152) Muhtadi, S.; Hwang, S.; Coleman, A.; Asif, F.; Lunev, A.; Chandrashekhar, M.; Khan, A. Selective Area Deposited N-Al0. 5Ga0. 5N Channel Field Effect Transistors with High Solar-Blind Ultraviolet Photo-Responsivity. *Appl. Phys. Lett.* **2017**, *110* (17), 171104. https://doi.org/10.1063/1.4982599.

(153) Muhtadi, S.; Hwang, S. M.; Coleman, A. L.; Lunev, A.; Asif, F.; Chava, V.; Chandrashekhar, M.; Khan, A. High-Speed Solar-Blind UV Photodetectors Using High-Al Content Al0. 64Ga0. 36N/Al0. 34Ga0. 66N Multiple Quantum Wells. *Appl. Phys. Express* **2016**, *10* (1), 011004. https://doi.org/10.7567/APEX.10.011004.

(154) Waltereit, P.; Bronner, W.; Quay, R.; Dammann, M.; Cäsar, M.; Müller, S.; van Raay, F.; Kiefer, R.; Brückner, P.; Kühn, J. GaN-based High-frequency Devices and Circuits: A Fraunhofer Perspective. *Phys. Status Solidi A* **2012**, *209* (3), 491–496. http://dx.doi.org/10.1002/pssa.201100452.

(155) Jewel, M. U.; Alam, M. D.; Mollah, S.; Hussain, K.; Wheeler, V.; Eddy, C.; Gaevski, M.; Simin, G.; Chandrashekhar, M.; Khan, A. Trap Characterization in Ultra-Wide Bandgap Al0. 65Ga0. 4N/Al0. 4Ga0. 6N MOSHFET's with ZrO2 Gate Dielectric Using Optical Response and Cathodoluminescence. *Appl. Phys. Lett.* **2019**, *115* (21), 213502. https://doi.org/10.1063/1.5125776.

(156) Zheng, X.; Feng, S.; Li, X.; Zhang, Y.; Bai, K. Photocurrents in GaN-Based HEMTs: Theoretical Model and Experimental Results. *Appl. Phys. Lett.* **2019**, *115* (21), 213505. https://doi.org/10.1063/1.5128825.

(157) Matthews, C.; Flicker, J.; Kaplar, R.; Van Heukelom, M.; Attcity, S.; Kizilyalli, I.; Aktas, O. Switching Characterization of Vertical GaN PiN Diodes; IEEE, 2016; pp 135–138. https://doi.org/10.1109/WiPDA.2016.7799924.

(158) Jones, E. A.; Wang, F. F.; Costinett, D. Review of Commercial GaN Power Devices and GaN-Based Converter Design Challenges. *IEEE J. Emerg. Sel. Top. Power Electron.* **2016**, *4* (3), 707–719. https://doi.org/10.1109/JESTPE.2016.2582685.
(159) Stanchu, H. V.; Kuchuk, A. V.; Mazur, Y. I.; Li, C.; Lytvyn, P. M.; Schmidbauer, M.; Maidaniuk, Y.; Benamara, M.; Ware, M. E.; Wang, Z. M. Local Strain and Crystalline Defects in GaN/AlGaN/GaN (0001) Heterostructures Induced by Compositionally Graded AlGaN Buried Layers. *Cryst. Growth Des.* **2018**, *19* (1), 200–210. https://doi.org/10.1021/acs.cgd.8b01267.
(160) Barchuk, M.; Motylenko, M.; Schneider, T.; Förste, M.; Röder, C.; Davydok, A.; Lazarev, S.; Schimpf, C.; Wüstefeld, C.; Pätzold, O. Defect-Rich GaN Interlayer Facilitating the Annihilation of Threading Dislocations in Polar GaN Crystals Grown on (0001)-Oriented Sapphire Substrates. *J. Appl. Phys.* **2019**, *126* (8), 085301. https://doi.org/10.1063/1.5092284.
(161) Moroz, V.; Wong, H. Y.; Choi, M.; Braga, N.; Mickevicius, R.; Zhang, Y.; Palacios, T. The Impact of Defects on GaN Device Behavior: Modeling Dislocations, Traps, and Pits. *ECS J. Solid State Sci. Technol.* **2016**, *5* (4), P3142. https://doi.org/10.1149/2.0211604jss.
(162) Christou, A. Reliability Limitations from Crystal Defects in Thick GaN Epitaxial Layers. *Microelectron. Reliab.* **2020**, *114*, 113946. http://dx.doi.org/10.1016/j.microrel.2020.113946.
(163) Shenai, K. Switching Megawatts with Power Transistors. *Electrochem. Soc. Interface* **2013**, *22* (1), 47. https://doi.org/10.1149/2.F05131if.
(164) Yang, Y.; Wang, W.; Zheng, Y.; You, J.; Huang, S.; Wu, K.; Kong, D.; Luo, Z.; Chen, H.; Li, G. Defect Effect on the Performance of Nonpolar GaN-Based Ultraviolet Photodetectors. *Appl. Phys. Lett.* **2021**, *118* (5), 053501. https://doi.org/10.1063/5.0040110.
(165) Chatterjee, A.; Khamari, S. K.; Kumar, R.; Porwal, S.; Bose, A.; Sharma, T. Role of Threading Dislocations and Point Defects in the Performance of GaN-Based Metal-Semiconductor-Metal Ultraviolet Photodetectors. *Superlattices Microstruct.* **2020**, *148*, 106733. https://doi.org/10.1016/j.spmi.2020.106733.
(166) Cerezo, J. Class D Audio Amplifier Performance Relationship to MOSFET Parameters. *Int. Rectifier Appl. Note -1070 Httpwww Irf Comtechnical-Infoappnotesan-1070 Pdf* **2005**. https://www.infineon.com/dgdl/an-1070.pdf?fileId=5546d462533600a40153559530600fe5.
(167) Corporation E. P. C. Gallium Nitride Brings Sound Quality and Efficiency to Class-D Audio https://epc-co.com/epc/cn/GaN技术杂谈/Post/13752/Gallium-Nitride-Brings-Sound-Quality-and-Efficiency-to-Class-D-Audio (accessed 2021 -11 -02).
(168) Graham, R.; Yu, D. Scanning Photocurrent Microscopy in Semiconductor Nanostructures. *Mod. Phys. Lett. B* **2013**, *27* (25), 1330018. https://doi.org/10.1142/S0217984913300184.
(169) Nanayakkara, S. U.; Cohen, G.; Jiang, C.-S.; Romero, M. J.; Maturova, K.; Al-Jassim, M.; van de lagemaatt, J.; Rosenwaks, Y.; Luther, J. M. Built-in Potential and Charge Distribution within Single Heterostructured Nanorods Measured by Scanning Kelvin Probe Microscopy. *Nano Lett.* **2013**, *13* (3), 1278–1284. https://doi.org/10.1021/nl4000147.

(170) Barker, Jr., B. G.; Chava, V. S. N.; Daniels, K. M.; Chandrashekhar, M. V. S.; Greytak, A. B. Sub-Bandgap Response of Graphene/SiC Schottky Emitter Bipolar Phototransistor Examined by Scanning Photocurrent Microscopy. *2D Mater.* **2018**, *5* (1), 011003. https://doi.org/10.1088/2053-1583/aa90b1.

(171) Chava, V. S. N.; Barker, B. G.; Balachandran, A.; Khan, A.; Simin, G.; Greytak, A. B.; Chandrashekhar, M. V. S. High Detectivity Visible-Blind SiF4 Grown Epitaxial Graphene/SiC Schottky Contact Bipolar Phototransistor. *Appl. Phys. Lett.* **2017**, *111* (24), 243504. https://doi.org/10.1063/1.5009003.

(172) Lyu, Q.; Jiang, H.; Lau, K. M. High Gain and High Ultraviolet/Visible Rejection Ratio Photodetectors Using p-GaN/AlGaN/GaN Heterostructures Grown on Si. *Appl. Phys. Lett.* **2020**, *117* (7), 071101. https://doi.org/10.1063/5.0011685.

(173) Satterthwaite, P. F.; Yalamarthy, A. S.; Scandrette, N. A.; Newaz, A.; Senesky, D. G. High Responsivity, Low Dark Current Ultraviolet Photodetectors Based on Two-Dimensional Electron Gas Interdigitated Transducers. *ACS Photonics* **2018**, *5* (11), 4277–4282. https://doi.org/10.1021/acsphotonics.8b01169.

(174) Kim, Y.; Son, B.; Jeong, H.; Park, K.; Ahn, Y. Electronic Band Alignment in AlGaN/GaN High Electron-Mobility Transistors Investigated Using Scanning Photocurrent Microscopy. *Curr. Appl. Phys.* **2019**, *19* (4), 406–410. https://doi.org/10.1016/j.cap.2019.01.008.

APPENDIX A:

A.1 COPYRIGHT PERMISSION